UNIVERSITÁ DEGLI STUDI DI CATANIA

Dottorato di Ricerca in Fisica - XXIII ciclo

LAURA GRASSI

Nuclear reactions induced by light exotic nuclei produced at INFN-LNS and studied by CHIMERA multidetector

PHD THESIS

Tutors:
Prof. F. Rizzo
Dr. S. Pirrone

PhD coordinator:
Prof. F. Riggi

CONTENTS

INTRODUCTION

Progress in nuclear science is often driven by new accelerator and other advanced facilities, which allow probing ever more deeply into the structure of the nucleus, or even to discover new states of the nuclear matter.

It is well known that the atomic number Z determines the number of electrons of the neutral atom and, consequently, its chemical properties. When displayed on a graph of neutron number N versus Z, the stable isotopes lie along a slightly curved line, called the line of stability (or β-valley of stability), all unstable isotopes decay until the line of stability is reached. The isotope lifetime can range from less than 10^{-3} second to billions of years. Short-lived isotopes cannot be found naturally on earth, even if they are continually created in stars. So they play an important role in the creation of the elements, and in the understanding of the universe origin.

Physics researchers think that most of the elements in the cosmos are formed in stellar environments via reactions that involve many rare isotopes, which are short-lived nuclei (called exotic nuclei) very far from the line of stability. The properties of most of these isotopes are unknown and they can be studied thank to the new facilities in the world and to the theoretical models calculation. In this scenario, nowadays different facilities are running to produce exotic beams and new projects and techniques are going to reach new exotic beams with high energy and intensity.

At Laboratori Nazionali del Sud of the Istituto Nazionale di Fisica Nucleare (LNS-INFN) in Catania (Italy), exotic beams are produced since many years. In particular, the subject of this thesis deals with the opportunity to study direct reactions, using CHIMERA multidetector and beams produced by In-Flight Fragmentation technique. CHIMERA (Charge Heavy Ion Mass and Energy Resolving Array) device is a 4π multidetector made of 1192 telescopes. It has been

build at LNS-INFN to study heavy-ion collisions in the intermediate energy range (20-200 MeV/u). During the last year, thank to the availability of light exotic beams in the ^{11}Be isotope region, the first two experiments have been performed to test the detector's capabilities. The elastic scattering angular distribution of ^{16}C+p and ^{16}C+d at 50 MeV/u, ^{10}Be+p at 56 MeV/u and ^{13}B+d at 52 MeV/u are obtained using the kinematical coincidence technique. The results are very encouraging to next studies of transfer reactions and/or others direct reactions. Several upgrading to optimize the beams transmission and increase their intensity are important to improve the measurement results. Some of these are available in the future experiments.

This thesis is divided in five chapters. The chapter 1 shows a panoramic view of the physics understanding and controversy on the today knowledge of the exotic nuclei, with particular attention to the direct reactions. The chapter 2 describes the principle features of the radioactive beam production method, especially the facilities running at LNS-INFN. The chapter 3 shows the main CHIMERA multidetector characteristics, the tagging system upgrading which allows performing experiments with exotic beams produced by the In-Flight Fragmentation method. The chapter 4 describes the procedure to analysis the experimental data, and to extract the elastic scattering angular distributions. Finally the chapter 5 is devoted to illustrate the procedure and model used to perform the fit of the angular distributions.

CHAPTER 1 – Physics case

1.1 Introduction

Nowadays nuclear physics research is principally devoted to investigate nuclei far from stability by means of radioactive beam facilities. Most of the present knowledge of the nuclear structure is based on the properties of nuclei close to the line of β-stability, where the proton to neutron ratio is almost the same for the stable nuclei. Far from the stability region the nuclear physics models have to be revisited. Different observables disagree the expected dependence, for instance the nuclear radius dependence as $A^{1/3}$, the magic numbers for Z and N seem to be dependent on N and Z, respectively. Besides nucleon correlations and clustering seem to play a much more important role than the binding energy of stable nuclei. The study of nuclei under extreme conditions of isospin (connected to the difference between the proton and neutron numbers) leads to the discovery of new phenomena like nuclei halos, neutron skins and maybe even more exotic structures. Consequently new modes of collective motion are expected in connection with these phenomena, namely oscillations of the neutron skin against the core, similar to the soft dipole mode already identified in the case of very light halo nuclei. Today the thickness and the properties of the neutron skin of exotic nuclei are not well known. This understanding will help to describe the compact systems like neutron stars, an object composed mostly of neutrons at nuclear density or greater and properties of both finite and infinite system.

1.2 The nuclear chart and drip lines

The existence of the atomic nucleus is firstly related to the binding energy of the specific system of protons and neutrons. The binding energy BE is defined as the difference in mass energy between a nucleus ${}^{A}_{Z}X_{N}$ and its constituents of Z protons and N neutrons and can be written by using atomic masses (in atomic mass

units) as [HEY04]:

$$BE(^{A}_{Z}X_N) = \left[Z \cdot M_p + N \cdot M_n - M(^{A}_{Z}X_N)\right] c^2 \qquad 1.1$$

with M_p, M_n denote the proton and neutron mass respectively, $M(^{A}_{Z}X_N)$ is the actual nuclear mass and c^2 having the value of 931.50 MeV/u. Information on atomic masses (experimental or calculated ones) can e.g. be found tabulated on the website of the Atomic Mass Data Center website [ATMCE]. The binding energy is a measure of how much energy has been gained through the strong force by forming the nucleus. On the other hand particle and cluster binding energies give important information about the limits of nuclear existence. Then the neutron (proton) binding energy B_n (B_p) (sometimes called separation energy) is the amount of energy needed to remove the last neutron (proton) from the specific nucleus and gives information on the single state of the nuclear structure. Negative binding energy means that the particle is energetically not bound anymore by the nucleus.

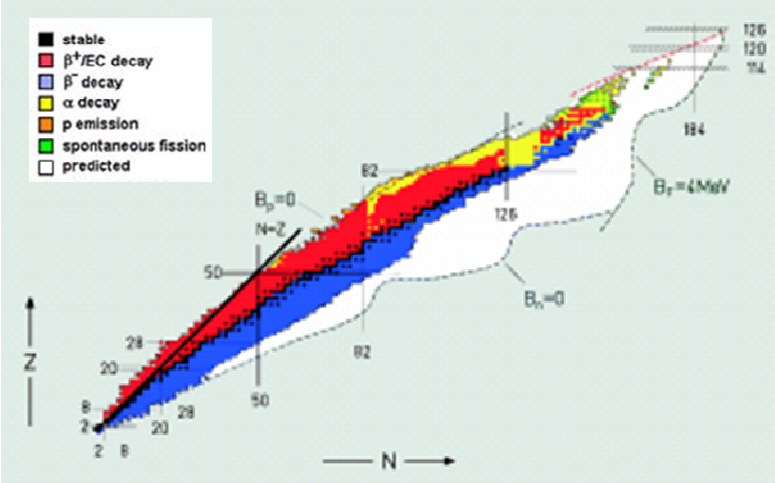

Figure 1.1 The chart of the nuclides showing the neutron and proton drip lines which are defined by demanding that the respective binding energies, B_n and B_p, be zero. The neutron and proton numbers for the closed shells are indicated by the horizontal and vertical lines. The figure also shows the line where the fission barrier B_f goes below 4 MeV and a prediction of the possible shell structure for the super–heavy elements [HUY04].

The chart of the nuclides (see Figure 1.1), also called the Segrè plot, shows the nuclear species as a function of the proton number (Z) and neutron number (N). The black squares correspond to the stable nuclei; this area is called "stability" or "β-stability". There are about 283 nuclear species stable or sufficiently long lived to be found on Earth. We see them initially along the $N = Z$

line, but then moving steadily to the neutron rich side of the chart, because they opposite to the Coulomb force. The chart also indicates how many protons (neutrons) the nuclear ground-state can hold and still be bound. Our present knowledge of atomic nuclei suggests that some 6000–7000 distinct nuclear species live long enough to be created and studied. Since the birth of nuclear physics, many short-living radioactive isotopes have been the subjects of extensive studies,

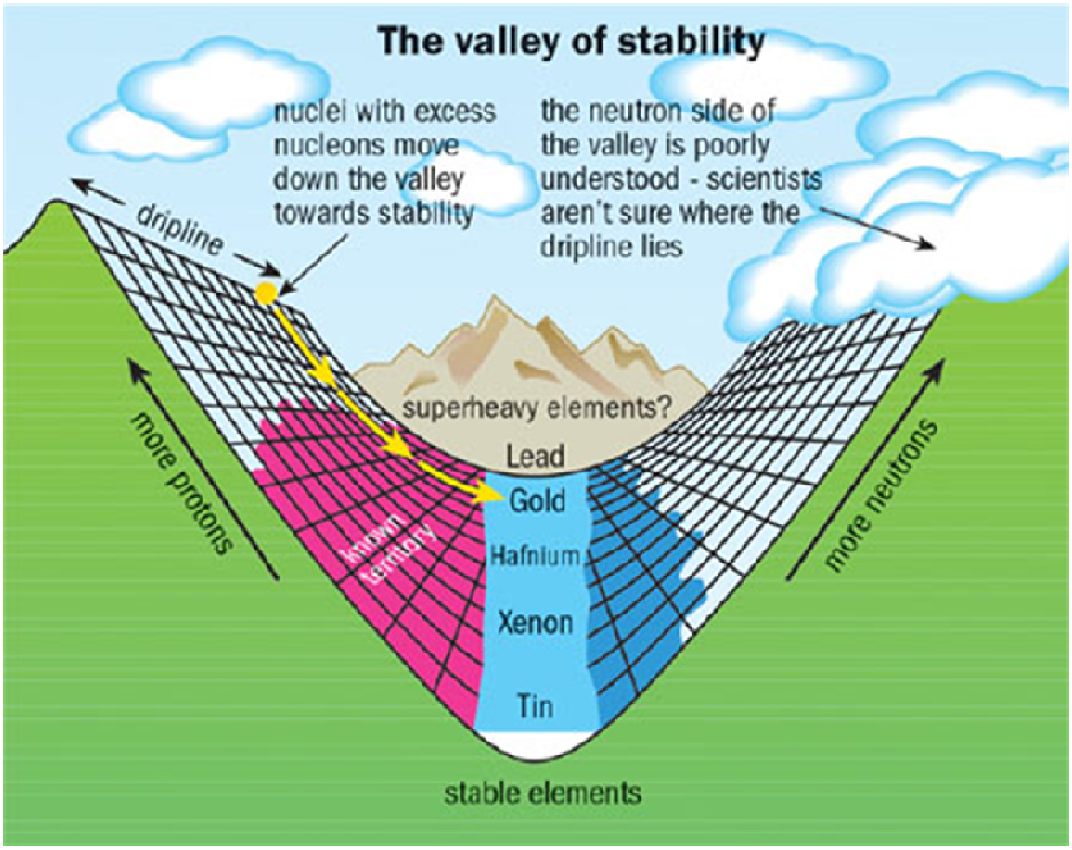

Figure 1.2 An artistic picture of the valley of stability. The valleys walls area symmetric: as one adds neutrons the valley's wall rises less quickly than by adding protons. This is due to the repulsive Coulomb interaction between protons which grows as the square of the number of protons [BOU02].

first as products in natural radioactive chains or through production in cosmic radiation, and later as artificially created in reactors and accelerators. When adding, as a third dimension, the nuclear mass excess (the difference between the nuclear mass and atomic mass number A) a landscape becomes visible: the valley of β-stability (see Figure 1.2). The stable nuclei form the bottom of the valley and can be found by differentiating the Bethe-Weizsäcker semi-empirical mass

formula. The cliffs of the valley rise parabolically for a given mass number. The weak interaction brings the unstable nuclei, through β-decay within isobaric chains, back to the bottom of the valley. The time scale of the β-decay ranges from milliseconds to years and strongly depends on the available decay energy: going further away from stability the decay is faster. Near the drip lines in the Segrè plot, the binding energy (B_p or B_n) of the last nucleon (proton or neutron) becomes zero and the strong interaction takes over the weak one. These lines are accepted as the borderlines of nuclear existence, although for particular cases barriers can slow down the particle emission and lead to the observation and study of nuclei beyond the drip lines, so the exact location of them is, for certain isotopes, not well known. For a given isotope, differences up to 16 mass units in the predicted drip lines using different mass models can be the result.

Other decay modes based on cluster emission, such as α decay and fission, will become faster than β decay and will take over. The half life for α decay depends mainly on the available decay energy (Q_α-value, see [ATMC]) compared to the height of the Coulomb barrier, although local nuclear structure effects can alter the half life by one to two orders of magnitude. Different regions, where α decay is or will be the main decay mode, can be localized on the chart of nuclei (see Figure 1.1). The half life values of the spontaneous fission process are much more difficult to obtain due to the extreme sensitivity to the fission barrier shapes. Furthermore, shell effects can stabilize the so-called “superheavy elements” towards the spontaneous fission process and therefore the question of where nuclear existence ends in the superheavy corner is still open. In Figure 1.1 a borderline is drawn where the fission barrier lays around 4 MeV. Taking the different borderlines into account, more than 6000 nuclides are believed to exist of which 3600 have been observed even if not all of them have been studied in full detail. Within this high number, important information on the forces interacting in the nuclear medium is present and the most exotic nuclei is believed to give a deep

understanding of the nucleus and its structure [HUY06].

1.3 Physics interests in Radioactive Ion Beams (RIBs)

As it was discussed in previous section, various extrapolations using mass formulae and fits to the known nuclei in the region of stability diverge rather wildly when approaching the drip-line region. So, it is clear that main interest is found in studying new ways in which protons and neutrons are organized in forming nuclei, which are either very neutron or proton rich.

In order to reach those regions, new production and separation techniques are under development, leading to intense and energetic radioactive ion beams of short-lived nuclei. Eventually, these beams can be used to go even further out of stability. A very important driving idea in the production of these radioactive beams is the accessibility to the nuclear reactions that play a role in the element formation inside stars. The domain at the borderline between nuclear physics and astrophysics, called 'nuclear astrophysics', can thus be studied and will help to find the key reactions that have led to the formation of the lightest elements first: light-element synthesis, understanding the CNO catalytic cycle, etc. Indeed radioactive beam experiments are important for the measurement of reactions and decay processes of radioactive nuclei which can take place at the high temperatures, typical in explosive stellar events. Reaction measurements with radioactive beams have been successfully performed, simulating nuclear processes in the Big Bang and for explosive hydrogen and helium burning conditions. Besides in the domain of nuclear astrophysics, the exploration of the neutron-rich side is essential: in this region, in fact the formation of the heavier elements occurres during the r-process (the rapid capture of a number of neutrons in reactions (n, γ)), before β-decay back to the stable region could proceed [HEY04].

1.4 Nuclear structure far from stability

The shell model is related to the description of nuclear excitation modes and the properties in the ground-state. So one of the main questions is to find the way to extrapolate the nuclear mean field approach in region far from the β-stability. Indeed nuclei with high isospin have properties as spin, parity, and electromagnetic moments, different from the ones foreseen by the shell-model. Many phenomena may affect the shell structure, such as the isospin dependence of the effective interaction and in particular the spin-orbit term.

While shells and magic numbers are important to determine the properties of the nucleus, polarization effects can also play a relevant role. More specifically, there are collective effects involving from several to all nucleons leading to a variety of phenomena such as vibrations, rotations and giant resonances. They are driven by correlations among nucleons. Collectivity leads to deformation and weakening of the spherical shell structure. Much of the richness of nuclear structure derives from the interplay between these competing tendencies, namely the interweaving of single-particle and collective motion and their subtle dependence on nucleon number.

1.4.1. Shell structure

The shell model is the basic framework for nuclear structure calculations in terms of nucleons. It is based on the assumption that, as a first approximation, each nucleon inside the nucleus moves independently in a spherically symmetric potential, generated by the other nuclei and including a strong spin-orbit term. The nucleons are arranged in shells, each one able to contain up to a certain number of nucleons determined by the Pauli principle. The so called “magic numbers” correspond to fully occupied shells. An energy gap appears between the last completely occupied and first unoccupied shell, this provides extra stability to this particular combination of nucleons. Magic numbers are well established for nuclei

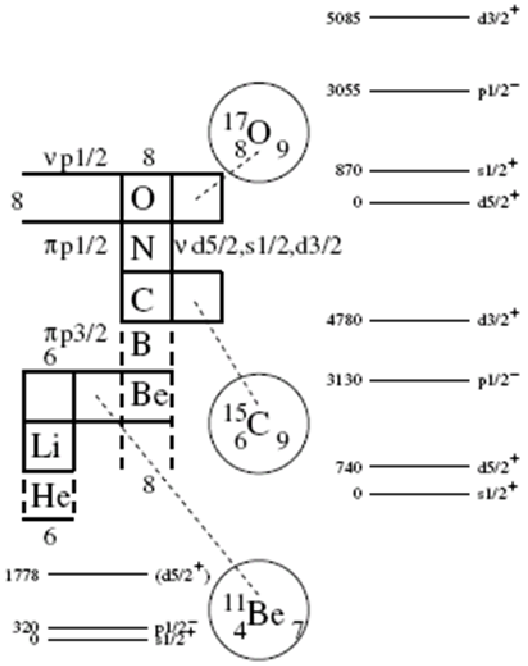

Figure 1.3 Examples of shell inversion [GRA04].

along the stability line and for most of the known unstable nuclei.

For nuclei far from stability vanishing of the traditional shell gaps and appearance of new magic numbers might however occur. One important aspect, which is currently the subject of much discussion, is the so-called “shell quenching”, which is related to the modification of the average field experienced by a single nucleon as a consequence of changes in size and diffuseness for nuclei with large isospins. For these nuclei far from stability, the softening of the Woods-Saxon shape of the neutron potential is expected to cause a reduction of the spin-orbit interaction and therefore a migration of the high-l orbitals with a substantial modification of the shell structure [DOB94, HEY04].

In this scenario single particle states, two nucleon separation energies S_{2n} and S_{2p} and their differences δ_{2n} and δ_{2p} respectively, excitation energies are used as signatures for shell structure. It can consider some examples of the experimental discoveries of the level inversion. The Figure 1.3 illustrates the evolution of the N=8 shell gap. ^{17}O has 8 protons (magic) and 9 neutrons. Removal of the two $p_{1/2}$ protons from the ^{17}O to ^{15}C causes the $5/2^+$ and $1/2^+$ levels swap excite states. The removal of the first pair protons in $p_{3/2}$ in ^{12}Be causes an upward shift of the $p_{1/2}$ of the neutrons partners, closing the N=8 gap neutron and opening the N=6 gap. This behaviour is strongly evident in ^{11}Be level scheme with the inversion of the $s_{1/2+}$ and $p_{1/2-}$ levels (shown in Figure 1.3).

The status of the nuclear shell model is determined by the capabilities to

take care of a continuous set of adjustments, in order to handle many major shells at the same time, by the availability of realistic two-body effects accounting the three body effects and the comparison with experimental data in exotic region [GRA04].

1.4.2. Nuclear moments and nuclear masses far from stability

The ground-state properties of an exotic nucleus such as half life, decay mode, decay energy and subsequently the mass are often the first experimental information obtained. The ground-state mass is of particular importance as all interactions and correlations contribute to it. By experimentally mapping the mass surface and improving the theoretical mass formulae, it becomes clear that clustering and nucleon correlations create more binding and therefore more exotic nuclei are expected to be bound. While in the past most of the masses of radioactive nuclei were deduced from their decay characteristics (such as α- and β-decay energies) and in the region of the stability from reaction work (such as energy thresholds for transfer reactions), the manipulation of radioactive beams has advanced so much that superior mass measurements are now possible in traps, accelerators, dedicated spectrometers and storage rings.

The density in the atomic nucleus, as well as the diffuseness of the surface, was predicted to be nearly constant and as a consequence the nuclear radius varies with mass number as $R_0A^{1/3}$ with R_0 ranging from 1.2 to 1.25 fm. Furthermore, the protons and neutrons are mixed homogeneously in the nucleus. One can then calculate the change in the mean square radius by adding one neutron to a nucleus, assuming a uniformly charged, spherical liquid drop. Around mass A = 100 this is typically of the order of 0.3 percent, which is small compared to the change in the mean square radius induced by a deformation of the spherical shape: a typical quadrupole deformation, $\beta_2 = 0.3$, causes an increase of $\langle r \rangle^2$ of 3 percent. Such

changes can be deduced accurately by measuring the isotope shift of a spectral line between two isotopes.

The advent of radioactive beams made possible to measure interaction cross sections of radioactive ions, and surprisingly large root mean square radii were observed in the first experiments in Berkeley [TAN85] for ^{6}He and ^{11}Li. The large size of these particular nuclei was explained as due to the halo effect, which arises from the weak binding of the last valence nucleons. The particular situation of nuclear radii in the beginning of the nuclear chart is shown in Figure 1.4.

The ground-state spin and parity, the nuclear electromagnetic moments, the magnetic dipole moment and the electric quadrupole moment, provide crucial information on the nucleus, as on the specific single-particle characteristics of the valence nucleon(s), as well as on the collective properties of the underlying core. The knowledge of spin and parity of a ground-state, often comes from its decay characteristics, provided the structure of the daughter nucleus is well known. But in many cases the selection rules for the specific decay mode(s) only limit the possible spin range and therefore other methods have to be developed to have a unique spin and parity determination. The magnetic dipole moment is directly

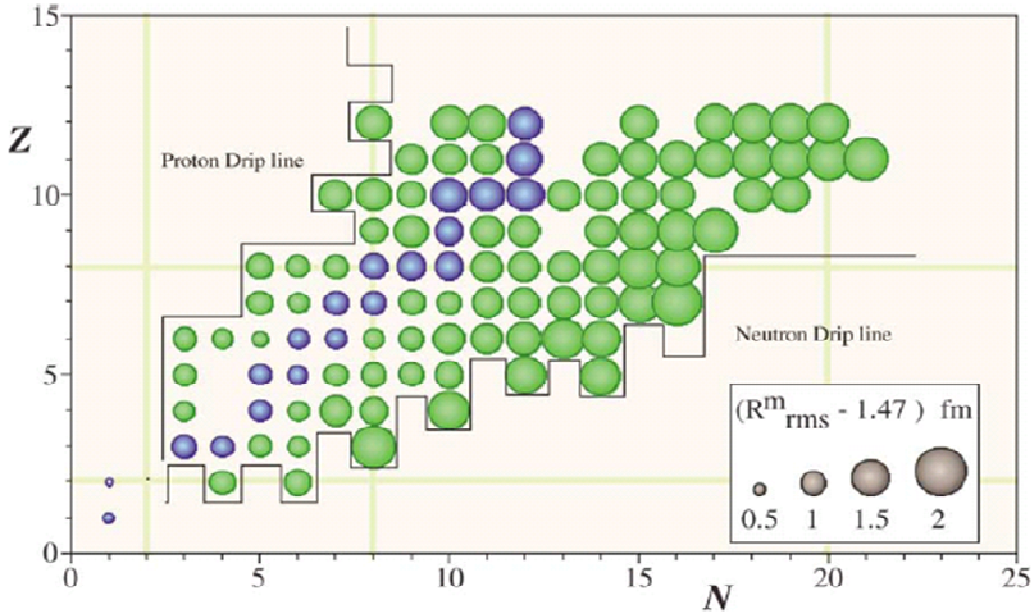

Figure 1.4 Root-mean-square matter radii of light nuclei [TAN03].

related to the nuclear spin through the gyromagnetic ratio [HUY06].

Several ingenious techniques have been developed to measure nuclear electromagnetic moments and they have recently been reviewed by G. Neyens [NEY03]. The magnetic dipole and electric quadrupole moments of ^{11}Li and ^{9}Li, and thus the proton distributions, are very similar which, in turn proves that the extended radius in ^{11}Li is due to the extra neutron pair [ARN92].

With the advent of energetic radioactive ion beams, a number of reactions can also be used to obtain information on the spin and the parity of the ground-state of the projectile and of the populated states. An interesting spin-off of the optical techniques that have been developed to measure electromagnetic moments is the laser ion source. Laser light can be used to ionize efficiently and selectively the radioactive isotopes of a specific element produced in nuclear reactions. The influence of the nuclear properties on the atomic optical transitions through the hyperfine interaction can be probed with the resonant laser ionization technique by scanning over the laser frequency [HUY06].

1.4.3. Halo Nuclei

The halo is a threshold effect arising from the very weak binding of the last one or two valence nucleons (usually neutrons) with a well-defined inert ‘core’ containing all the other nucleons. In halo nuclei, the potential well corresponds to the mean field potential of the core of the nucleus. The valence nucleon (the discussion will be restricted to one halo nucleon principally) has a good chance of finding itself outside the core. The uncertainty principle ensures that such bound states have a relatively short lifetime, of the order of a few milliseconds to a few seconds. This is quite long enough for such nuclei to be formed and used in nuclear reactions in order to study their unusual features.

The accepted definition of a halo nucleus (typically in its ground-state) is therefore that the halo neutron is required to have more than 50% of its probability

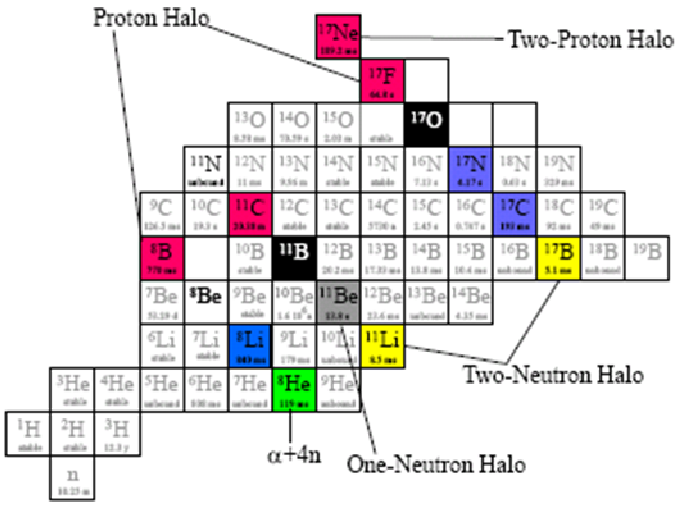

Figure 1.5 Many new phenomena occur for dripline nuclei. Some of them are illustrated here for the A=8, 11 and 17 isobars. The A=8 isobar consists of nuclides, which are all radioactive. The astrophysical interesting nucleus ^{8}B is a one-proton halo nucleus while ^{8}He may best be described as an alpha core surrounded by four neutrons. For A=11 the neutron dripline is reached for ^{11}Li ($T_{1/2}$=8.3 ms), which is a two-neutron halo nucleus, while ^{11}Be is a one-neutron halo with an intruder s-state in its ground-state. The level order of the ground-state and the first two excited states in ^{11}Be is identical to that of its unbound mirror nucleus ^{11}N. The A = 17 isobar is limited by the two-neutron and two-proton halo nuclei ^{17}B and ^{17}Ne, respectively, and the beta-decay of the latter feeds an excited proton-halo state in ^{17}F at 495 keV [JON04].

density outside the range of the core potential. In such open structure, it is not surprising that shell model and mean field approaches to describe such systems break down, and few-body (cluster) models of core plus valence particles can account for the most general properties of these nuclei, such as their large size and breakup cross sections. In addition to the decoupling of core and valence particles and their small separation energy, the other important criterion for a halo is that the valence particle must be in a low relative orbit angular momentum state, preferable a s-wave, relative to the core, since higher l-values give rise to a confining centrifugal barrier. The confining Coulomb barrier is the reason why proton halos are not so spatially extended as neutron halos.

The three most studied halo nuclei are ^{6}He, ^{11}Li and ^{11}Be. However others exotic halo systems will be confirmed, such as ^{14}Be, ^{14}B, ^{15}C and ^{19}C. The above examples are close to the neutron dripline at the limits of particle stability. Other candidates, awaiting proper theoretical study and experimental confirmation include ^{15}B, ^{17}B and ^{19}B, along with ^{16}C, ^{22}C and ^{23}O. Proton halo nuclei examples include ^{8}B, ^{13}N, ^{17}Ne and the first excited state of ^{17}F.

Another special feature is that most halos tend to be manifest in the ground-states of the nuclei of interest. Indeed, most of the known halo nuclei tend to have only one bound state; any excitation of such a weakly bound system tends to be into the continuum, with the notable exception of ^{11}Be which has two bound states.

It is possible to distinguish single halo, two neutron halo and neutron skin (see Figure 1.5). Two-neutron halo nuclei, such as ^{6}He and ^{11}Li have the remarkable property that none of their two-body subsystems are bound. Thus, ^{6}He can be modelled as a bound three-body α+n+n system despite there being no bound states of α+n (^{5}He) or n+n (the dineutron). Such nuclei have been called 'Borromean' [ZHU93] and their wavefunctions require rather special asymptotic features to account for this behaviour [KHA04]. There are different model to describe their nuclear structure. In general, single halo can be studied using a simple two-body (cluster) model, core + valence neutron, bound by a short range potential. Indeed one of the criteria for a halo state to exist is if the total probability for the neutrons to be found outside the range of the potential is greater than the corresponding probability within the potential. Two neutron halo model considers the motion of the two neutrons around the nucleus core and can be described through Hartree-Fock techniques. A number of studies are currently developing fully microscopic (ab-initio) structure models. They start from a realistic NN interaction and can also include 3-body forces. Another promising approach is the Coupled Cluster Method [DEA03]. This has been used widely in a number of other fields, such as chemistry, atomic and condensed matter physics, and it has only recently been applied seriously to nuclear structure.

1.5 Nuclear Reactions induced by RIBs

The continuous improvement in the intensities and optical qualities of secondary radioactive beams leads to systematic studies of nuclear reactions, essential to the development of modern nuclear physics. In particular direct reactions that selectively excite a minimal number of nucleonic degrees of freedom are particularly relevant. So mechanisms such as Coulomb excitation, more recently elastic and inelastic scattering, transfer and knock-out reactions are rapidly becoming standard tools for the investigation of the structure of nuclei far from stability.

At energies larger than 500 MeV/u it is generally accepted that the Glauber approximation [GLA59] can be used to infer charge and matter distributions from proton elastic scattering data, if the cluster structure of the nuclei is properly considered [KHA96, KHA01].

At lower beam energies, inelastic scattering can be used to measure the resonance structure of nuclei and the nature of low-lying excitations. Inelastic excitations can provide additional information, complementary to Coulomb excitation studies, since the nuclear interaction that leads inelastic excitation is function of protons and neutrons numbers, while Coulomb excitation depends only on the interaction of protons [IWA00a, IWA00b].

Transfer reactions can be used to accurately determine atomic masses, excited state energies, level spins and parities, and spectroscopic factors. It has also been established that nuclear deformations have clear signatures that can be inferred from transfer reaction angular distributions [WER94, BER83]. The use of angular distributions inverse kinematics could even be extended to electron-nucleus scattering by the use of a colliding electron exotic nucleus storage ring. This would allow an accurate determination of charge distributions in nuclei [CAS00].

The following subjects concerning the elastic scattering, transfer and

breakup reactions are strictly connected with the investigation of this thesis.

1.5.1. Elastic Scattering

The elastic scattering is a well known reaction process and it has been an important source of information on nuclear properties. This information can be obtained primarily through studies of the potential of interaction ("optical potential") that is found to reproduce measurements of the elastic scattering cross sections. In distorted waves Born approximation (DWBA) the distorted wavefunctions for the incoming and outgoing particles are generated using optical potential. It describes elastic scattering and effect of the non-elastic channels is taken into account through the imaginary part of the optical potential. If, however, one or more inelastic channels are strongly coupled to the elastic channel it is not sufficiently accurate to take them into account through the optical potential, nor it is sufficiently accurate to use DWBA to calculate the scattering into these inelastic channels. This strong coupling situation arises when strongly collective states are excited (coupled-channels (CC) approach) [BRA97].

The phenomenological optical model tries to replace the complex many-body problem of the interaction of two nuclei by the interaction of two structure-less particles through an effective potential. In the description of the elastic scattering, the effect of non-elastic processes such as inelastic scattering and transfer lead to absorption of flux out of the elastic channel, being represented by adding an imaginary term to the potential. While the effective potential is in principle non-local, it is usually replaced by its local equivalent of the general form

$$U(r) = V_C(r) - V(r) - iW(r) \qquad 1.2$$

where V(r) is the real well depth, W(r) is the imaginary part that takes into account the non elastic effect of the interaction. $V_C(r)$ represents the Coulomb potential usually described by:

$$V_C(r) = \begin{cases} \dfrac{Z_a Z_A e^2}{r}, & r \geq R_{ch} \\ \dfrac{Z_a Z_A e^2}{r}\left(3 - \dfrac{r^2}{R_{ch}^2}\right), & r \leq R_{ch} \end{cases} \qquad 1.3$$

where R_{ch} is the sum of the charge radii of the interacting nuclei, Z_a and Z_A are the charge of the two nuclei colliding and r is the relative distance. The calculated elastic scattering is usually insensitive to the choice of R_{ch} for heavy-ion elastic scattering [KEE09].

When studying proton plus nucleus elastic scattering at energies well above the Coulomb barrier, usually it can be neglected specific effects due to couplings to other reaction channels. It is then possible to describe the scattering by phenomenological or microscopic potentials that vary slowly with energy. Microscopic optical model approaches have been used for many years to calculate the nucleon-nucleus and nucleus-nucleus entrance channel, optical potential and transition potentials, for scattering to excited states [ALA04].

A very popular microscopic optical model description for obtaining the real and imaginary parts of the nucleon-nucleus optical potential is the JLM model

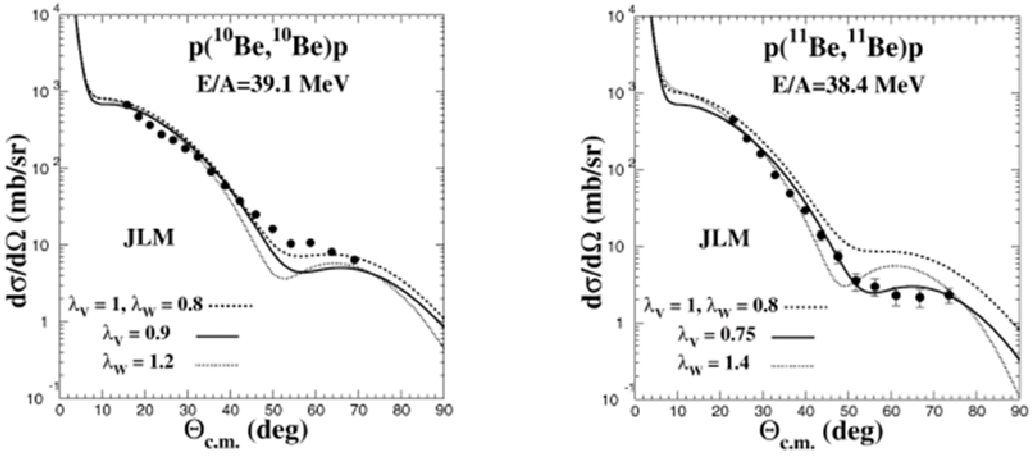

Figure 1.6 On the left side the cross sections for the ^{10}Be + p elastic scattering at 39.1 MeV/u compared to calculations using the JLM potential and the "Sagawa" density. The full circles correspond to the data. The dashed line corresponds to the standard JLM calculation for light nuclei. Full line (dotted line) corresponds to calculations in which the real part (imaginary) was renormalized. The potential is written: $U_{JLM} = \lambda_V V + i\lambda_W W$, with λ_V, λ_W the normalization factors of the real V and imaginary W parts of the potential. On the right side ^{11}Be + p elastic scattering at 38.4MeV/u [LAP08].

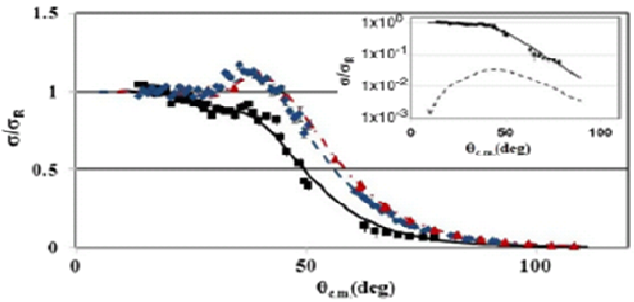

Figure 1.7 Elastic-scattering angular distributions on ^{64}Zn: ^{9}Be (red triangles), ^{10}Be (blue diamonds), and ^{11}Be (black squares). The lines represent the optical model calculations for ^{9}Be (dot-dashed line), ^{10}Be (dashed line), and ^{11}Be (full line). The inset shows the measured angular distribution (symbols) and optical model fit (full line) for the ^{11}Be+^{64}Zn system together with the result of the calculation for the inelastic excitation of (1/2$^-$, Ex= 0.32 MeV, dashed line). The error bars are statistical for $^{10;11}$Be and statistical and systematic for ^{9}Be on ^{64}Zn. In order to reproduce ^{11}Be data, it was used a surface potential to take into account the diffuse halo structure [DIP10].

developed by J.P. Jeukenne, A. Lejeune and C. Mahaux [JEU77]. In this model, ground-state and transition densities are used to deduce, from infinite nuclear matter, optical potential calculations, the elastic scattering and the transition optical potentials of finite nuclei [ALA04]. An example, the Figure 1.6 shows angular distribution of elastic scattering of ^{10,11}Be nuclei and it is compared with the calculations using the optical model and a microscopic approach for the proton–nucleus potential.

In literature it also established that to describe elastic scattering involving weakly bound nuclei at incident energies lower than 150 MeV is necessary take into account the strong couplings to the continuum states[1] of the break-up channels to the elastic channel [SAK87]. The probability to be excited to continuum states is higher, compared to the stable isotopes, and this may induce new features in the interaction potential. The coupling to the other reaction processes may also be stronger. In principle, to calculate the interaction potential for elastic scattering, one should include all possible virtual couplings between the ground and higher excited states. These processes remove flux from the elastic channel [BRA97]. The interaction term arising from couplings to inelastic channels is called the

[1] Continuum states: for a pair of interacting nuclei (a, A), states where either a or A or both are unbound are referred to as continuum states. The continuum, so called, because there are an infinite number of unbound states that blend into a continuous whole containing resonant states of well-defined spin and parity and decay widths as well as the main non-resonant continuum. Couplings to and within the continuum are particularly important for weakly-bound nuclei and can have significant effects on other channels, particularly the elastic scattering [KEE09].

dynamical polarization potential (DPP) [BRA97]. This term is complex, non-local and energy-dependent, it includes the coupling to excited states and to continuum states or to other reaction processes, like transfer reactions or break-up.

Another new approach describes the elastic scattering with halo nuclei through optical model adding a part related to the surface potential. A systematic work on elastic scattering around Coulomb barrier with halo nuclei [DIP10] gives very interesting information about the surface properties, such as size of nuclei and surface diffuseness (see Figure 1.7).

1.5.2. Transfer Reactions

Distorted wave theories applied to transfer (knock-out, stripping, etc.), assume two-body descriptions of both the entrance and exit channels. The comparison with experimental data allows to obtain different information; in facts measurements of the energy spectra give locations about the states of the residual nucleus and values for the separation energies of the transferred particles. Whereas measurements of the angular distribution give information about the transferred angular momentum (from the shape of the distribution) and about the strengths of the transitions (from the magnitude).

The workhorses of this effort were the (*d*, *p*) stripping and (*p*, *d*) pickup reactions, but many other reactions were used, including two-particle transfers.

For reactions with radioactive beams, one must work in inverse kinematics, since the nucleus of interest is now the projectile and not the target. Very few transfer reaction studies involving radioactive beams have been carried out so far. This is mainly due to the low cross section, of the order of 1 mb/sr.

Interest in the halo nucleus ^{11}Be has prompted work on the p(^{11}Be,^{10}Be)d reaction at 35 MeV/nucleon [WIN01]. As previously mentioned, the nucleus ^{11}Be is particular interesting for several reasons. The ground-state spin parity is $1/2^+$ in contradiction to the simple shell model and spherical Hartree–Fock prediction of

$1/2^-$. This "parity inversion" is correctly predicted by, for example, psd-shell calculations of [BRO96]. The simplest configuration consists of a $2s_{1/2}$ valence neutron coupled to a ^{10}Be core, that is $\alpha\left|{}^{10}Be\left(0^+\right)\otimes 2s_{1/2}\right\rangle$. In case of core excitation (2^+ excited state at 3.368 MeV for ^{10}Be), there is another component with a valence neutron in the $1d_{5/2}$ sub-shell, that is $\beta\left|{}^{10}Be\left(2^+\right)\otimes 1d_{5/2}\right\rangle$. If one expresses the wave function of the $1/2^+$ ^{11}Be ground-state as the sum of the single-particle and core excited components

$$^{11}Be_{gs}=\alpha\left|{}^{10}Be\left(0^+\right)\otimes 2s_{1/2}\right\rangle+\beta\left|{}^{10}Be\left(2^+\right)\otimes 1d_{5/2}\right\rangle \qquad 1.4$$

The spectroscopic factors for transfer to the ground and first excited state of ^{10}Be should be directly related to α^2 and β^2 assuming negligible population of the 2s1d orbitals by ^{10}Be core neutrons. Then the study of the neutron transfer ^{11}Be(p,d)^{10}Be provides information on the overlap between the ground-state in ^{11}Be and the 0^+_{gs} and 2^+_1 states in ^{10}Be, as well as on the ratio of the two components β/α [WIN01] (see Figure 1.8).

An experimental observable, to probe the strength of pairing correlations, is the probability of reactions in which a pair of neutrons is transferred between projectile and target. Again the reaction, typically (t,p) or (p,t), would be performed in inverse kinematics. The difference in the asymptotic behaviour of single-particle density and pair density in a weakly bound system can be measured by comparing the energy dependence of one-particle and pair-transfer cross sections. The question of the evolution of the pairing effects as function of isospin and nuclear density has often been discussed. In general, it is predicted that the pairing gap increases with neutron excess. This effect is related to the density dependence of the pairing interaction and the lower density associated with skins and haloes. The increase of the pairing correlation should be reflected in larger probabilities in two-neutron transfer reactions, which are the direct measurement of the pair field.

1.5.3. Break-up reactions

In the previous sections, it has been described that transfer reaction is an important tool for the study of the single-particle characteristics. However, transfer reactions experiments, in the case of an exotic partner of the reaction, are often difficult to perform due to low cross sections. Beside most importantly the theoretical analyses require very precise knowledge of the nucleus-nucleus elastic scattering optical potentials, which in turn can contain the effects of break-up [TYM99, BON02]. Then the study of break-up reactions represents an important complementary approach.

The breakup reaction on a light target is characterized by an unusually narrow momentum distribution of a "core" fragment and an enhanced reaction cross section, reflecting the extended neutron halo structure. Indeed, the halo structure was first discover for ^{11}Li by observing the enhanced interaction cross section for this nucleus [TAN85] and the narrow momentum distribution of ^{9}Li, following the breakup of ^{11}Li on a carbon target [KOB88, ORR92].

In case of one neutron halo, the simplest measurement is the single-neutron removal cross section, in which only the core is observed in the final state,

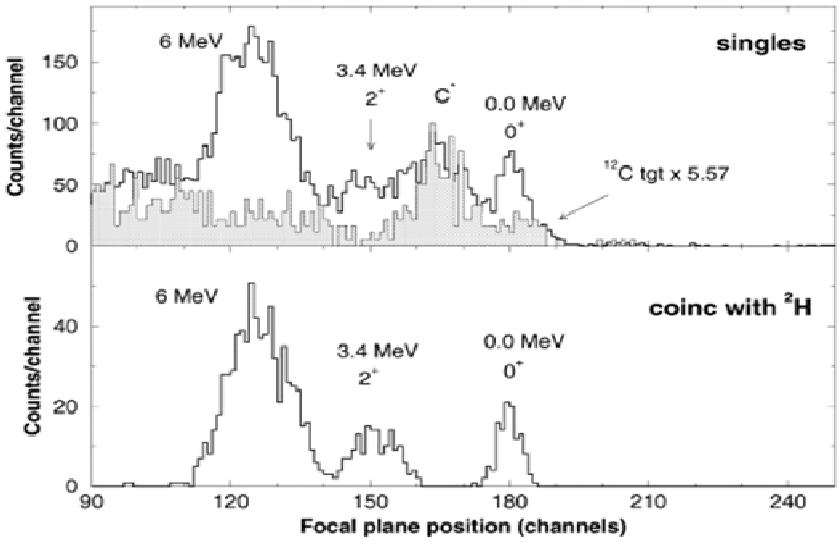

Figure 1.8 ^{11}Be at 35.3 MeV/u on CH^2 target with SPEG and CHARISSA array. Upper panel ^{10}Be focal plane spectra in singles; lower panel: in coincidence with deuterons in the CHARISSA array. The spectra are for ^{10}Be laboratory angles from 0.4° to 1.2° [WIN01].

as in the transfer reaction. If the interaction responsible for the neutron removal is the neutron-target nuclear potential [BON98], the core cross section in coincidence with the neutron is called diffractive (or elastic) breakup cross section.

In the case of heavy targets, the coincident cross section contains also the contribution from Coulomb breakup due to the core-target Coulomb potential which acts as an effective force on the neutron [BON03]. So in general, in all theoretical models the dynamics is controlled by the three potentials describing nucleon-core, nucleon-target, and core-target interactions.

In some works it has been established that the halo breakup is responsible for a damping in the elastic angular distribution, in the range of 5°–20° [KHA04, BON02]. Besides charge exchange reactions, which produce radioactive nuclei in the final state, have also been studied. The effect of the halo breakup is very dramatic in this case, reducing the absolute cross sections by about 50% [CAP01].

In general the theoretical methods used to describe the above mentioned reactions, require at some stage of the calculation the knowledge of the nucleus–nucleus optical potential. The problem of the determination of the optical potential for a halo projectile has already been studied by many authors and a summary can be found in [PAC00]. For example one method is to start from a phenomenologically determined core–target potential and then the effect of the breakup of the halo neutron is added. This process leads to adding a surface part to the core–target potential [BON02]. This new surface peaked optical potential has been seen to have a quite long range which should reflect the properties of the long tail of the halo neutron wave function. Such kinds of potentials are often called, as previously said, DPP.

Another approach to the calculation of the imaginary part of the optical potential due to breakup is based on a semiclassical method described by Broglia and Winter in [BRO81a,BRO81b]. This is also used by Brink and collaborators [BON85,STA85] to calculate the surface optical potential due to transfer and in the

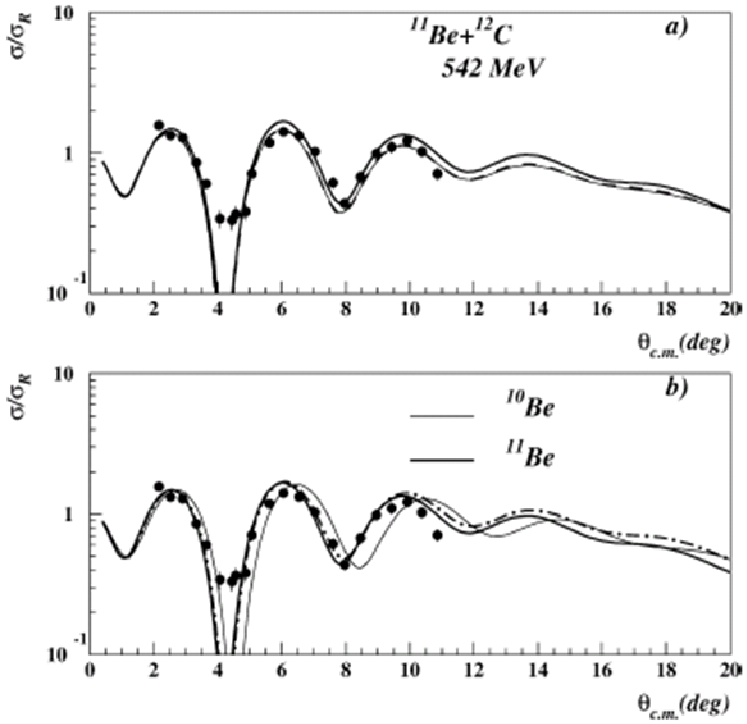

Figure 1.9 (a) Elastic scattering angular distribution for the reaction ^{11}Be + ^{12}C. Solid line is with a bare volume imaginary potential. Dashed line is obtained adding the imaginary surface potential. Dotted line includes also the real part of the surface potential. (b) Solid line is obtained with the same bare potential as in (a), the dotted line is obtained by decreasing both the real and imaginary potential radii as explained in the text, while the dot-dashed line is obtained decreasing only the imaginary potential radius [BON02].

Bonaccorso and Brink model for transfer to the continuum reactions [BON88, BON91a, BON91b, BON92, BON98]. The idea is that the breakup is a reaction following the same dynamics as transfer but leading manly to continuum final states for incident energies per nucleon higher than the average nucleon binding energy.

Since the optical potential has one of its most interesting applications in the calculation of elastic scattering angular distributions, Figure 1.9 shows an example for the reaction ^{11}Be + ^{12}C at 49.3 MeV/u. The optical model parameters for the volume parts of the bare potential are taken from Ref. [KHA97] (solid line). The dashed line is obtained instead including the surface imaginary potential calculated according to the method proposed in the work [BON02]. The theoretical

calculations reproduce the behaviour of the experimental data especially at angles larger than 5° where the effect of breakup is to suppress scattering [BON02]. The angular distribution shows the usual Fraunhofer oscillations at small angles, followed by an almost exponential decrease of the cross section due to far side dominance.

CHAPTER 2 – Production of radioactive beams

2.1 Introduction

The exploration of nuclear matter under extreme conditions is one of the major goals of modern nuclear physics. The opportunities offered by exotic ion beam for research in the areas of nuclear structure and mechanism and nuclear astrophysics are exciting, and worldwide activity in the construction of radioactive beam facilities bears witness to the strong scientific interest in the physics, that can be probed with such beams. Moving away from the valley of stability, the production of the so called “exotic nuclei”, however, is compared with difficulties because of the extremely low production cross section and very short half lives of the nuclei of interest. Nowadays there are two complementary ways to make good quality beams of exotic nuclei: the Isotope Separation On Line and the In Flight Fragmentation methods (see Figure 2.1):

The Isotope Separation On Line method (ISOL): radioactive species are produced in a target and thermalized in a catcher consisting of solid, liquid or gas material. The isotopes are subsequently extracted from the catcher material and ionized in an ion source. After extraction from the ion source the species are mass analyzed using magnetic selector and subsequently accelerated to the required energy. Beams produced have good optical quality and variable in energy essentially from rest (meV/u) to intermediate energy (a few 100 MeV/u) [HUY04].

In Flight Fragmentation method (IFF): thin production target is bombarded with an accelerated heavy-ion beam in order to have the reaction products recoiling out of the target. The primary beam fragments into a variety of stable and exotic secondary beams, moving with velocities around the primary

beam. This method uses the reaction kinematics, some combination of magnetic and electrical fields, and atomic processes to identify the nuclei and to separate the isotopes of interest from the primary beam or from other isotopes produced in the reaction. In this way it is applicable to very short-living nuclei (~μs) [DUP06].

Several RIBs (Radioactive Ion Beams) facilities are currently running in the world and new projects have been developed. A new generation of RIBs facilities is planned with FAIR (Germany), SPIRAL2 (France) and FRIB (USA), looking for hybrid combination of the two production methods described above. At the Laboratori Nazionali del Sud of Istituto Nazionale di Fisica Nucleare in

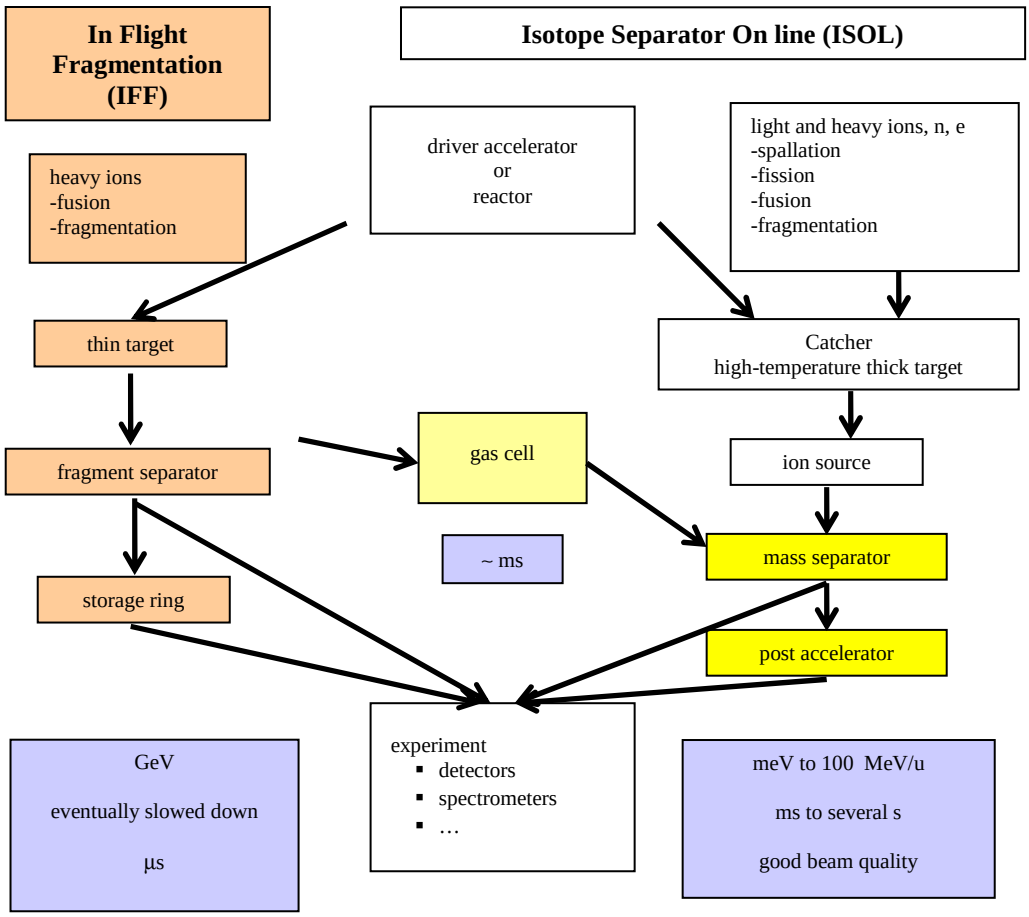

Figure 2.1 A generic description of the IFF and ISOL methods [HUY04].

Catania (Italy), LNS-INFN, exotic beams are produced by IFF beams and by EXCYT facility (ISOL method). Besides, since 2008 it has been started collaboration in the SPES (Selective Production of Exotic Species) project consisting in the design and realization of a new facility based on the ISOL technique for production of radioactive beams of medium mass. This project will be realized at the Laboratori Nazionali in Legnaro of the Istituto Nazionale di Fisica Nucleare (LNL-INFN). It represents an intermediate step towards the EURISOL project [EURW].

2.2 The Isotope Separation On Line method (ISOL)

The different steps of an ISOL system, shown in Figure 2.1, can be considered: production, thermalization, ionization, extraction, mass separation, cooling, charge-state breeding and acceleration and often some of them are embedded in a single unit of the system. The different steps are governed by physical and chemical processes, thus both physical (e.g., production cross-section, decay half-life, ionization potential) and chemical (e.g., molecular formation probability, volatility) properties of the nuclei of interest and of the target material are important.

2.2.1. Reaction mechanisms

The main aim of the target systems is to produce as much isotopes as possible and to get the released in gaseous form, from the target, as fast and as efficient as possible. A wide variety of reactions and beam-target combinations are chosen to produce the radioactive isotopes of interest, looking the predicted cross section of the system and therefore to obtain a high production yield for the exotic nuclei of interest. Usually the processes involved in the exotic beam productions are: light and heavy ion fusion evaporation, direct reactions, fission, spallation and

fragmentation reactions. Different projectiles with a wide energy range are used to induce the nuclear reaction in the target: low energy protons and neutrons of 30 to 100 MeV, high-energy protons of 500 to 1500 MeV, heavy ions of 4 to 100 MeV/u, thermal neutrons and electron beams of 50 MeV.

Beams close to the line of stability on the neutron-deficient side can be produced through light-ion induced fusion reactions. In this case the advantages are the high cross section of the reaction and the high intensity of the primary beam available. Instead heavy-ion fusion evaporation reactions have typically a much lower cross section, but they produce neutron-deficient nuclei very far from the line of stability.

To produce neutron-rich nuclei in a wide mass range, different beams, as low and high energy protons, heavy ions, fast or thermal neutrons and electrons, are used to induce fission reaction of ^{235,238}U, ^{232}Th and long lived actinides. Usually the cross section of a fission reaction is not very much dependent on the energy of the incoming particle, so with different energy of the primary beams, different secondary beams can be produce with about the same rate [DAR90].

Spallation products can span a large part of the nuclear chart on its neutron-deficient side. The production cross-sections for nuclei very far from stability are modest, but the high primary beam energy (usually proton) allows one to use thick targets (of the order of 100 g/cm^2).

Projectile fragmentation reactions are induced by a high-energy heavy ion beam with energies above 50 MeV/u or a high energy proton beam. These reactions produce a wide variety of isotopes, close to the initial target or projectile nucleus as well as very light nuclei.

It should be noted that direct and light or heavy ion fusion evaporation reactions produce on average a limited number of different isotopes, while the other reaction mechanisms discussed produce hundreds of different isotopes. In general, the choice of the nuclear reaction, used to produce an ion beam of a

particular isotope, depends on its position on the chart of nuclei, but also on its physical chemical properties [DUP06].

2.2.2. Targets and Catcher

The main aim of the target systems is to produce as much isotopes as possible and to release them as fast and as efficient as possible. The diffusion in the target material of the reaction products is strictly connected to the chemical properties of the target systems. Once the exotic nuclei are produced, they are stopped in a solid or gaseous catcher. Often the word “thermalized” instead of “stopped” is used to indicate that the radioactive atoms are cooled down from e.g. about 200 MeV kinetic energy in case of a fission reaction to ~300 meV average kinetic energy corresponding to a catcher temperature of 2000 ^{o}C. In some cases the target and the catcher are the same. After thermalization the radioactive nuclei of interest (partly) escape from the catcher and they are transported towards the ion source. In case of a solid catcher, diffusion from the target/catcher material is followed by effusion towards the ion source. The former process is governed by the diffusion properties of the atoms of interest and of the target/catcher matrix. The effusion is controlled by a combination of factors: pumping through the pores of the target/catcher material and through the connecting tube, sticking times when the atom hits a wall and diffusion properties of the atoms with respect to the wall material. In case the sticking time is long compared to the diffusion time of the atom inside the wall material, it will diffuse and eventually disappear in the walls. To reduce the loss of nuclei, the speed of these processes is increased by heating the target/catcher system, the transfer line and the ion source to a suitable temperature. In this way the diffusion process to the surface of the solid matrix is accelerated and the sticking time at the walls of the target or catcher material and container is reduced.

Thick targets are mainly used in combination with high-energy proton

beams, in particular for light-ion fusion reactions [DUP92, GAE03] and fragmentation reactions [VIL03] thick carbon catchers are exploited as well. Typical targets have thicknesses of a few 100 g/cm^2 and consist of foils (e.g., tantalum), fibres, liquids (e.g., mercury) or powders (e.g., uranium-carbide). The target container is heated, e.g., by sending an electrical current through the container, reaching temperatures around 2000 ^{o}C.

In heavy-ion fusion evaporation reactions the recoil products are stopped in a thin catcher foil heated to high temperatures. For several application carbon is used as catcher material as for many elements the diffusion process is fast and graphite can stand very high temperatures. Still other materials like niobium, tantalum, tungsten and rhenium are used as well. This configuration was used extensively at the GSI ISOL facility [KIR92].

In case of a gaseous catcher, the radioactive atoms of interest stay in the gas phase and there is no need for high temperature systems. These kinds of catchers are widely used in fission or heavy ion fusion evaporation reactions, in which the reaction products are stopped in a noble gas [DUP06].

2.2.3. Ion Sources

Depending on the requirements, several ionization mechanisms are used. In general singly-charged positive or negative ions are produced. In a few cases multiply charged ions are produced as well. Usually the target-catcher-ion source is an unique system. It is put on a positive (in case of beams of positively charged ions) or negative (negatively charged ions) high voltage of typical values between 40 and 60 kV.

Different ionization mechanisms are implemented in the ion sources of ISOL systems. The use of them depends essentially on the ionization potential (W_i) of the element of interest, the required charge state and selectivity.

For isotopes of elements, present in the gas phase inside the ion source,

with W_i>7 eV and for the creation of multiply charged ions, electron impact ionization is mostly used. The atoms or ions are bombarded by energetic electrons, thereby losing one or more of their outer electrons. Studying the cross section for electron impact ionization of atoms as a function of electron energy is possible to optimize the production. This method is used in high-temperature gaseous discharge ion sources, ECR ion sources and EBIS.

A second ionization mechanism is based on surface ionization. When an atom interacts with a heated surface it can lose or gain an electron before leaving the surface as a positive or negative singly charged ion. This technique can be used efficiently for elements with W_i<7 eV for the creation of positive ions (positive surface ionization) and with electron affinity E_A>1.5 eV for the creation of negative ions (negative surface ionization). Using this ionization technique, extreme selectivity can be obtained if isotopes produced in the same nuclear reaction have very different ionization potentials [DUP06].

A method that has been successfully implemented at ISOL systems is resonant laser ionization [DUP97]. During this process the atoms are stepwise excited by laser photons, leading finally to the continuum, to auto-ionizing states or to highly excited states close to the continuum. In the latter case the ionization step is achieved through infra-red irradiation, an electrical field or atomic collisions. The process consists of typically two or three steps. Because of the resonant nature of most of these steps, resonant laser ionization is very efficient and chemically selective. If the laser bandwidth is narrow enough, beams are obtained isobarically and isomerically pure. Details on the principles and applications of resonant laser ionization can be found in [HUR88, LET87].

2.2.4. Mass Separator and Post Accelerator

After the ions are created in the ion source, they are extracted and accelerated in a DC electrical field created by a high-voltage potential difference between the ion source and an extraction electrode or the beam line. Then the low-energy ion beam is mass separated by an analyzing magnet and transported to the focal plan. The focal plane is where, in ideal conditions, the ion beams are focussed after the analyzing magnet. An important property that expresses the quality of the system is the mass resolving power, defined as $R = M/\Delta M$. Here ΔM is the full width at half maximum of a beam of ions with mass M in the focal plane of the separator. The resolving power depends on the properties of the magnet and of the ion optical properties of the ion beam [DUP06]. Typical values for ISOL systems vary from a few hundred to a few thousand. Other properties of the mass analyzing system are discussed in [BRO89].

A “cooler” device is used to cool down the ion beam in order to improve its ion optical properties and in some cases to bunch the ion beam. Cooling should be understood in terms of reducing its axial and radial temperature or more precisely its axial and radial momentum or energy spread. Bunching of the ion beam is often required to increase the peak to background ratio of certain experiments like laser spectroscopy experiments or to inject the beam into a charge-state breeder. There are two distinctive devices used for cooling and bunching: penning traps [BOL97] and radio frequency (RF) coolers [MOO92]. Both systems are based on the storage of the ions using electrical DC and RF fields (RF-coolers) or a combination of magnetic and electrical fields (Penning traps). Buffer gas like helium or argon is introduced inside the system. Through collisions between the buffer gas atoms and the radioactive ions, energy is lost and the ions beams are cooled. This cooling technique has been developed over the last years yielding excellent performance. Efficiencies, defined as the beam intensity of the cooled beam versus the injected beam, over 50% have been reached. Coolers are installed at different ISOL

systems [CLA03, HAB00, HER01, NIE01] for efficient injection into traps as well as for solid-state studies.

The beam of singly charged radioactive ions is accelerated by using a variety of post accelerators (cyclotrons, linear accelerators and tandems). At Triumf and Oak-Ridge laboratories the singly charged ions are accelerated directly and stripping is performed during the acceleration process. For all other projects, charge state breeders are required in order to obtain higher charged ions. They have been developed to boost the 1^+ ion beam to a higher charge state. This process has to be efficient and fast without inducing extra beam contamination from stable isotopes. Two types of charge-state breeding ion sources are used: the Electron Beam Ion Source (EBIS) and the Electron Cyclotron Resonance (ECR) ion source. Both rely on the principle of intense bombardment of the ions with energetic electrons, with electron impact ionization yielding ions in higher charge states. The plasma of ions and electrons is confined through electrical and strong magnetic fields.

2.3 EXCYT facility at LNS-INFN

The EXCYT facility (Exotics with Cyclotron and Tandem) for production and acceleration of radioactive ion beams is available at LNS-INFN, since the end of 2006 (see Figure 2.2). This facility is based on the ISOL method: the K-800 Superconducting Cyclotron drivers the stable heavy ion beams (up to 80 MeV/A, 1 pμA) on a target-ion source (TIS) assembly, and the 15 MV Tandem provides the post-accelerating of the radioactive ion beams produced [RIF08].

The EXCYT facility is able to produce beams with high purity, but the role of the Tandem as a post-accelerator, implies that the reaction products must be ionized negatively in order to be accelerated by it. Since nowadays, many efforts were focused on Li^8 yield. The production of the radioactive ions is performed by injecting a $^{13}C^{4+}$ primary beam of 45 MeV/A on a graphite target up to a beam

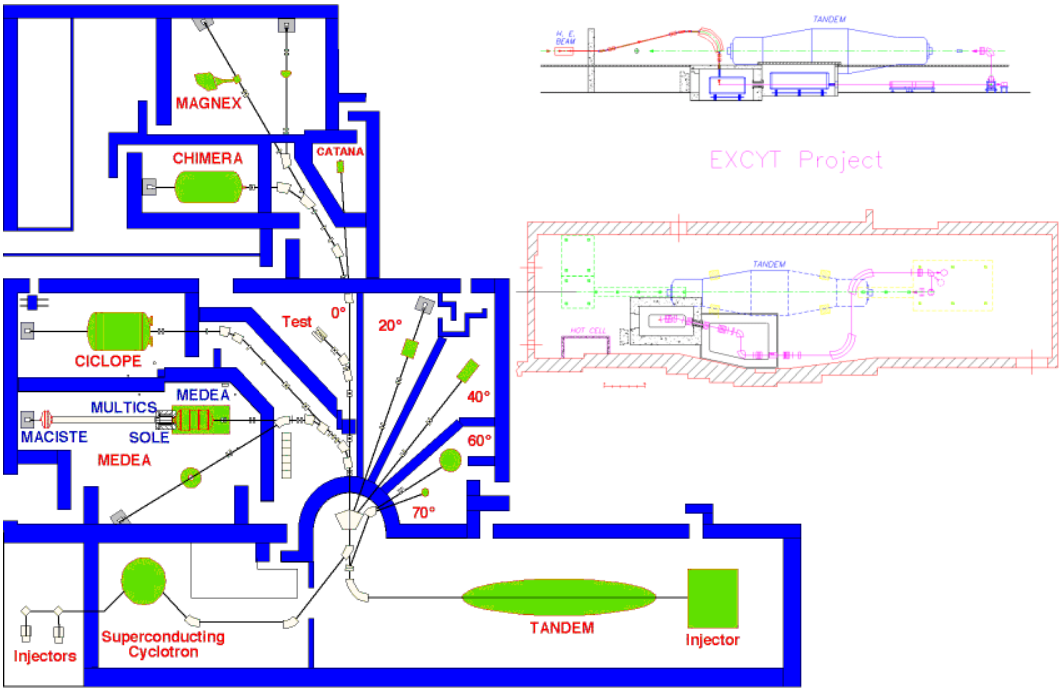

Figure 2.2 Layout of the LNS-INFN laboratory and ECXYT facility [LNSW].

power of 150 W, while the ionisation of ^{8}Li is achieved by a Tungsten positive surface ioniser. For such a kind of ion beam, the highest extraction efficiency from the TIS is obtained by positive ionisation. Then the post-acceleration with the Tandem is possible only after a charge exchange cell (CEC) to obtain negative ions. The CEC consists of a cell containing Caesium vapours, which interact with the ^{8}Li beam converting its charge from +1 to –1 by a two step reaction. The Li^{+} beam has been produced at different energies to cross-check the transmission efficiency together with the charge exchange efficiency.

The maximum ^{13}C primary beam intensity was 1 era, which corresponds to a beam power of 147 W leading to a production yield of 9×10^{6} pps of ^{8}Li. Table 2.1 summarizes the production yields at the entrance of the first stage of isobaric separation. The yields of ^{9}Li and ^{21}Na are also reported even if measured in not optimized conditions.

The Target Ion Source Complex is made of graphite enclosed in a tungsten container and heated by a surrounding electrical heater. The recoils produced in

the target will effuse through the transfer tube to the ionizer, where they are ionized by an ISOLDE-type ion source and then extracted by an acceleration voltage up to 50 kV. The sources available for the TIS are the Hot Plasma Ion Source (HPIS), which is suitable to ionize positively many elements, included noble gases with an efficiency of about 1%, and the surface ionization type sources for positive and negative ion production. The positive (PIS) is particularly suitable for alkaline ions for which it is highly selective and efficient, while the negative (NIS) is indicated for halogens with exception of fluorine. The source presently used is the PIS (efficiency measurements indicate an ionization rate around 70% for Lithium beam) [RIF08]. The selection of target material has been done following the criteria of high porosity, small grain size, high thermal conductivity, high chemical purity, high melting point and low vapour pressure.

The first target prototype used for the preliminary test at SPIRAL in GANIL and at LNS-INFN during March 2006 is shown in [MEN05]. It consists of two parts: the upper tablet and the lower part which acts also as mechanical support. The transfer tube to the ionizer is located in between these two parts. Sizes were chosen to maximize the Li collection (diameter=8mm, high=3.5 mm). To improve the production the target design was modified by employing ten, uniformly spaced, 1 mm thick, graphite disks. Further investigations are planned to improve knowledge about the Li release mechanism from the target. Other target candidate materials such as fibres, felts and nano-structured materials are taken into consideration.

Using a primary beam of 100 W, a beam intensity $5.4 \cdot 10^6$ pps of $^8Li^+$ is produced. After the CEC, $1.5 \cdot 10^5$ pps of $^8Li^-$ are transported through the mass separator until the Tandem entrance. The transport

Table 2.1 ^{8}Li, ^{9}Li and ^{21}Na Measured Yields at the Entrance of First Stage of Isobaric Separation [RIF08].

Beam	Beam Power	Intensity
^{8}Li	147 W	$9 \cdot 10^6$ pps
^{9}Li	82 W	$3.4 \cdot 10^5$ pps
^{21}Na	82 W	$3.7 \cdot 10^5$ pps

efficiency through the two stages of the isobaric mass separation is close to 100% as expected. The acceleration transmission at the Tandem is of the order of 50%, lower than with Li stable beams. Therefore some improvements are planned in the injection line of the Tandem, possibly the installation of a new quadruplet. The final intensity of ^{8}Li on target is $5 \cdot 10^{4}$ pps [RIF08].

An overall optimisation process involves several key points of the facility (CS, TIS, CEC, Tandem). This will permit a significant increase of the beam intensity on target. In particular an ^{8}Li intensity up to $5 \cdot 10^{5}$ pps can be expected. Besides, the installation of a different source type is planned in the near future: the aim is to start developing a new radioactive beam, different from ^{8}Li, which can be of scientific interest for researcher, as it could be ^{15}O.

2.4 In-flight fragmentation (IFF) of projectile

By the ISOL method, fragments are produced almost at rest in thick targets and can be used for experiments at low energy or may be re-accelerated by a post accelerator. Radioactive beams at energies larger than 30 MeV/A have been produced so far at heavy ion accelerators by using the IFF. This technique relies on the forward focusing of the products of peripheral nuclear reactions and on the selection, in flight, by electromagnetic devices, of the different produced species. RIBs, including the short living ones, produced by the IFF technique are directly available for experiments [RAP07].

In this method the primary beam passes through the production target and retains a large fraction (~90% or more) of its initial kinetic energy. Therefore, an advantage of IFF techniques is that beams can be produced and delivered at high energy without the need for reacceleration. The process can be extremely efficient and the production target only needs to be able to dissipate a fraction of the beam power. The unreacted beam is collected at some other point in the separator itself.

A distinct advantage of this method is that the purity of the secondary beams can be improved by passing the ions through profiled energy degraders at an intermediate dispersive point [GEI89, SCH87]. This can, in most cases, eliminate mass-to-charge ambiguities and provide essentially pure secondary beams for even the heaviest elements.

One final significant feature of IFF is that the process is not sensitive to chemical properties or, in general, to the half-life of the isotopes of interest. The limitation on the half-life is only given by the flight time of the ions through the device, which is usually longer in the in cooler rings. The net result is that, given suitable ion optics, the efficiency of the IFF separation techniques can reach essentially 100% [MOR04].

Below it is described the general feature of this method and the availability of these beams at LNS-INFN in Catania.

2.4.1. Reaction mechanisms

The three principal reactions involved in the radioactive beam production are: projectile fragmentation, projectile fission and nuclear fusion.

Projectile fragmentation process involves a peripheral interaction of the projectile with a target nucleus. In this process some nucleons are removed and the excited residue undergoes small recoil from the removal and isotropic recoil from the de-excitation. Coulomb deflection and the nuclear recoil of the ion are small so that the large initial velocity can focus all the products into a narrow cone. The mass, charge, and velocity distributions of the residues have been equally well described in microscopic nucleon-nucleon scattering models or in macroscopic abrasion framework partly because all the models predict the creation of excited primary residues that must undergo statistical de-excitation [MOR79].

A macroscopic model based on the removal of nucleons in the volume eclipsed by the target and projectile and the subsequent de-excitation of the

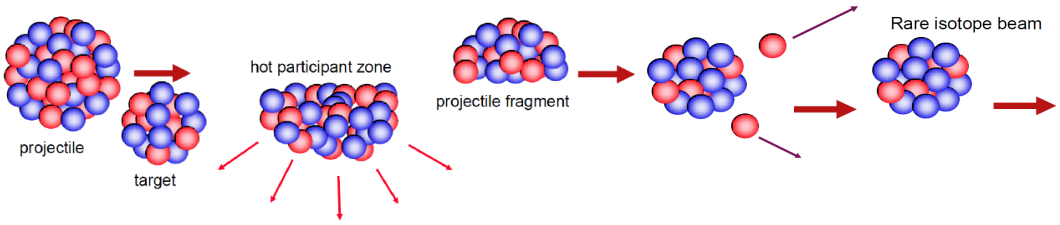

Figure 2.3 Schematic view of the projectile fragmentation. Accelerate heavy ion beam passes through a thin target to achieve random removal of protons and neutrons in flight. The projectile fragments cool by evaporation giving rare isotope beams [LIS10].

primary products also has been successful [BOW73, GOS77]. This approach is called alternatively the participant-spectator model or, more commonly, the abrasion-ablation model. The target nucleus is imagined to shear off part of the projectile, leaving the rest of the projectile to travel forward at the initial beam velocity, with a minor down-shift in velocity and some excitation energy (see Figure 2.3). The primary residues (projectile or target) then undergo statistical de-excitation processes leading to the observed products [MOR78].

A remarkable feature of the observed fragment cross sections is that they are relatively constant from approximately 40 MeV/nucleon to 2 GeV/nucleon with the exception of the fragments whose mass number is lower than, but still close to that of the initial nucleus [SOU02, ENQ02]. The cross sections are largest for fragments close in mass, but lower, than the initial nucleus and decrease exponentially with decreasing mass number.

An example of the broad range of fragments that can be observed in a single setting of a separator is shown in Figure 2.4 from the work of Pfaff et al. [PFA96].

Although projectile fragmentation is used to produce light neutron-rich nuclei, the maximum yield of projectile fragmentation products is obtained for neutron-deficient nuclei. On the other hand, nuclear fission has been an extremely important source of neutron-rich nuclei for a long time. The fission process creates nuclei with a kinetic energy of approximately one MeV/u in the rest frame of the fissioning nucleus and the angular distribution of products is essentially isotropic

for low values of angular momentum. Thus, the recoil vectors of the products are distributed on the surface of a slightly diffuse sphere. When the fissioning nucleus is moving with a kinetic energy that is large compared to the fission recoil, then the products can be collected and separated using IFF techniques in the similar way used for projectile fragments. However, generally only one or the other kinematics solution, e.g., forward-going or backward-going in the rest frame, can be accepted by present separators. Even with this limitation the fission of very energetic projectiles is an important process for the production of neutron-rich nuclei due to the lack of other methods to produce these nuclei [MOR04].

Another reaction used to the production of exotic beams is the nuclear fusion reactions. In this case the products have linear momentum that is significantly lower than the primary beam ones. Usually the secondary beams are collected by recoil separators, which often employ electric fields to select the fragments velocities, and preserving the mass-to-charge ratio [DAV89, NOL85, TRIB89]. This production method is less used because the beams from these recoil separators suffer from some contamination. Indeed the separation technique is sensitive to the atomic mass-to-charge ratio of the ion and not strictly to the nuclear mass-to-proton number ratio of the ion. Besides different charges states of a given isotope will be separated decreasing the collection efficiency.

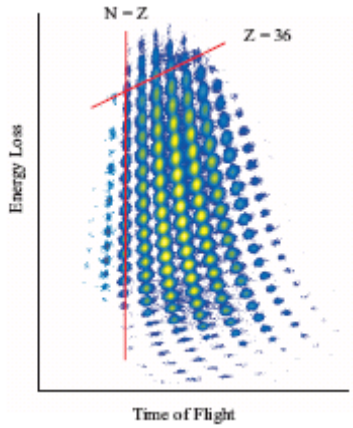

Figure 2.4 The projectile fragments observed in one setting of the magnetic rigidity in the A1200 separator from the reaction of ^{78}Kr with ^{9}Be at 70 MeV/u are shown as a function of energy-loss and time-of-flight. The vertical line indicates the position of nuclei with N=Z and the diagonal line indicates the positions of krypton isotopes [PFA96].

2.4.2. Targets

The influence of the target material on the fragment yields comes from the interplay of the nuclear cross section and the perturbation of the beam properties by electronic interactions (energy loss and multiple scattering). Usually target materials with low Z are preferred.

The ion optics of fragment separators (discussed in the next section) require that the width of the beam spot on-target be approximately less than 1-mm to allow high selectivity in the separation and purification of the secondary beams. In general the beam energy is delivered to a target volume of the order of a few cubic millimetres. Dissipation of the thermal heat delivered to fragmentation targets in such small volumes, can become an important problem. Advanced designs for cooling targets have included a rapidly rotating graphite wheel in operation from some time at GANIL [SAV96] and new designs of similar systems for the big-RIPS [KUB03] and for the super-FRS [GEI03] separators. Some work suggests that liquid lithium is another choice for target material partly because it is also an excellent cooling medium [NOL03]. Since the density of beryllium is about four times that of lithium, the combination of beryllium metal with liquid lithium cooling could be used to provide a contained target system [MOR04].

2.4.3. Fragment separator and profiled degrader

One of the largest difficulties of beams produced by projectile fragmentation is that the secondary beam emittance[2] is unavoidably large due to the random recoil momentum of the fragments created by the nuclear reaction. This emittance is reduced with increasing beam velocity. Moreover, the resulting energy and angular spreads of the radioactive nuclei beams are much larger than those of a standard beam from an accelerator (by a factor ten or more). In fact, the

[2] emittance is an important property related with the optical quality of the ion beams. In general the 95% radial emittance of an ion beam is defined as the area of an ellipse that contains 95% of the beam intensity.

total emittance of secondary beams is determined by the combination of the nuclear reaction kinematics and atomic processes such as multiple angular scattering and energy loss straggling in the production target and in any degrader.

The highest resolving power for the various fragments is obtained if the system is achromatic. The term achromatic means that the horizontal position and angle of a particle at the end of the separator does not depend on its momentum. Achromatic systems have the advantage that the final spot size is kept small even when the momentum acceptance is large. The Figure 2.5 illustrates the basic ion-optical concepts of fragment separation in a momentum-loss achromatic with one stage of filtering. The ion trajectories for different momenta and initial scattering angles of the same isotope are indicated by the lines in the figure. Note that the ions are focussed to a small spot at the final focal plane of the device, independent of the initial angle or momentum. The key elements in the device are an initial bend for momentum-to-charge ratio selection and beam rejection, an energy loss degrader for atomic number separation, also called a 'wedge', and a second bend for momentum-to-charge ratio selection of a specific ion.

The angular acceptance can be set by an aperture after the target or simply by the quadrupole magnets themselves at the beginning of the device. The momentum acceptance of the device is generally limited by the magnet bores or by an aperture at the intermediate position. Since the fragmentation nuclei are produced at nearly the same velocity, the Lorentz formula ($B\rho=p/q=mv/q$) sets the initial value of the magnetic rigidity given by the mass to charge ratio separation.

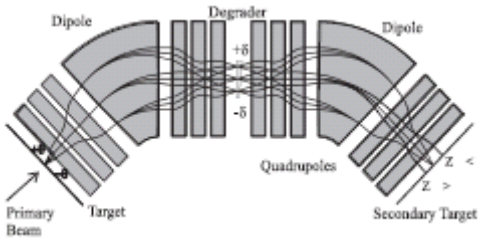

Figure 2.5 Schematic representation of the ion-optics used in a momentum-loss achromat to separate projectile fragments [MOR04].

An energy degrader can be inserted into the beam at the intermediate momentum-dispersive image. It breaks the ambiguity among the ions that have the same initial mass-to-charge ratio, because the energy lost

in the material will depend on MZ^2/E or $(Z/v)^2$. The momentum lost will be approximately proportional to (Z/v). Again, because the ions have approximately the same velocity they will lose different momenta in the degrader depending on their atomic number and they will exit from the foil with different magnetic rigidities. The contaminants can then be dispersed at the focal plane by an additional bend.

The mass resolving power of a fragment separator can be expressed in first order as [MOR04]:

$$R_{mass} = \frac{(x/\delta)_1}{(x/x)_1 \cdot x_0} \cdot \frac{(\delta/\delta_m)}{(\delta/\delta_0)} \qquad 2.1$$

where $(x/\delta)_1$ is the dispersion of the first set of dipoles; $\delta = (p - p_0)/p_0$ is the percent momentum deviation from the central momentum; $\delta_m = (m - m_0)/m_0$ is the percent change in the momentum caused by a percent change in mass respect m_0; x_0 is the initial spot size at the degrader, and $(x/x)_1$ is the magnification at the dispersive image. In each case the subscript 0 denotes the value for the central ray. A similar expression can be written for the charge resolving power [MOR04]:

$$R_{charge} = \frac{(x/\delta)_1}{(x/x)_1 \cdot x_0} \cdot \frac{(\delta/\delta_z)}{(\delta/\delta_0)} \qquad 2.2$$

where $\delta_z = (z - z_0)/z_0$ is the percent change in the momentum caused by a percent change in the atomic number, z_0, at the degrader with the mass and momentum held constant. Equations 2.1 and 2.2 are valid for an achromatic system with the condition:

$$(x/\delta)_2 = -(x/x)_2 \cdot (x/\delta)_1 \qquad 2.3$$

It's important to note that the first term in both equations 2.1 and 2.2 for the resolution is simply the momentum resolving power of the first half of the separator. Hence, lower momentum resolving power always implies less pure secondary beams. To obtain mass resolving powers of the order of 200, the intrinsic momentum resolving power of the device should be 1000 or greater. This

requirement has important consequences for the design of the separator and indicates that the emittance of the primary beam should be as small as possible in order to reduce the spot size, x_0, and thus increase the resolving power. In general, it is not necessary to use degraders with achromatic profiles. An alternative approach is to use a "homogeneous" or flat degrader and to tune the magnetic components of the second half matching the dispersion of the beam after the flat degrader.

Very fast projectile fragment beams, kinetic energy per particle ~200 MeV/nucleon, can be thermalized by depositing the bulk of their energy in a solid foil and the remainder in high pressure helium gas [SCH03] in order to basic studies of the existence, half lives, and decay properties of the ions produced. However, there are two difficulties in just stopping the ions in a buffer gas: first, the density of a typical gas is about 1000 times lower than that of a solid causing the range distribution to be spread over large distances, second, the broad momentum distributions of ions from projectile fragment separators (several percent in most cases) will spread the large range distribution of a mononenergetic ion in gas over even larger distances. In different fragmentation facilities, fast ions are collected in buffer gases. In these systems the fast ions lose nearly all of their kinetic energy in a degrader foil/entrance window and go into the gas cell filled with high-purity helium. These degraders have to be very carefully prepared because imperfections in the solid on the order of a few μm turn into tens of mm in a gas. The ions will lose the remainder of their kinetic energy in the gas and will capture electrons during the final deceleration and become thermalized.

2.4.4. Computer Simulation

Several programs exist to calculate the performance of in-flight separators and the expected yields. The most commonly used program is LISE++ [TAR08]. LISE++ includes the parameters of the general configurations for most of the

existing fragment and recoil separators. For a new design, a program such as TRANSPORT is used to calculate the first order beam optics and these parameters are input into LISE. More sophisticated programs that include higher order optics and secondary reactions are also available. The most readily available and reliable code of this type is MOCADI [IWA97].

2.5 Outlook facilities

At present a large number of facilities are modifying and/or upgrading their present capabilities to be able to produce radioactive beams using one of the two methods. Different new projects in Europe and in the world are through the scientific study but are awaiting possible agreement on funding and a number are in the construction phase.

In the United State, the Fragmentation Radioactive Ion Beam (FRIB) project will offer measurements with fast, stopped, and reaccelerated beams of rare isotopes. At Michigan State University (MSU), the existing National Superconducting Cyclotron Laboratory (NSCL) facility folded driver linac accelerator, deliver uranium with energy up to 200 MeV/u and lighter ions with increasing energy (protons at 600 MeV). The upgrading will allow to reach 400 MeV/u for uranium and 1 GeV for protons (400 kW) [FRIBW].

The High Intensity and Energy ISOLDE project (HIE-ISOLDE) at CERN, Geneva (Switzerland), is a major upgrade of the existing ISOLDE and REX-ISOLDE facilities. The objective is the increasing energy up to 10 MeV/u of the delivered radioactive ion beam (RIB). This project aims to fill the request for a more energetic post accelerated beam by means of a new superconducting linac [HIEW].

The Facility for Antiproton and Ion Research (FAIR) project in Darmstadt (Germany) is a particle accelerator complex. The facility is an integrated system of particle accelerators which will provide high energy and high intensity beams of

ions of all stable and unstable chemical elements (from hydrogen to uranium, ions up to 35-45 GeV/u and antiprotons 0-15 GeV/c) with unprecedented quality. Moreover derived beams of short-lived nuclei and antiproton beams will be available [FAIW].

The SPIRAL2 project, at GANIL (France), is based on a multi-beam driver in order to allow both ISOL and low-energy IFF techniques to produce RIB. A superconducting light/heavy-ion linac accelerates deuterons up to 40 MeV and heavy ions up to 14.5 MeV/u. They are used to bombard both thick and thin targets. The production of high intensity RIB of neutron-rich nuclei will be based on fission of uranium target induced by neutrons, obtained from a deuteron beam impinging on a graphite converter or by a direct irradiation with a deuteron, ^{3}He or ^{4}He beam. The post acceleration of RIB in the SPIRAL2 project is assured by the existing CIME cyclotron, which is well adapted for separation and acceleration of ions in the energy range from about 3 to 10 MeV/u for masses A~100-150 [SPIW].

In addition, the nuclear physics community is working on a common design for a future European Isotope Separation On Line Radioactive Ion Beams (EURISOL) project.

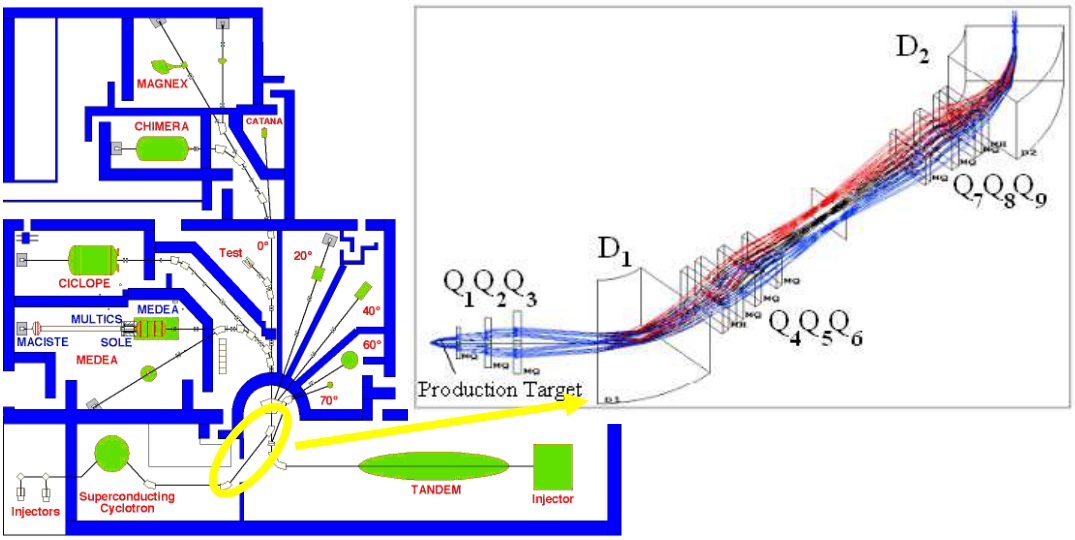

Figure 2.6 Layout of the LNS and the Fragment Recoil Separator used to select exotic beams

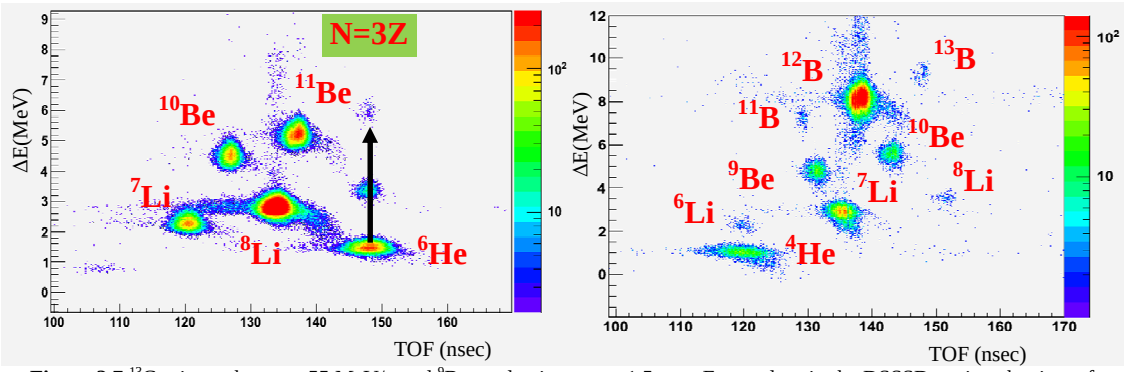

Figure 2.7 ^{13}C primary beam at 55 MeV/u and ^{9}Be production target 1,5 mm. Energy loss in the DSSSD against the time of flight between the silicon detector and the MCP. The picture corresponds to the magnetic field configuration to optimize the ^{11}Be transport. The lower one corresponds to the optimization of ^{12}B. The black line shows element with the same time of flight.

In Italy both the ISOL and IFF facilities are available. At LNL-INFN, there is a new project called Selective Production of Exotic Species (SPES). This consists in the production of protons at 30-70 MeV (delivered by a new cyclotron under construction), impinging on different targets of UC_x. The exotic fission products are accelerated by the already existing LINAC ALPI (A~100 at 12 MeV/u).

In particular in the next section it'll be shown the main characteristic of the in-flight radioactive ions beams facility running at the LNS-INFN in Catania. The measurements of the beam production are part of this thesis subject.

2.6 Exotic beams produced by IFF method at INFN-LNS

In-flight production of RIBs at LNS-INFN was achieved by projectile fragmentation on light targets at incident energies in the range of 40 to 62 MeV/A [RAP07]. In particular, fragmentation reactions of stable beams accelerated by the LNS-INFN Superconductive Cyclotron (SC) at 55 MeV/u (^{13}C, ^{16}O, ^{18}O) at 55 MeV/u were studied. Production targets of ^{9}Be with thickness ranging from 0.5 to 2500 μm have been used. In the production of RIBs by the IFF method, the key role is played by the Fragment Recoil Separator (FRS), which is a magnetic filter which selects, according to their magnetic rigidity, the fragments produced in the

reaction. In the IFF method the standard extraction line of the accelerator was employed as FRS, since it was already built as an achromatic fragment separator. The FRS consists of two bending dipole magnets D_1 and D_2, three quadrupoles triplets Q_1-Q_3, Q_4-Q_6 and Q_7-Q_9, two sextupoles correctors S_4, S_9 near quadrupoles Q_4, Q_9 (see Figure 2.6). A degrader could be placed at the intermediate focus [RAP07].

During 2009 different experiments were performed to study the opportunities offered by such beams using 4π CHIMERA multidetector. A tagging system made of a Double Side Silicon Strip Detector (DSSSD) and a MicroChannel Plate (MCP) was developed for CHIMERA array. The measure of the "time of flight" and the energy loss allows the isotopic identification of the beams. More details about the two detectors and the measurement technique will be described in the next chapter.

Beams around ^{11}Be region were obtained with ^{13}C, and ^{18}O primary beams

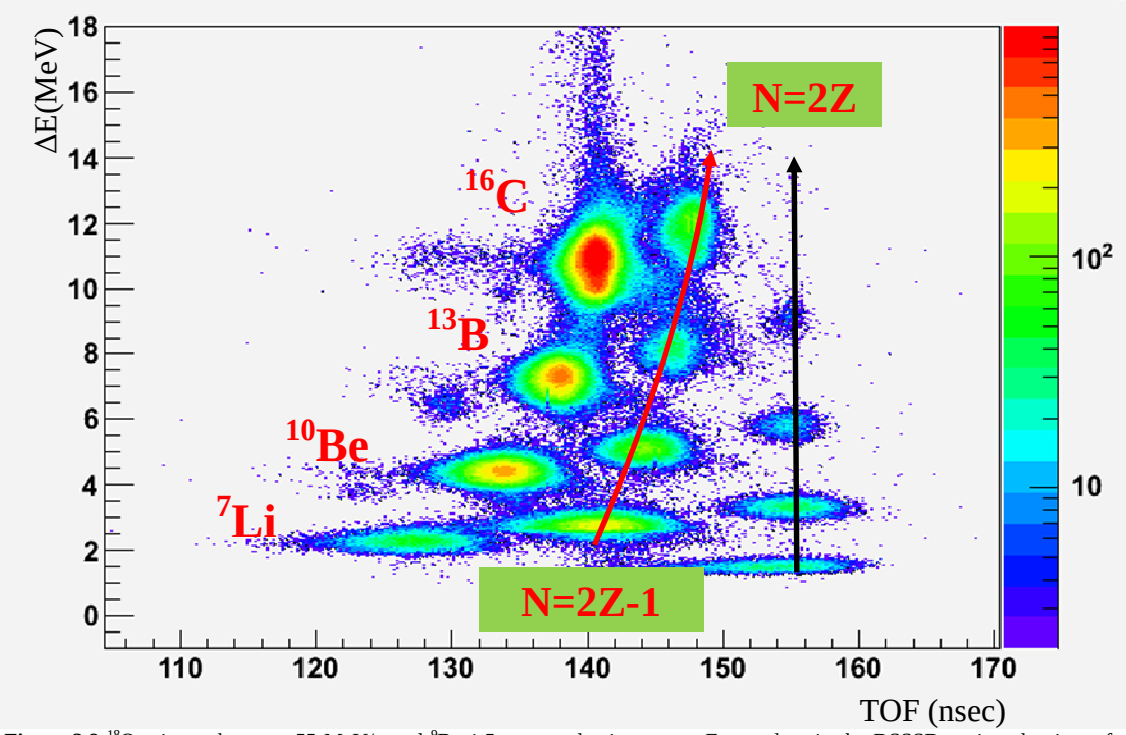

Figure 2.8 ^{18}O primary beam at 55 MeV/u and ^{9}Be 1,5 mm production target. Energy loss in the DSSSD against the time of flight between the silicon detector and the MCP. The black line shows elements with the same time of flight.

at 55 MeV/u and ^{9}Be production target thick 1,5 mm. ^{13}C primary beam at 55 MeV/u impinging on a ^{9}Be target produces ^{11}Be and ^{12}B with rate around 10 kHz, optimizing the corresponding magnetic fields of the transport for two different configuration (see Figure 2.7). ^{18}O primary beam impinging at the same production target can produce also ^{11}Be with less intensity (3 kHz), but more neutron rich beams like ^{16}C with higher rate (see Figure 2.8). The Table 2.2 shows the different beams rate produced by the two primary beams ^{13}C and ^{18}O.

Table 2.2 Characteristics of the produced fragmentation beams. * Intensity is normalized to a primary beam of 100 Watt.

Primary beam (55 MeV/A)	^{9}Be production target thickness (mm)	Secondary beam and energy	Intensity (kHz)	Abundance
^{13}C	1.5	^{11}Be 48 MeV/A	10 *	50%
^{13}C	1.5	^{12}B 47MeV/A	160	80%
^{16}O	1.5	^{15}O 31 MeV/A	5	10%
^{16}O	1.5	^{14}O 36MeV/A	0.7	1.5%
^{16}O	2.5	^{17}F 24MeV/A	10	20%
^{18}O	1.5	^{16}C 50 MeV/A	9	30%
^{18}O	1.5	^{13}B 52MeV/A	4.5	15%
^{18}O	1.5	^{11}Be 48MeV/A	3*	10%
^{18}O	1.5	^{10}Be 56MeV/A	4.5	15%
^{18}O	1.5	^{8}Li 51MeV/A	3	10%

The optimization of the beams transport is a difficult task because of the lack of an efficient transport monitor system. To optimize the transport up to the scattering chamber, the pilot beam technique has been used. This method consists using a beam with the same magnetic rigidity of the exotic beam desiderate. Indeed ^{11}Be has approximately the same magnetic rigidity of the primary beams itself ($^{13}C^{5+}$ and $^{18}O^{7+}$ beams at 55 MeV/u).

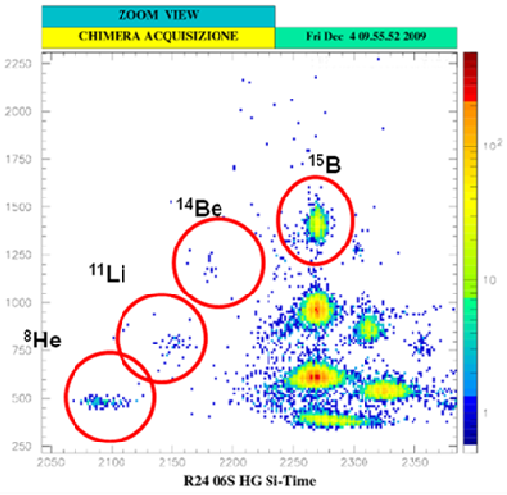

Figure 2.9 Scatter plot ΔE-TOF. ^{18}O primary beam at 55 MeV/A impinging on a ^{9}Be production target [AGO09].

The primary beams are characterized by magnetic field with a Bρ of 2.817 and 2.785 Tm respectively, very near to the values foreseen by LISE++ calculations (2.780 and 2.710 Tm). In general, the transport of neutron rich beams is impossible using this technique. It could shift the currents value of the magnetic dipoles and quadrupoles using the reference points given by the primary beam. In this way it cannot take into account non linear behaviour of the magnetic field, when rather large changes in currents are set.

As an example the Figure 2.9 shows the production and identification of nuclei as ^{8}He, ^{11}Li, ^{14}Be, and ^{15}B. The production of these nuclei can be possible, even if the efficiency of their transport in the CHIMERA beam line is very low, due to the large changes necessary on the Bρ setting of the magnets. To improve the transport efficiency a new system for the transport diagnostic has been implemented and will be tested on 2011. The aim is the optimization of the diagnostic system. It will allow to control in real time the beam intensity and the two-dimensional beam profiles. The aim is to optimization of the beams transport efficiency along the beam line. This system maximizes the intensity until to the scattering chamber.

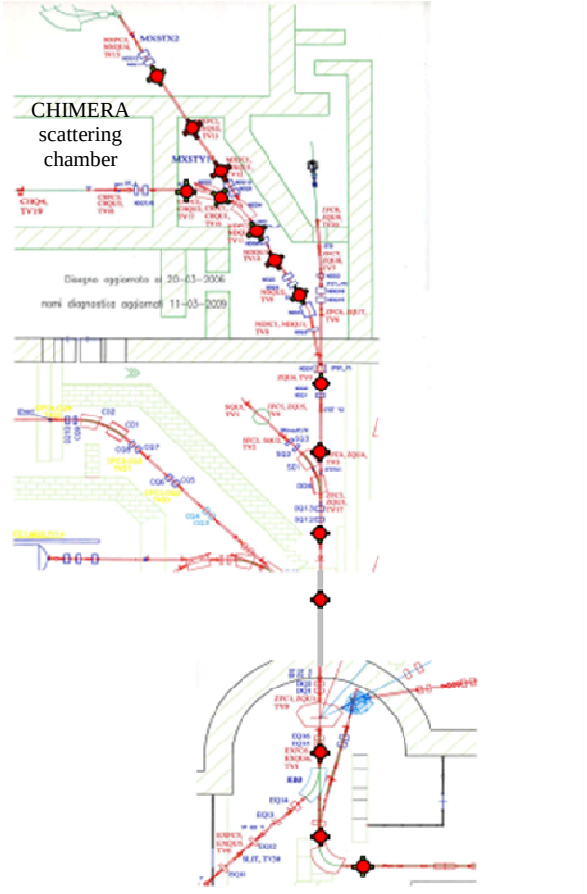

Figure 2.10 Schematic view of the beam line. The diagnostic

The diagnostic devices are made of plastic scintillators and DSSSDs. The scintillator measures the beam intensity (lower than 10^{6} pps), the DSSSD allows to

visualize the spatial beam profile. The Figure 2.10 shows the positions of each diagnostic device installed along the beam line until to the CHIMERA multidetector. In order to optimize the intensity of beam transport and its focus, the two detectors are installed in pair. Another device that will be installed in two points of the beam line is a Fiber Ion Beam Based Sensor (FIBBS). It is a device based on scintillating fibres, it scans the beam allowing to acquire the horizontal and the vertical beam profiles with sensitivity below 10^3 pps [COS09].

Another upgrading of the FRS is going and will be ready at the beginning of 2011. All the transport beam line from the Cyclotron up to the switching magnet has been dismounted and rebuilt in order to insert new larger acceptance quadrupoles and some sextupole. The new beam line has been studied in order to increase the acceptance of the fragmentation beam. A factor from 10 to 40 is foreseen for the increase of the beam transport efficiency. New tests are scheduled on middle February until 10^{th} March 2011, in order to check the overall efficiency of the new system.

CHAPTER 3 – The CHIMERA array

3.1 The 4π CHIMERA multidetector

The CHIMERA (Charged Heavy Ion Mass and Energy Resolving Array) is a multidetector to study heavy-ion collisions in the intermediate and low energy range [PAG01]. It is a 4π multidetector array for charged particles, at present installed at Laboratori Nazionali del Sud of INFN in Catania (Italy), made of 1192 detector telescopes and covering the 94% of the total solid angle (see Figure 3.1 and Figure 3.2) [AIE95, PAG01, PAG04].

The detector measures polar and azimuth angles, energy, velocity, and isotopic identification of almost all the detected particles. The identification method employed are four:

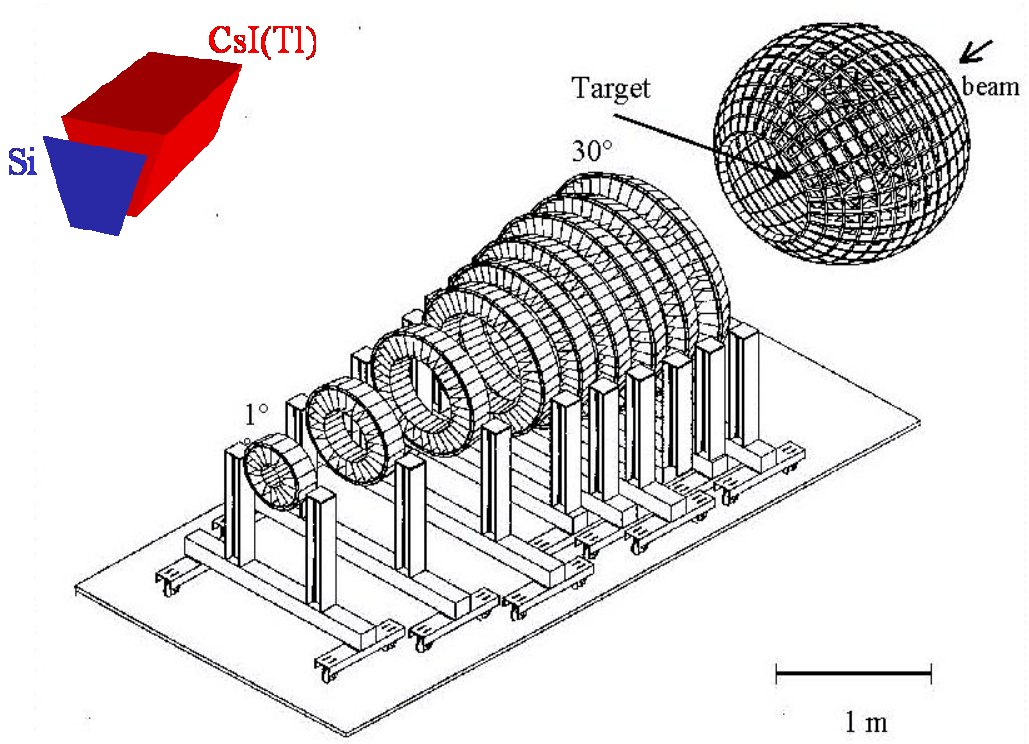

Figure 3.1 Schematic view of the CHIMERA multidetector. The target is set inside the sphere. On the top a schematic view of a telescope.

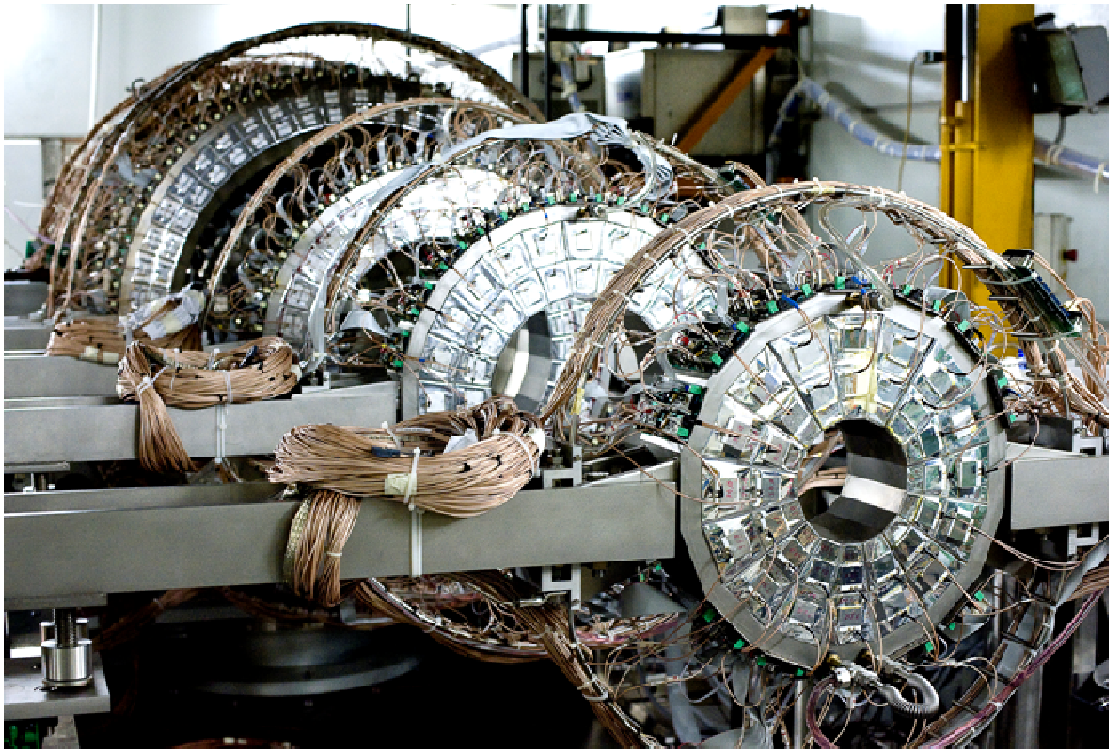

Figure 3.2 Recent photo of the CHIMERA multidetector with sphere and five rings. The other four rings of the forward part have been transferred at GSI.

- ΔE-E, charge identification of the particles punching through the silicon detector and stopped in the CsI(Tl). Mass identification for particles with Z≤9.

- ΔE-TOF (Time of Flight), mass identification, velocity and energy measurement of the particles stopped in the silicon detector.

- PSD (Pulse Shape Discrimination) in CsI(Tl), isotopic identification of light charge particles.

- PSD (Pulse Shape Discrimination) in Silicon detector, charge identification of the particles stopped in the Silicon detector.

Besides, the CHIMERA multidetector is characterized by a low energetic detection threshold (less of 0,5 MeV/u for heavy ions and 1 MeV/u for light particles). In particular in Table 3.1 are shown the threshold values considering the

particles involved and the identification method.

Table 3.1 Detection thresholds of the CHIMERA multidetector against the identification method for charge light particles.

Z≤3			**3<Z<10**		
Energy (MeV/u)	Technique	Identification	Energy (MeV/u)	Technique	Identification
E <6	TOF	A	E <12-15	TOF	A
6< E < 15	ΔE-E	Z e A	E >12-15	ΔE-E	Z e A
15< E <Emax	PSD in CsI(Tl)	Z e A	4 < E < 6	PSD in Si	Z

3.2 The Tagging System

It has been shown in the chapter 2 that fragmentation beams are available at LNS-INFN in Catania. Event by event identification of the incoming beams is obtained by the tagging system implemented in CHIMERA apparatus. This tagging consists of a MicroChannel Plate (MCP) and a Double Side Silicon Strip Detector (DSSSD). They are set along the beam line at the entrance of the CHIMERA scattering chamber, with a base of flight of 12.9 meter (see Figure 3.3). The MCP gives the start time reference, the DSSSD give the stop time reference and measures the position of the impinging beams and their energy loss.

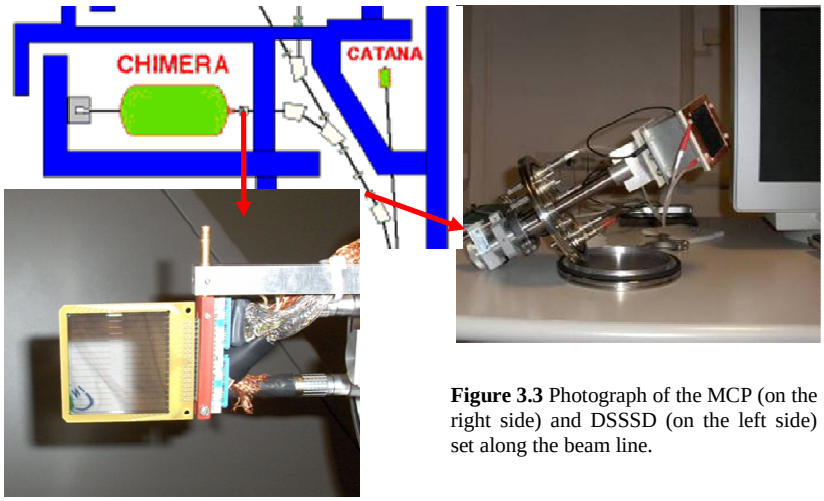

Figure 3.3 Photograph of the MCP (on the right side) and DSSSD (on the left side) set along the beam line.

3.2.1. MicroChannel Plate

In general these kinds of detectors are largely used in nuclear physics for time measurements thank to their prompt answer [CUN07, MON05, FIG91]. The MCP has been assembled at LNS-INFN using the bare micro-channel glasses (43 x 63 mm, 700 micron thick), produced by the Topag Lasertechnik. They has been mounted in chevron configuration, the electrical contact are set into the groove of a plastic frame. A mylar foil (2 μm thick) with an evaporation of LiF (15 μg/cm^2) is the source of electrons. When the beam impinges the foil, it causes the escape of electrons from this surface. They are driven by a uniform electric field until arriving on the upper surface of the MCP glasses that multiply the electrons collected. The electron drift region is realized with an aluminium box supporting a metallic grid (biased at the same potential of the upper surface of the MCP). Then the signal emitted from the MCP is collected by a planar copper anode. The future upgrading consists in a MCP position sensitive, where grid and rear of the MCP will be supplied through a resistive divider [PIR01,MUS06].

The bias applied is 4000 V, enough to get 100% efficiency with a calibration α source (the α energy loss punching through the LiF is about 115 keV/μm). The efficiency of light fast ions is lower (see Figure 3.4), and it is not easy improve the results. In fact for instance, increasing the electric field applied to the MCP system from 4000 to 4500 V, it produces an increase of only 2% of the efficiency for ^{6}He ions. This is due to the small number of electrons emitted by the foil and probably also by the quite

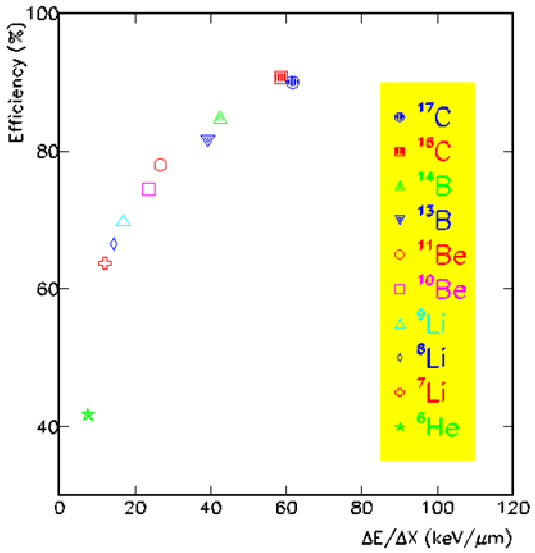

Figure 3.4 Efficiency plot for intermediate energy fragmentation beams detected by MCP. The abscissa represents the specific energy loss in the mylar foil [GRA08].

high velocity of emitted electrons, strictly related to the beam velocity [DEF08].

3.2.2. Double Side Silicon Detector

The DSSSD is a position sensitive silicon detector produced with planar process, where a series of narrow parallel strip electrodes have been superimposed on one surface using ion implantation and/or photolithography techniques (see Figure 3.5). Since electron-hole pairs, created within the volume of the detector, travel along field lines to the corresponding electrode segment, a strong signal is derivated only from those segments that have collected appreciable charge carriers [KNO00].

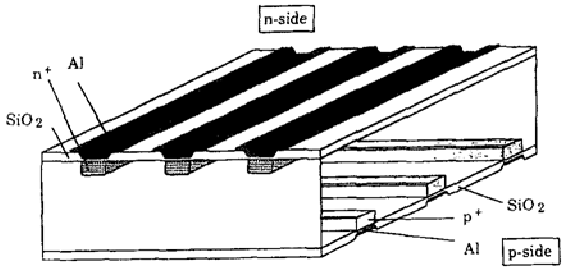

Figure 3.5 Schematic picture of a double side silicon strip detector. [HUB91]

The DSSSD used is provided by the Micron Semiconductor Ltd. It is 50x50 mm^2 area and 140 μm thickness, with 16 vertical strips in the front side and 16 horizontal ones in the rear side, therefore the beam position sensibility is about 3x3 mm^2. The DSSSD is placed, on a movable arm, along the beam line, around 90 cm before the entrance of the CHIMERA scattering chamber (see Figure 3.3).

3.3 The electronic chains

The signals coming from the detectors are processed, transforming them in such a way that they can be read by the acquisition system. The electronic chain can be schematized in two different chains of the signals coming from the silicon detectors and CsI(Tl). The basic electronic chain of silicon detectors, with the relevant parameters, is sketched in Figure 3.6. A charge preamplifier (P.A.C.), customized for timing measurements with high capacitance detector, provides a first amplification of signal. The charge preamplifier integrates the signal of the

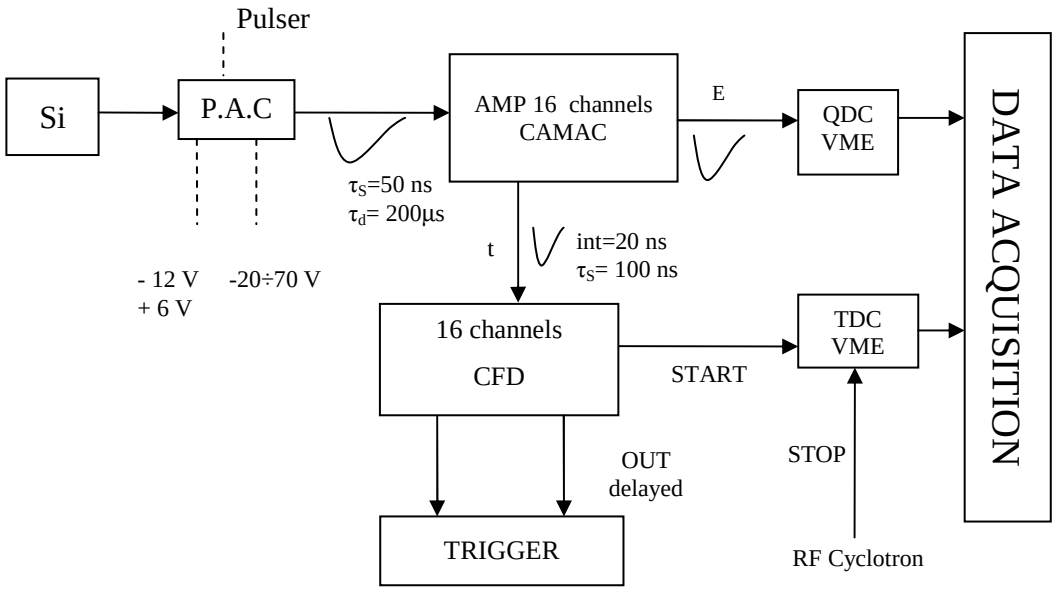

Figure 3.6 The electronic front-end of silicon detectors.

detector giving an output independent of the detector capacity and proportional to the charge produced by detected particles. Moreover, the preamplifier has a test input in which it is possible to send precise spanning pulses generator (pulser) signals, in order to control the electronic stability. Then the output signal is processed by the amplifiers (CAMAC 16 channels bipolar model, produced by CAEN). They give two different analogic outputs, one processes the signals for energy measurements, the other output for time measurements.

The energy signal is integrated by charge digital converters (QDC, realized on VME 9U standard by CAEN). In order to have a good energy resolution, also for low energy signals, the analogical to digital conversion is achieved by double charge encoding: the “High Gain” (HG) and the “Low Gain” (LG) coding.

Timing logical signals for the silicon are generated by a high resolution Constant Fraction Discriminator (CFD, produced by CAEN). This module gives two logic output, one prompt output is the start time reference signal. This signal together with the Radiofrequency of the Cyclotron are processed to the Time Digital Converter TDC and give the measure to the Time of Flight (TOF). The

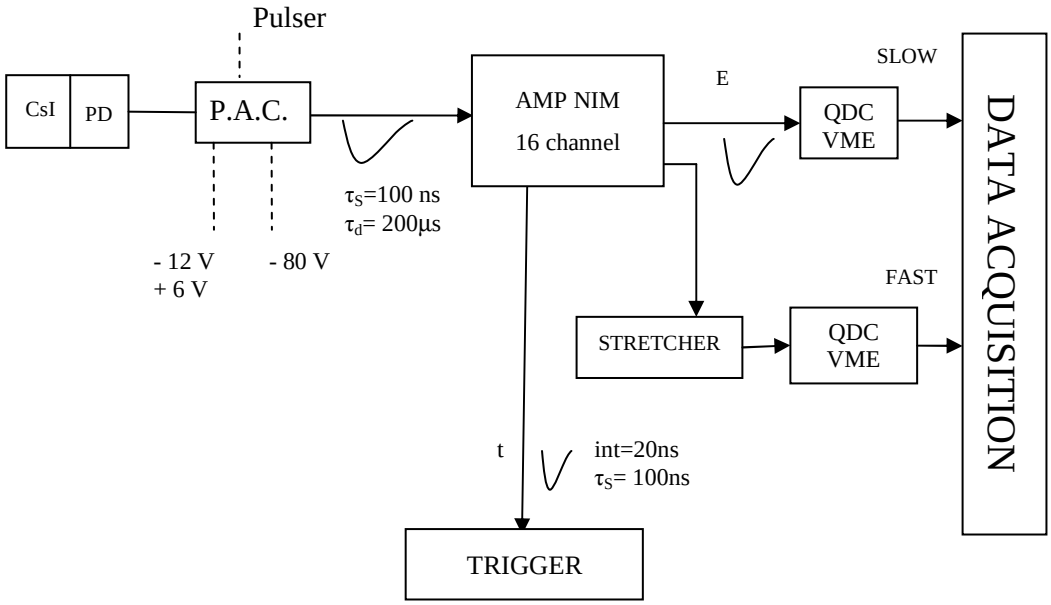

Figure 3.7 The electronic front-end of CsI scintillator.

CFD produces also a chainable multiplicity signal used for the trigger of the acquisition system. From the ring 4 to ring 16, the old silicon electronics has been replaced by new compact modules particularly studied for the measure of the rise time of the silicon signal enabling us to get the charge of particles stopped in the silicon detectors [ALD04, ALD05]. The module (mod. N1568 Caen) has 16 channels, each one including one energy and time amplifier, two CFD discriminators respectively with 30% and 80% fraction and a stretcher for the energy signal. The time difference between the 30% and 80% CFD provides the silicon rise time information. The stretched energy allows a simpler adjustment of the QDC gate. The production of these module has been planned to the Pulse Shape Discrimination in Silicon Detectors and described in the section 3.4.4.

A schematic view of the electronic chain of CsI(Tl) coupled with photodiode (PD) is shown in Figure 3.7. The amplifiers, produced by SILENA in a 16 channels NIM module, give a fast timing output and double output in energy for each channel, with different gains (higher = 10 · lower). The energy output with high gain is sent to the QDC, this is the “slow” CsI(Tl) signal component.

The other energy output is sent to a stretcher, it maintains the signal at its high value, this is the ”fast” component. The other delayed output of the TDC is used for the chain of trigger of the data acquisition system.

During experiments with beams produced by IFF, signals coming from MCP and DSSSD are added to the electronic chain. MCP signal is sent to a preamplifier. Then a constant fraction discriminator gives the time stop reference signal processed by the TDC. The 32 signals of the DSSSD are processed by two compact preamplifier produced by Mesytec and send to two 16 channel NIM modules. They give energy, time and OR outputs. The energy outputs of both strip sides are sent to the QDC to the measure of the energy loss. The timing outputs are sent to the TDC to the time reference. The OR of the front strip side, scaled by a factor from 100 to 500, is send to the trigger system to monitor the beam intensity.

The Trigger system of a 4π detector must be able to perform an accurate event-selection, while the event rejection must be fast enough to reduce dead time. In CHIMERA [ALD02] various triggers are used eventually scaled. They are based mainly on multiplicity that can be decided according to the physical purposes. During the experiments with radioactive beams, one event trigger multiplicity together with a beam monitor trigger has been set. The choice to use multiplicity M=1 is due to the rather low beam intensity and to store data from elastic scattering reactions. The beam monitor trigger, scaled by a factor 100-500, is generated by the DSSSD. When an event is accepted by the trigger the dead time signal is raised and gates to QDC and stretchers are generated. In order to select the good reference signals for the selected event, a window gate enabling the MCP and RF signals is generated. After the conversion time the CPUs begins the QDC and TDC data readout. When this job is ended a signal to stop the dead time is send and another event can be accepted.

Data are collected trough some racks PC. These are connected to the VME crate by an optical link with CAEN system V2718 VME-PCI Optical Link Bridge

and broadcasted via Ethernet to be read by different workstations for storage and on-line control. The set-up and control of CAMAC modules, including pulse generator linked to preamplifier for testing and calibration purposes, are realized via a set-up VME-6U CPU, while the NIM modules are controlled by a dedicated software running on a PC. More details can be found in Ref. [DEF07].

3.4 Identification methods

The CHIMERA multidetector allows the identification of the charge particles emitted from the reactions, by using four method: ΔE-E, TOF, PSD in Si, PSD in CsI(Tl).

3.4.1. ΔE-E technique

Particles punching through the Silicon detector and stopped in the CsI(Tl), can be identified by ΔE-E method. The identification is based on the energy correlation measured by the two detectors.

Charged particles pass completely through the Silicon detector, retaining most of its initial energy. Therefore the silicon detector and the CsI(Tl) measure respectively the energy loss (ΔE) and the energy residue (E). ΔE is given by the following equation:

$$\Delta E = \frac{dE}{dx}\Delta x \qquad 3.1$$

where Δx is the thickness of the silicon detector and dE/dx is the stopping power (differential energy loss for charged particles within the material divided by the corresponding differential path length). The –dE/dx, also called specific energy loss, is given by the Bethe-Block formula [LEO94]. By using this formula for charged particles detected by a telescope of two detectors, it finds that the energy residue and dE/dx are sensitive to the atomic number (A) and the charge (Z) of the particle. Then the two energies measured are related by the following relation:

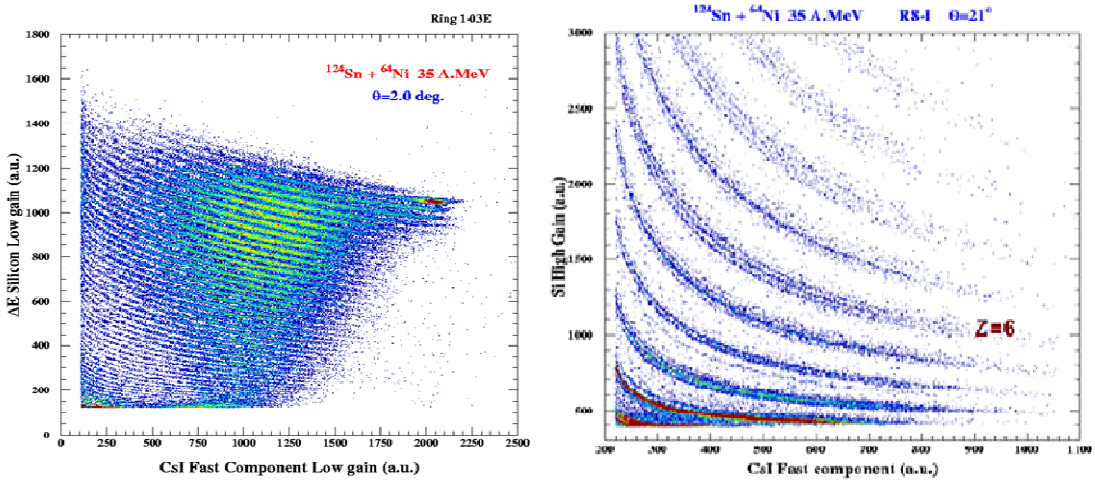

Figure 3.8 Reaction $^{124}Sn+^{64}Ni$ at 35 MeV/u. On the left side ΔE-E scatter plot, low gain configuration; it observers just charge identification. On the right side ΔE-E scatter plot, high gain configuration; it observes a very good isotopic identification [POL05].

$$E \cdot \Delta E \propto AZ^2 \qquad 3.2$$

The expression reveals that ΔE-E matrix (see Figure 3.8) have hyperbolic behaviour for each isotope detected, more sensible charge identification (due to Z^2 dependence) and mass identification for light particles. More details about the fitting procedure used can be found in [TAS01].

3.4.2. Time Of Flight

The particles stopped in the Silicon detector are identified in mass by the Time Of Flight (TOF) technique [PAG01, PAG04].

The start signal is given by 30 % Constant Fraction Discriminator acting on time signal generated by the silicon detector, while stop signal is given by delayed Reference Signal delivered by the Super Conducting Cyclotron (SC).

The identification in mass is obtained from the kinetic energy of the particle:

$$E = \frac{1}{2}Mv^2 = M\frac{D^2}{2\alpha^2}\frac{1}{(t_0 - t)^2} \qquad 3.3$$

where M e *v* are the mass and velocity of the particle detected; D is the base of flight from the target to the detector, α is a conversion factor between channel of the TDC and seconds (about 200 ps/ch); t is the time measurement; t_0 is the time

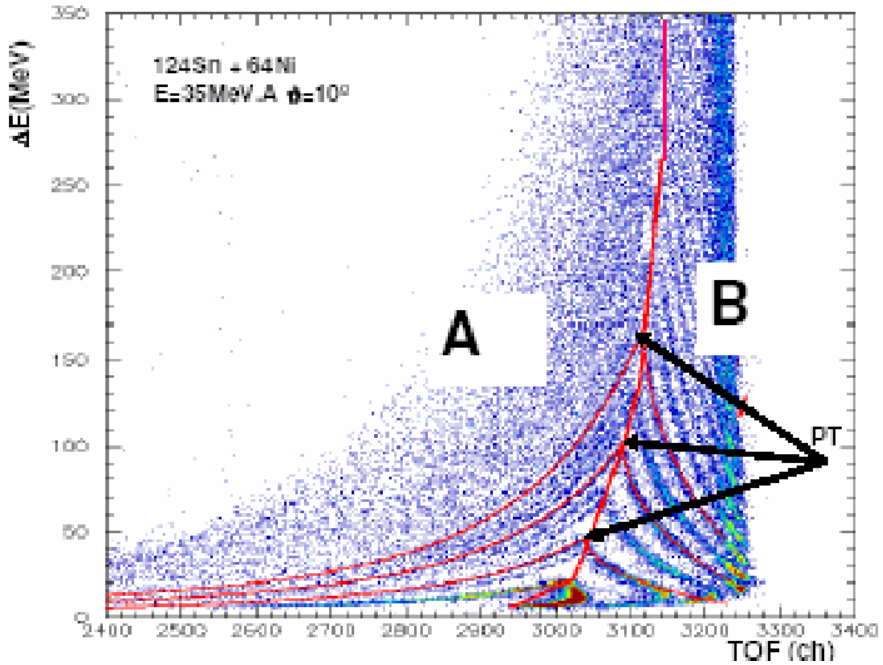

Figure 3.9 Reaction $^{124}Sn + ^{64}Ni$ at 35 MeV/u. TOF scatter plot. Time of flight against the energy measured by the silicon detector. A side shows particles stopped in the Silicon detector, B side particles punching through.

reference depending to the system configuration, it is set in a such way that $(t-t_0)$ is the "real" time of flight of the particle from the target to the detector. In order to obtain accurate measurement of the time of flight, it can be use calibration points of known energy.

This method allows to obtain also the velocity of the particle by using the follow expression:

$$v = \frac{s}{t} = \frac{D}{\alpha(t - t_0)} \qquad 3.4$$

The Figure 3.9 shows an example of TOF scatter plot. The figure shows also particle punching through the silicon detector. Considering also the Bethe block formula, it obtains $\Delta E \propto Z^2 (t - t_0)^2$.

3.4.3. Pulse Shape Discrimination in CsI(Tl)

CsI(Tl) scintillators are used to perform Light Charged Particles (LCP) mass and charge identification. They convert energy ionization to photons mainly in two different types of physical processes, resulting in two distinct light output components, commonly named ‘fast’ and ‘slow’, reflecting energy deposited by the particle in the crystal, and also the particle species. The light output of CsI(Tl) can be schematically described by a combination of two exponential components with different time constants. So pulse shape discrimination method (PSD)

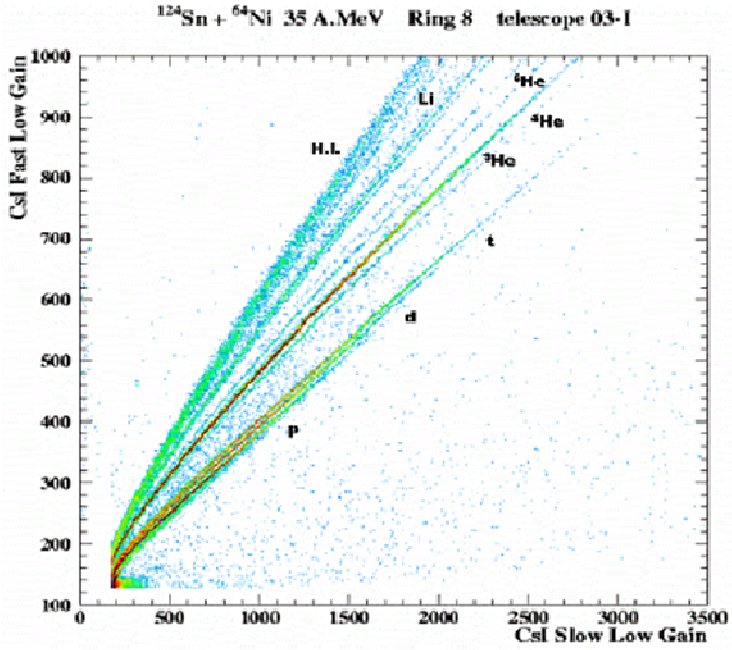

Figure 3.10 Reaction $^{124}Sn+^{64}Ni$ at 35 MeV/u. Scatter plot Fast-Slow [POL05].

consists in measurements of two gate applied on the signals shape output. One of the two energy outputs is stretched and then integrated (prompt component), the second energy output is directly integrated in the tail, providing information of the slow component of CsI light emission. The prompt and the slow components are thus used to construct an identification scatter plot, as shown in Figure 3.10.

3.4.4. Pulse Shape Discrimination in Si

In order to obtain charge (Z) discrimination for particles stopping in the first stage (Silicon detector), a new method PSD applied in Si has been developed, based on the Risetime measurements of charge signals by means of the difference in response time of two constant fraction discriminators, triggering at different pulse levels. The PSD method used is based on Risetime measurement of the signal for particles incoming in the front side mounted Silicon detector (300 μm thick). In fact the shape of the signal generated by a charged particle in a silicon detector carries information on its charge Z (see [MUT00] and references therein for further details).

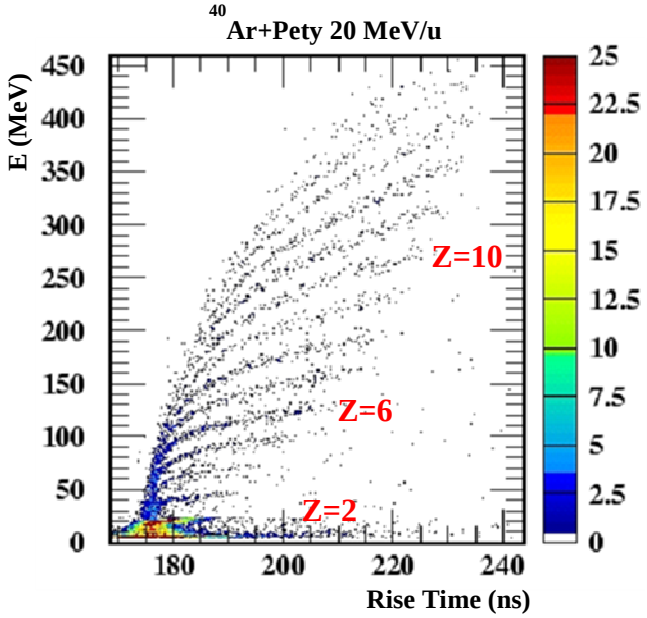

Figure 3.11 Reaction ^{58}Ni + ^{112}Sn at 35 MeV/u. Scatter plot energy against Risetime for fragments stopped in a silicon detector of ring 6 (θ = 13.7°).

A compact 16 channel NIM module commercialized by CAEN gives three signals. For each input: an analogical stretched signal proportional to the particle energy, a timing logic signal generated by a 30% constant fraction discriminator (CFD) and another timing logic signal generated at 80% fraction of the input signal. The risetime measurement is provided by the difference between the two timing signals (30% and 80% fractions). In Figure 3.11, the energy and risetime scatter plot reveals sensibility to the charge of the particle detected.

The pulse-shape analysis in silicon detector decreases the identification thresholds for charge and mass identification and allows the multidetector to be

used with low energy stable and exotic beams.

3.5 Kinematical coincidence technique

Because the CHIMERA multidetector is a 4π multidetector, the kinematical coincidence technique allows to exploit the good performance of the detectors. In this method energy spectrum is plotted considering events in coincidence with another telescope, kinematic condition "constraint" is that the azimuth angle between the two telescopes is 180° (Δφ=180°). Using such method it obtains background free data with good angular resolution. The main purpose is the measurement of angular distribution of fragments produced in two-body reactions such as elastic or inelastic scattering, transfer one etc.. As example, it can consider the results obtained studying the reaction ^{7}Li beam impinging on a plastic target, at 52 MeV. This experiment has been realized to check the quality of spectroscopic information that can be obtained by using CHIMERA multidetector. The Figure 3.12 shows the energy plot of two detectors with difference in azimuth angle of Δφ=180°. The black line corresponds to inclusive data. The red line corresponds to events in coincidence between the two detectors. The kinematic constraint produces very clean peaks and reduced background.

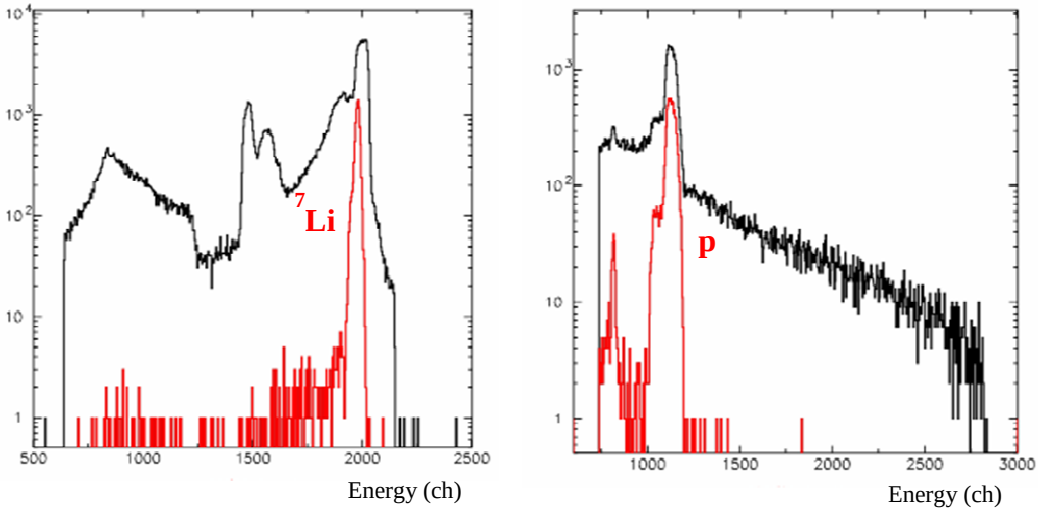

Figure 3.12. Reaction ^{7}Li+p at 52 MeV. Energy scatter plot of two silicon detectors with Δφ=180°. The black line corresponds to inclusive data. The red line corresponds event in coincidence.

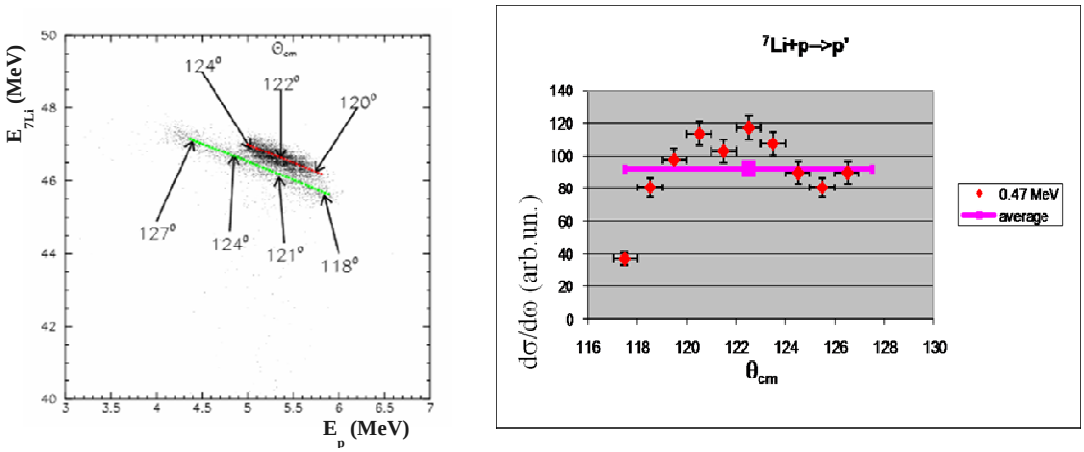

Figure 3.13 Reaction ^{7}Li+p at 52 MeV. On the left side, energy scatter plot ^{7}Li against proton energy of two silicon detector in coincidence with Δφ=180°. The kinematics lines relative to elastic scattering red line and inelastic scattering green line. On the right side angular distribution of the inelastic scattering to the first excited state of the ^{7}Li at 0,47 MeV [AMO08].

The CHIMERA sphere detectors (θ>30°) have an angular opening Δθ=± 4°, this value could produce a large energy spread in the coincidence peak in the extraction of angular distributions. Plotting the energies, relative at events in coincidence, it can distinguish kinematic lines corresponding to the different reaction channels involved. The Figure 3.13 shows two lines corresponding to the elastic and inelastic scattering to the first excite state of the ^{7}Li. In particular, the matrix is obtained plotting the energy measured in two silicon detectors of ring 3 external (θ=6.4°) and ring 13 (θ=58° sphere) in kinematical coincidence. It has been selected events stopped in the silicon detector. Besides considering small cuts in the inelastic line, as small as possible to have sufficient statistic, it corresponds a smaller angle in the centre of mass frame. This extrapolation can improve the angular distribution, as it shown in Figure 3.13.

CHAPTER 4 – Data Analysis

4.1 Introduction

During last year, two test experiments have been performed using CHIMERA multidetector and radioactive beams produced by the In Flight Fragmentation (IFF) method. The main aim is the study of direct reactions in inverse kinematic induced by these light ion beams at intermediate energy. In the chapter 2, the IFF facility running at LNS has been described in details. Through this production technique, different stable and exotic ion beams, are transported into the CHIMERA scattering chamber. A tagging system has been implemented in the CHIMERA multidetector, to perform isotopic identification of the incoming beams and measures their energies. Therefore, it allows to select accurately the different reaction channels and the incoming particles. Thanks to its higher rate than transfer reactions or other direct reactions, the elastic scattering is the first step to study the system, these radioactive nuclei and in the same time to explore CHIMERA capabilities (energy resolution, etc.).

In this chapter, it will be described the procedure to calibrate in time and energy the tagging system, the study of the beam line reconstruction, the kinematical coincidence method and the angular distribution of the elastic scattering for ^{13}B+d, ^{10}Be+p, ^{16}C+p and ^{16}C+d.

4.2 The tagging system calibration

As it has been described in the chapter 3, the tagging system consists of a MicroChannel Plate (MCP) and a Double Side Silicon Strip Detector (DSSSD). The DSSSD (149 μm thickness) is position sensitive, it is made of 16 strips front side and 16 strips back side in the opposite direction. To use MCP and DSSSD just when IFF beams are transported up the CHIMERA scattering chamber, they are set along the beam line with moving arms.

Initially, the system has been checked with a three peaks alpha source (5.1, 5.4 and 5.8 MeV). The MCP and DSSSD have been positioned in the vacuum tube at a distance of about 70 cm. An alpha source has been set in front of the MCP. The two output time references for the Time Of Flight (TOF) measurement are given by the MCP and DSSSD. The DSSSD measures also the energy (E) releases by the alpha particles. The Figure 4.1 (*a*) shows the matrix TOF–E, the three spots identify the alpha source structure, revealing the good performance of the tagging system. Indeed the DSSSD has enough energy resolution to resolve the substructures of the alpha source (~30 KeV energy resolution), and the selection of one pixel[3] in the DSSSD reveals time resolution better than 500 ps (see Figure 4.1 (*b*)).

After this check, two experiments with ^{13}C and ^{18}O primary beams at 55

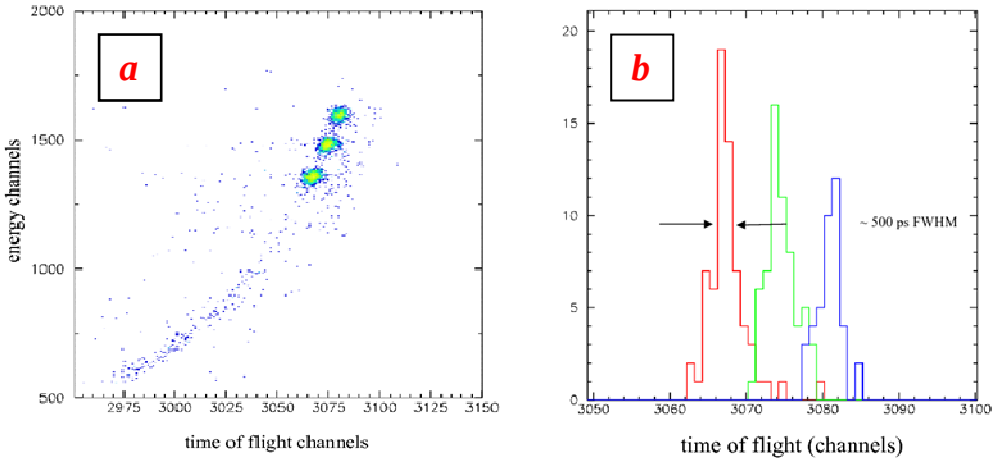

Figure 4.1 (*a*) TOF-energy scatter plot of alpha source. It has been selected one strip front side. (*b*) TOF histogram. The plot is obtained with one pixel[3] constraint in the DSSSD.

MeV/u have been performed by using CHIMERA multidetector. The task of the tagging system is to identify the incoming beams, and to measure their energies, to select the initial reaction channels, and to measure the number of the incoming particles. Therefore it must be used in transmission, and it would have to perturb the beams, as less as possible.

The time and energy scales have been calibrated by using the values

[3] A pixel in the DSSSD corresponds to one strip front side and one strip back side plot constraints.

predicted by LISE++ simulation program. The program is designed to predict the intensity and purity of radioactive ion beams by in-flight separators [TAR08]. It runs on various platforms and it has graphical interface. It has been selected the configuration of the fragment separator at LNS-INFN, called "LNS-ETNA_NoDegr", the primary beam, its energy and charge state (as example $^{13}C^{5+}$ at 55 MeV/u), the thickness of the production target (^{9}Be, 1.5 mm), the effective thickness of others "materials" crossed by the beams (the silicon detector is thick 149 µm; the mylar foil of the MCP is thick 2 µm and it is set at 45° respect the line beam), the "drift", which is the base of flight between the material chosen (MCP is set at 12.9 meter distance by the DSSSD). In particular the calibration of the tagging system has been performed considering the magnetic rigidities of the Fragment Separator, "Dipole 1" and "Dipole 2", on the maximum optimum transport of the chosen isotope (^{12}B, Bρ=2.433 Tm). This configuration setting simulates the TOF-ΔE scatter plot of the tagging system (see Figure 4.2 (*a*)). For each beams, energy and TOF values are established to scale channels in the tagging system.

For each strip front side, graphical contour cuts are done on the different beam spots (^{13}B, ^{12}B, ^{11}B, ^{10}Be, ^{9}Be, ^{8}Li, ^{7}Li and ^{6}Li, recognized from the comparison with LISE++ simulation, see Figure 4.2 (*a*)). The linear best fit establishes the time (expressed in nsec) and energy (expressed in MeV) scale of the tagging system. When the tagging system is calibrated for each strip front side of the DSSSD, the TOF-ΔE scatter plot can be plotted considering all events coming from the different strips (see Figure 4.2 (*b*)).

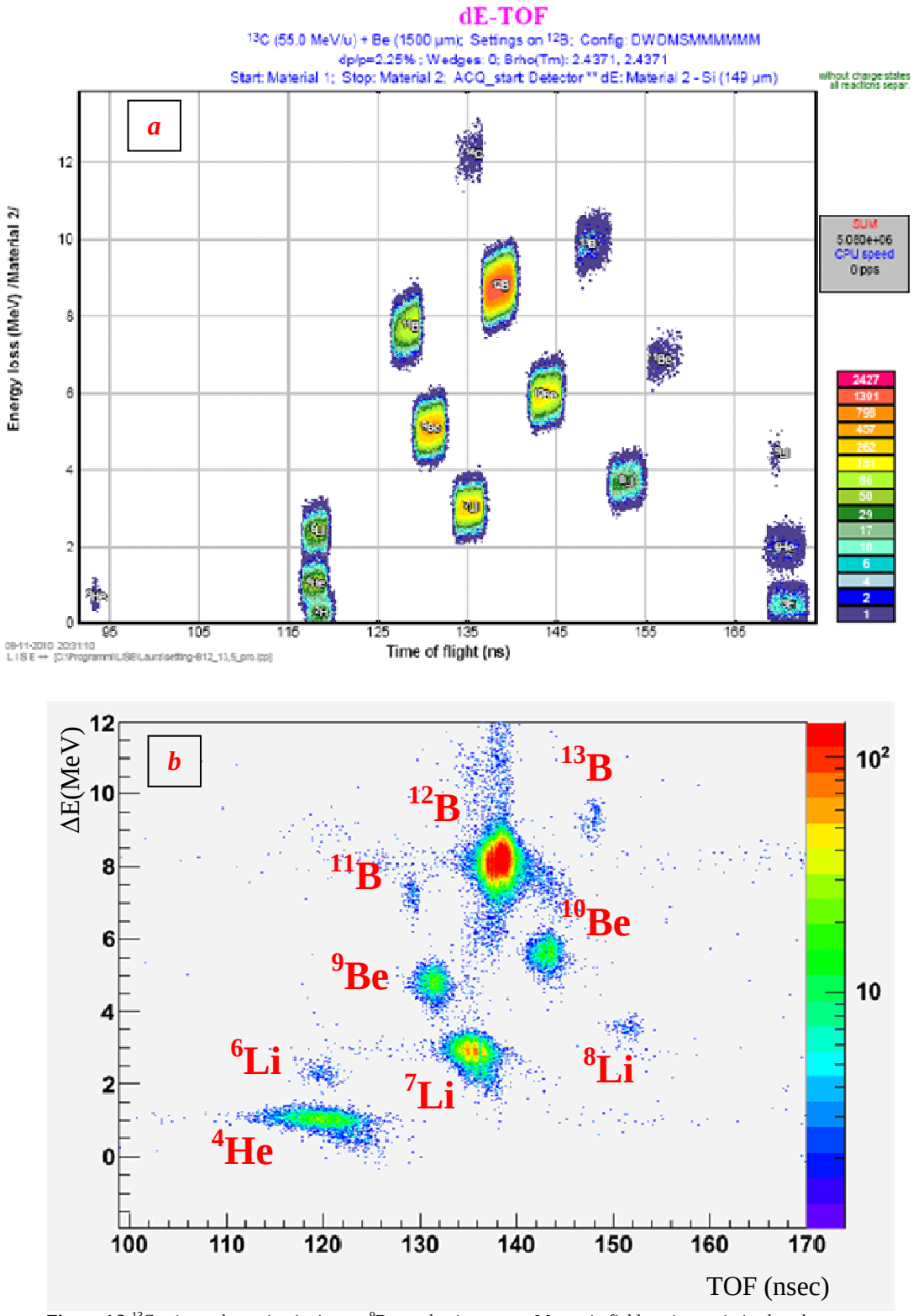

Figure 4.2 ^{13}C primary beam impinging on ^{9}Be production target. Magnetic field setting optimized to the transport ^{12}B. (*a*) TOF - ΔE LISE++ code simulation. (*b*) Experimental data TOF - ΔE scatter plot.

A check of the reliability of the calibration stands out comparing the values predicted by LISE++ program relative to another setting of magnetic fields. For example, setting the LISE++ configuration on $^{13}C^{5+}$ primary beam at 55 MeV and magnetic rigidity optimized on the transport of ^{11}Be fragment, the simulated TOF-ΔE scatter plot is obtained (see Figure 4.3 (*a*)). The general agreement with the corresponding experimental TOF-ΔE matrix (Figure 4.3 (*b*)) is quite good. However some discrepancies can be evaluated calculating the energies of the beams relative to the calibrated system by the following expression:

$$E_{beam} = \frac{md^2}{2t^2} - \Delta E \qquad 4.1$$

where m is the mass of the isotope, d is the base of flight, t is the time of flight of the tagging system and ΔE is the energy loss in the DSSSD. Comparing the extracted values with ones calculated by LISE++ simulation, and including the energy beams calibrated produced by $^{18}O^{7+}$ primary beam at 55 MeV/u (see Figure 4.4 (*a*) and Figure 4.4 (*b*)), an overall uncertainty of the beam energy is estimated $\pm$2.5%.

There are different kinds of uncertainties to lead forward this result. The main uncertainties are: the production target thickness ($\pm$1% about), the uniformity and thickness[4] of silicon detector ($\pm$1% about) and the energy of the primary beam ($\pm$1% about). The last uncertainty leads to strong effects in the final energy measurements, because it is strictly related with the setting of the magnet fields. As it has been described in the chapter 2, the pilot beams technique set the magnetic rigidity (Bρ) of the beam line transport. The primary beam, characterized by a given Bρ, is employed itself as pilot beams. This value is comparable with the Bρ predicted by LISE++ to optimize the transport on the isotope previously considered.

[4] The hole-electron pair collection depends on the depletion thickness, which is, more or less, the thickness of the detector.

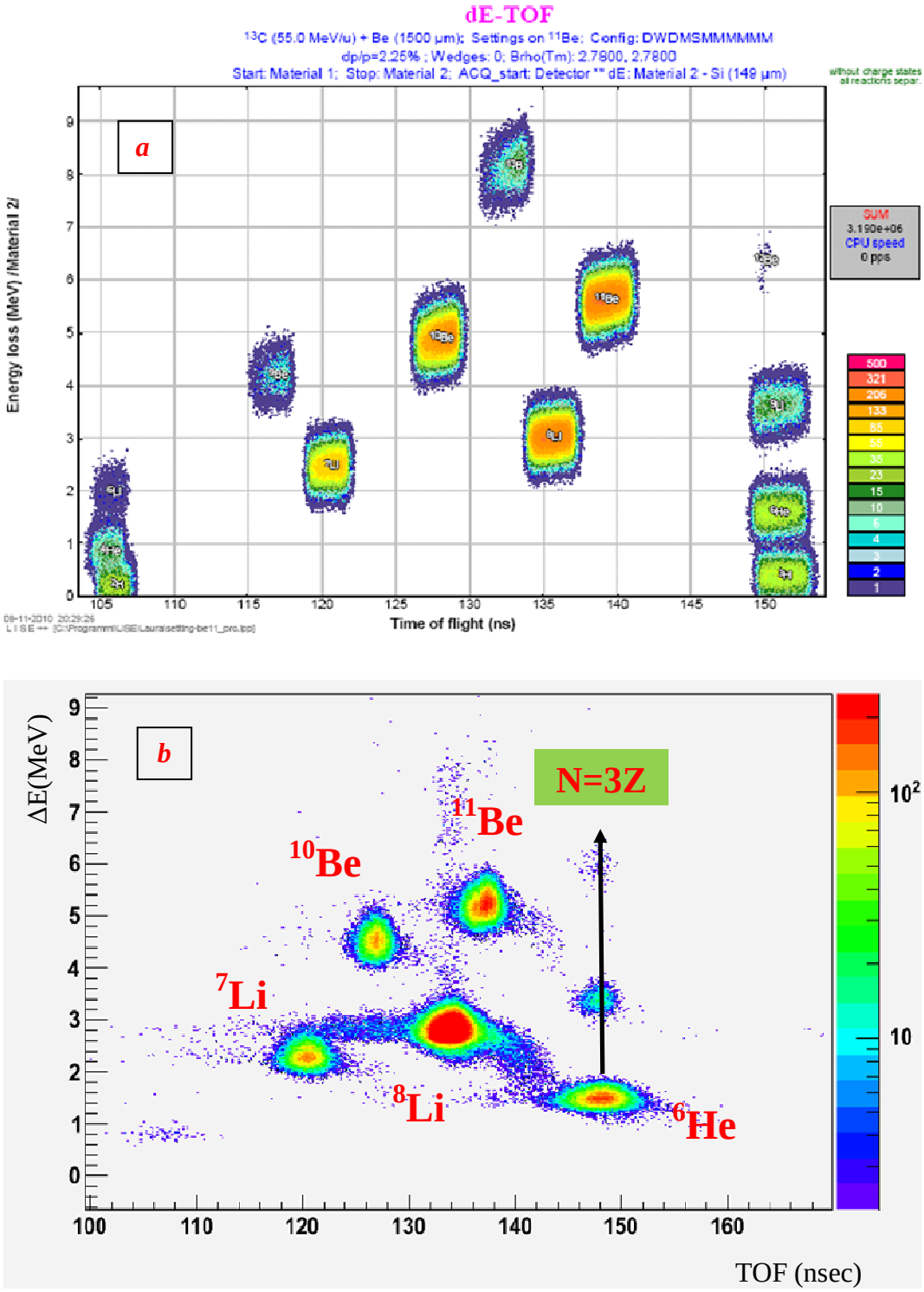

Figure 4.3 ^{13}C primary beam impinging on ^{9}Be production target. Magnetic field setting optimized to the transport ^{11}Be. (*a*) TOF - ΔE LISE++ code simulation. (*b*) Experimental data TOF - ΔE scatter plot.

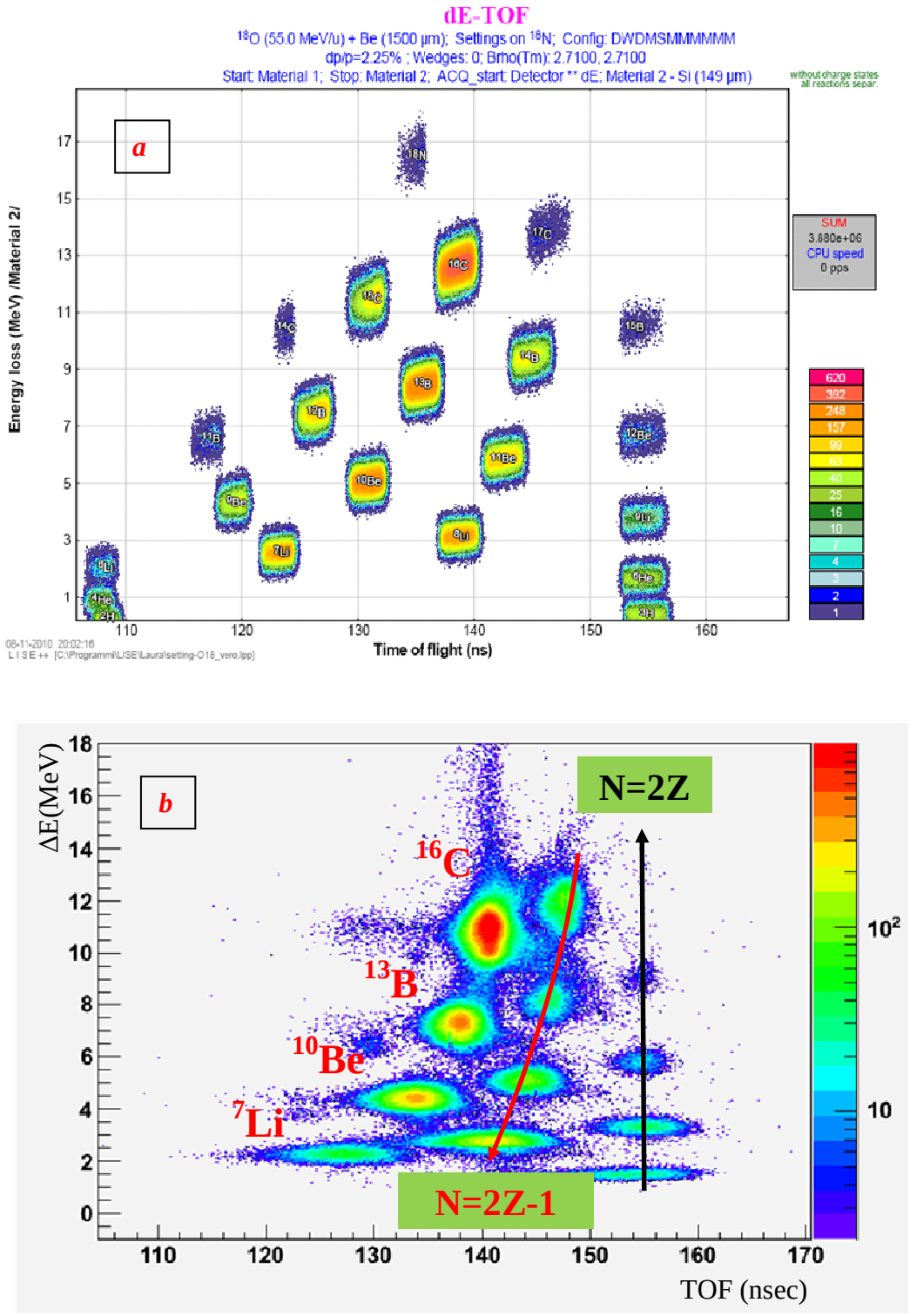

Figure 4.4 ^{18}O primary beam impinging on ^{9}Be production target. Magnetic field setting optimized to the transport ^{11}Be. (*a*) TOF - ΔE LISE++ code simulation. (*b*) Experimental data TOF - ΔE scatter plot.

The combination of all these uncertainties reasonably explains the final spreading observed between predicted and measured beam energies. Recent improvement about magnetic fields measurements and diagnostic system along the beam line will lead to energies uncertainties smaller than the $\pm$2.5%.

Apart the uncertainties above reported, the effect of the energy spread must also be taking into account. The production mechanisms generate beams with a rather large energy spread, moreover the beam line transport is optimized to select beams with about $\pm$1% momentum spread. This momentum spread, related also to the dispersion effect of the last dipole before the scattering chamber, can be highlighted by the TOF measurement, strip by strip of the DSSSD. The Figure 4.5 (*a*) and (*b*) show the TOF measured for ^{12}B ions in different pixels of the DSSSD. The Figure 4.5 (*a*) is obtained by selecting one strip front side (strip n. 5) and spanning all the strips in the back side. Instead the Figure 4.5 (*b*) is obtained by

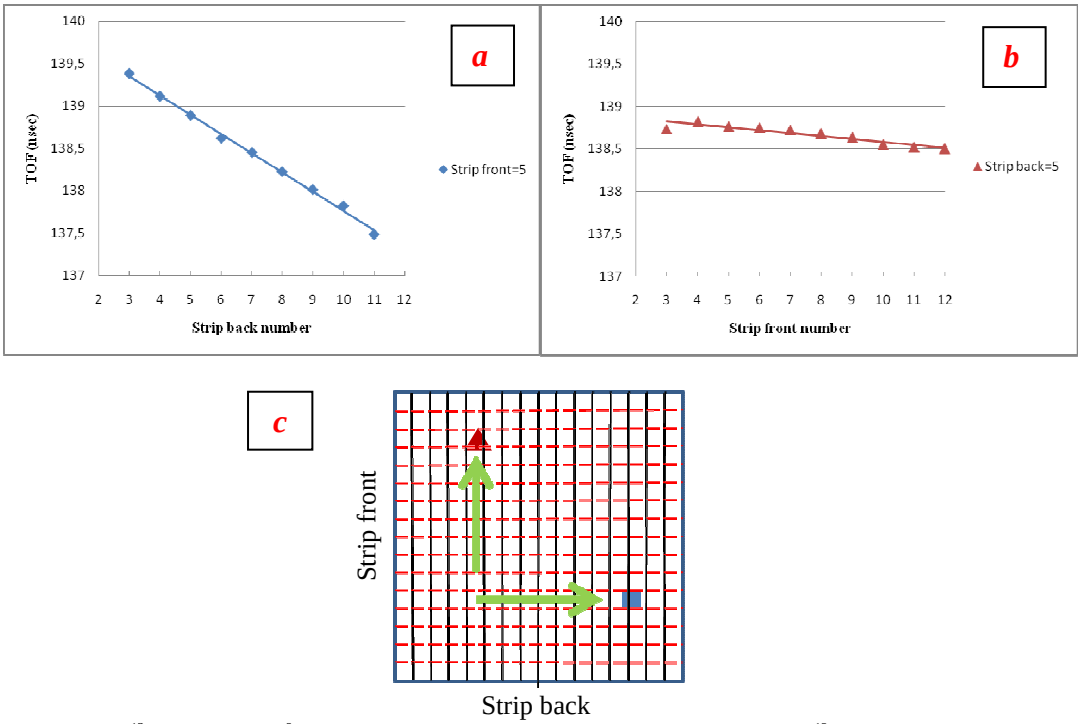

Figure 4.5 ^{13}C impinging on ^{9}Be production target, magnetic fields optimized to transport ^{12}B. (*a*) TOF measured by each back strips side and strip front side=5. (*b*) TOF measured by each front strips side and strip back side=5. (*c*) Schematic view of the DSSSD. The triangle and the square show the pixel direction of the two pictures in *a* and *b*. The dashed lines correspond to the back strip side.

selecting one strip back side (strip n. 5) and spanning all the strips in the front side. As schematized in the Figure 4.5 (*c*), the Figure 4.5 (*a*) and (*b*) match respectively to horizontal and vertical coordinate of the DSSSD. The Figure 4.5 (*a*) immediately underlines that an average TOF variation of about 2 ns of the beam paths exists when the horizontal plane is investigated (Figure 4.5 (*c*)). This effect is principally dues to the energy dispersion of the last dipole. The beam with larger average TOF has less energy and is more bended by the dipole than the beam with smaller TOF (higher energy).

Detailed analysis to discriminate interstrip events, i.e. events when particles punch through the middle space between two strips (Figure 4.6 (*a*)), from coincidences events, i.e. an event with two beam particles impinging on different strips (Figure 4.6 (*b*)), has been done. To avoid troubles, these events are excluded from the analysis data, considering, as it will be explained below, that they are a small percentage of the total ones. However the understanding of the effects,

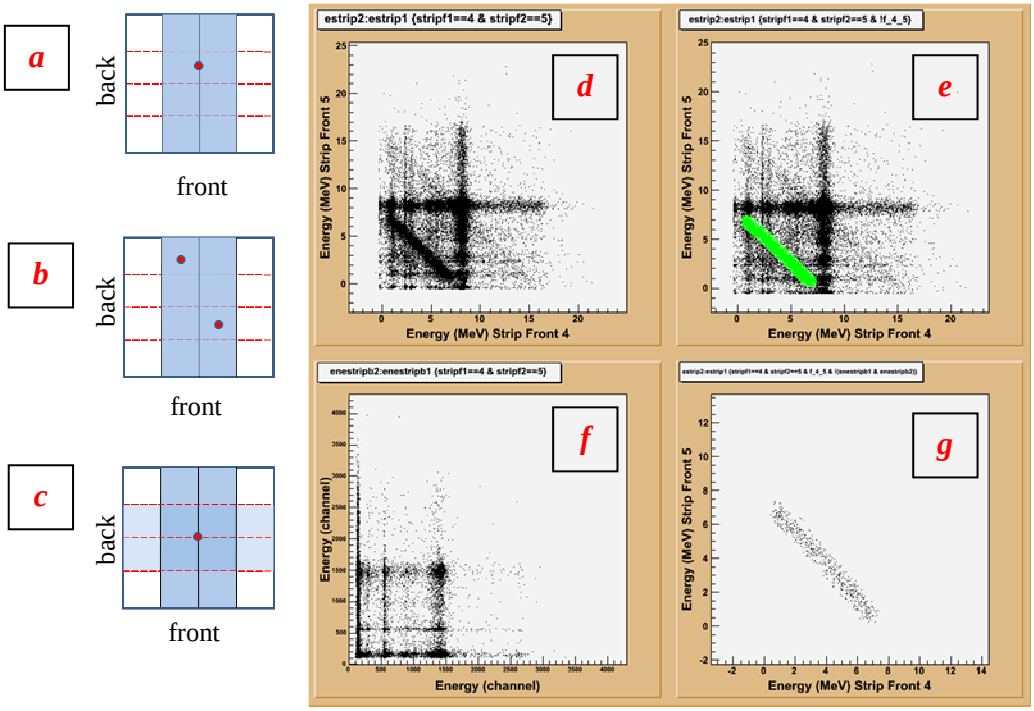

Figure 4.6 Schematic views: (*a*) interstrip event, (*b*) typical coincidence (*c*) interstrip event in a pixel. (*d*) Energy scatter plot of two adjacent strips front side. (*e*) Graphical cut on ^{12}B events with diagonal behaviour. (*f*) Energy plot correlation back side when two adjacent strips of the front side are fired. (*g*) Energy scatter plot of the graphical cut shows in the panel (*d*) less the events displayed in (*f*).

coming from these double and/or multiple firing events, helps to be ready to the future developments.

Interstrip events consist in a charge collection divided by two adjacent strips, therefore the sum of the energy measured by the two strips is the real energy loss by the particle in the detector. The Figure 4.6 (*d*) shows the plot of two adjacent strips front side. The diagonal behaviour is recognized as interstrip events, instead the lines parallel to the axes are events in which two particles have impinged the two strips, when the ACQ time window gate of QDC is opened (see section 3.3 in the chapter 3). The Figure 4.6 (*e*) reports a graphical contour cut (green colour) on the diagonal behaviour of the ^{12}B isotope. Obviously, in this cut also coincidence events are included (due to the intersection of the lines parallel to the axes). Therefore, another condition is required to discriminate interstrip events from coincidence ones. In general, the coincidences should fire two different strips of the back side (Figure 4.6 (*b*)), the probability that a particle impinges in the middle space of a pixel would be low (Figure 4.6 (*c*)). Indeed the energy correlation between two strips back side shows no diagonal behaviour (Figure 4.6 (*f*)), when two adjacent strips front side are fired. Therefore, assuming that interstrip events have double strips front side fired and single one from the back side (Figure 4.6 (*g*)), it is found that interstrip events are a very small part of the coincidences, which in turn, about 11% of the total events.

4.3 Kinematical coincidences technique

In the chapter 3, the kinematical coincidence technique has been showed in an experiment with stable beam at low energy. In that case the coincidence was looked for particle stopped in the silicon detectors. The following results are the first ones obtained at intermediate energy (55 MeV/u primary beam), looking for particles in coincidence between CsI(Tl) scintillators.

The study of events in coincidence between two telescopes is based on the

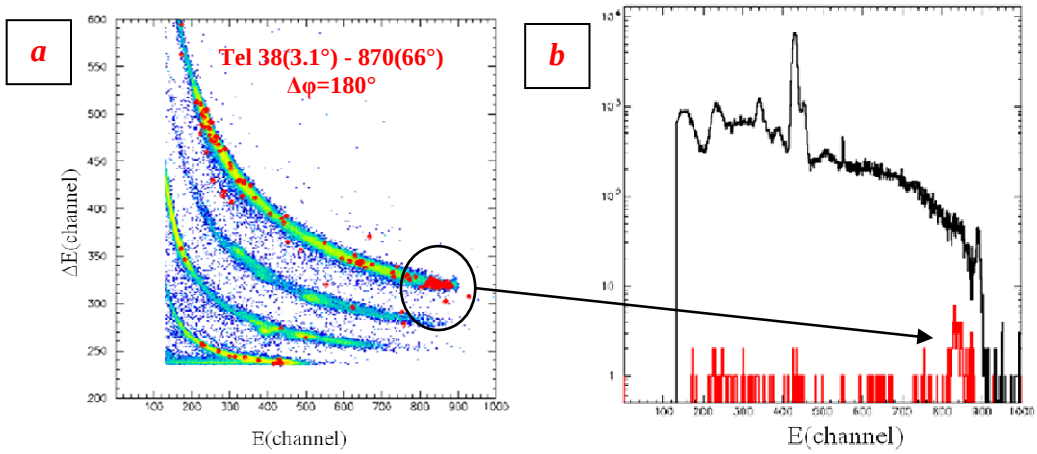

Figure 4.7 (*a*) ΔE-E matrix inclusive data cocktail beam. Selecting ^{12}B beam, the red points are relative to the particles detected in the telescope at 3.1° in coincidence with those ones detected by the telescope at 66°. The azimuth angle between the two coupled telescopes is Δφ=180°. (*b*) Energy histogram measured by the scintillator. The peak pointed to the arrow corresponds to the elastic scattering ^{12}B+d reaction.

comparison of the kinematic expected for the direct reaction involved (elastic or inelastic scattering, transfer reaction, etc.). Even if it requires a careful procedure to check coincidences, this technique gives spectra very clean from the data background. The Figure 4.7 (*a*) represents ΔE-E scatter plot of all the particles detected at polar angle θ_1=3.1°. Selecting from the cocktail beam the ^{12}B particles, the coincidence, between the telescope at θ_1=3.1° and the one at θ_1=66° with azimuth angle Δφ=180°, produces the red points in Figure 4.7 (*a*). As expected by 2-body kinematic, the elastic peak is recognized, see also energy spectrum in Figure 4.7 (*b*). Changing just the azimuth angle to Δφ=215°, no one coincidence, coming from elastic scattering reaction, is prominent (see Figure 4.8), because the detectors coupled don't satisfied the kinematic rules.

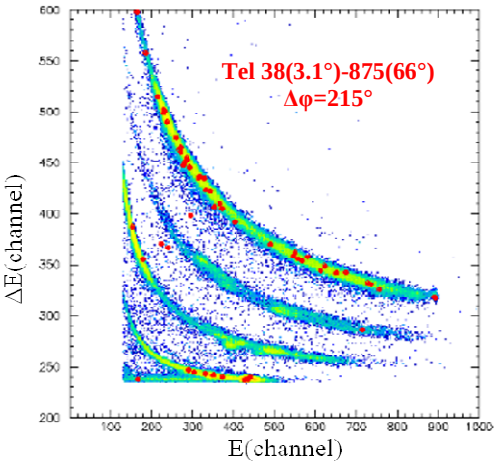

Figure 4.8 Selecting ^{12}B beam, the red points correspond to the particles detected in the telescope at 3.1° in coincidence with the telescope at 66°. The missing elastic events is due to Δφ=215°.

4.4 Angular distribution of the elastic scattering

The aim of this analysis is to extract from the experimental data the angular distribution of the heavy partner of the reaction in the centre of mass reference frame (CM). The angular cross section in the centre of mass frame is given by

$$\frac{d\sigma}{d\Omega} = \frac{N_{scat}}{N_i t \Delta\Omega} J_{CM} \qquad 4.2$$

where N_{scat} is the number of the particles scattered measured, N_i is the number of the incoming particles, t is the thickness of the target (atoms/area), $\Delta\Omega$ is the solid angle, J_{CM} is the factor to the transformation from the laboratory frame to the Centre of Mass frame.

The first task is the measure of the number N_{scat} of reaction events at a given angle. For each telescope of the forward rings, this is the sum of events in coincidence detected by scintillators kinematically coupled. In the experiment with ^{18}O primary beam, during the observation of these detectors, it has been realized that the beams line axis is not straight. This modifies the kinematical coupling between detectors. Indeed the particles, punching through the extreme right side of the DSSSD, are detected by the telescopes of the first ring of the CHIMERA array in the opposite direction (left side). The same result has been obtained in the others spatial directions. Taking into account that there aren't detectors at angles less than

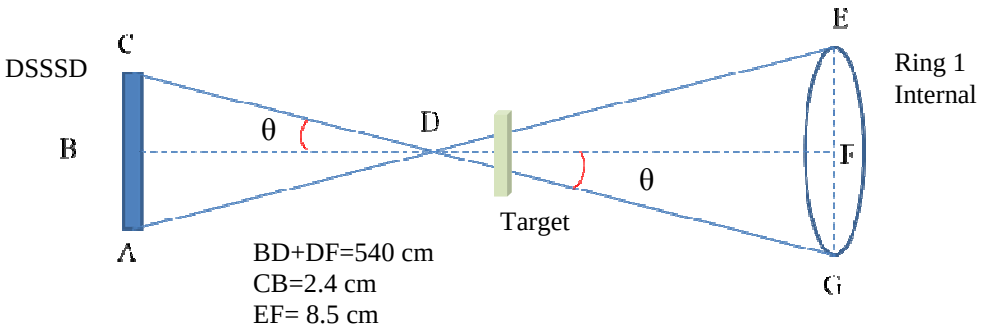

Figure 4.9 Schematic view of the focus beams point.

1° degree, it has been done some assumptions, strip by strip, to correct the beam line reconstruction.

The Figure 4.9 shows a schematic view of the system configuration. The angular corrections are obtained from the following relation:

$$tg\theta = \frac{EF}{DF} = \frac{CB}{BD} \qquad 4.3$$

where BD+ DF=540 cm is the distance between the DSSSD and the first ring, EF is its radius, and CB is the half length of the silicon detector side. The corrections on the angles respect to the centre of the DSSSD are the following:

	Strip 1/16	Strip 2/15	Strip 3/14	Strip 4/13	Strip 5/12	Strip 6/11	Strip 7/10	Strip 8/9
Δθ	1.16	1.02	0.87	0.73	0.58	0.44	0.29	0.10

Once taken into account these corrections, it can search for kinematical coincidences. It has to consider the spread in angle (in θ and φ) of the telescopes, and the correction due to the impinging angle of the beam.

The scattering angles predicted by the kinematic don't suit perfectly to the detectors opening. As an example, in Figure 4.10 are plotted two ^{16}C energy spectra, measured by two CsI(Tl) scintillators (one detector of the ring 2 external

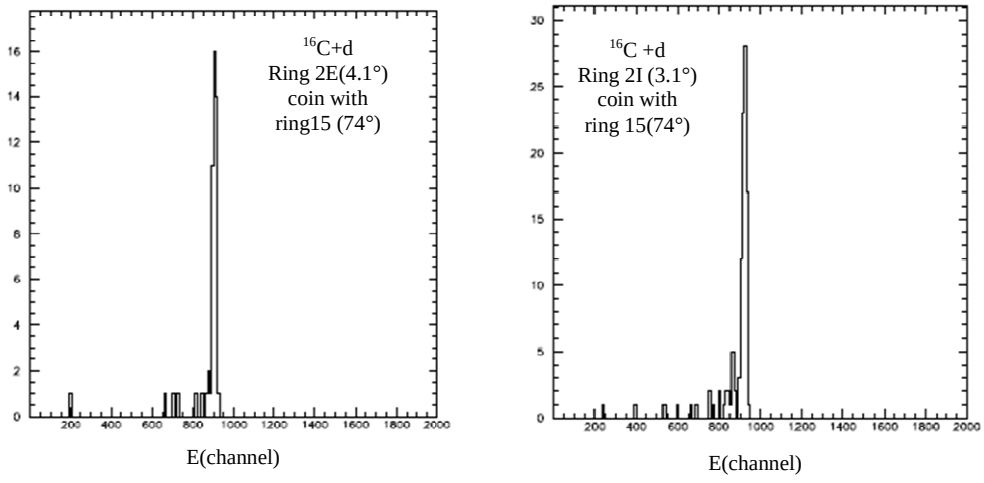

Figure 4.10 ^{16}C+p elastic scattering at 50 MeV/u. Energy scatter plots between two kinematically coupled scintillators with Δφ=180°.

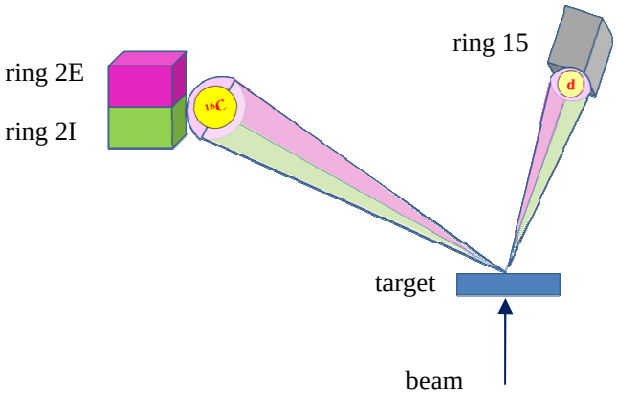

Figure 4.11 Schematic view of a typical coincidence between two telescopes along the polar angle.

and one of the ring 2 internal). The events are in coincidences with deuterons detected by a telescope of the ring 15. The kinematic angles expected, for elastic scattering of ^{16}C and deuterons, fall in the space between two detectors. The effective polar angle θ and the solid angle of the measured cross section is the result of the matching between the kinematic rules and the opening of each the detector (see Figure 4.11).

Similar situation can be switch along the azimuth angle (see Figure 4.12 (*a*)). In Figure 4.12 (*b*) is represented the energy histogram of ^{12}B detected by a scintillator of the ring 1 external (2.2°) in coincidence with deuterons detected by two scintillators of the ring16 (θ=82°).

In conclusion the solid angle and the θ polar angle of the particles detected are the results of the matching between the kinematics of the reaction, and the

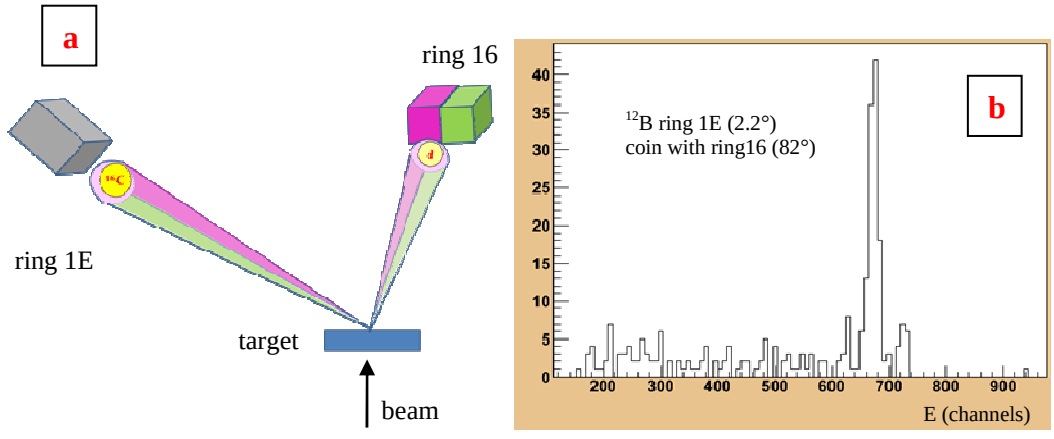

Figure 4.12 (*a*) Schematic view of a typical coincidence between a telescope of the ring 1 external and two telescopes of the ring 16. (*b*) ^{12}B+d elastic scattering at 47 MeV/u. Energy scatter plots between the scintillators kinematically coupled.

opening of the scintillators involved.

After these careful evaluation of the particles scattered at the effective angle θ in the laboratory frame, the transformation in the centre of mass frame θ_{CM} results multiplying for the Jacobian factor.

In the equation 4.2, the number of impinging ions, N_i, is given by the particles counted by the trigger of the tagging system. The selection of the beam incoming with the data beam trigger provides the number of event. The correction factor (see chapter 3, section 2.4) used in the acquisition beams events is considered. However even here, some cautions must be taken. During the experiment with ^{13}C primary beam impinging on ^{9}Be production target, even if the beam profile was not spread on the whole DSSSD (see Figure 4.13), many particles are scattered by the target frame. This makes difficult a correct evaluation of the incoming particles. For this reason, the angular distributions obtained correspond just at the test experiment with ^{18}O primary beam impinging on ^{9}Be production target. In the next experiment, a MicroChannel Plate position sensitive

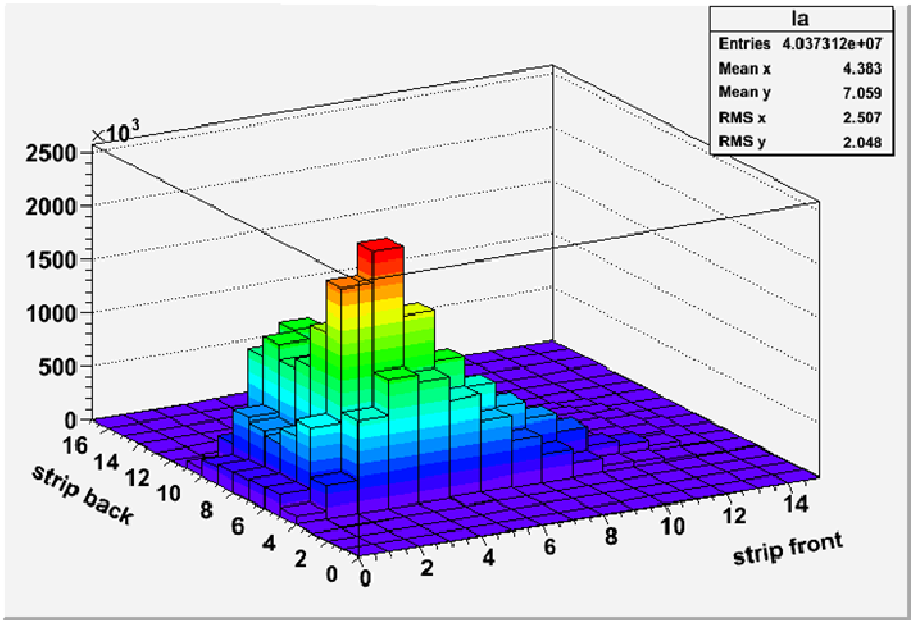

Figure 4.13 ^{13}C primary beam impinging on ^{9}Be production target, magnetic fields optimize to the transport of the ^{12}B. Matrix of the beam 2D-profile seen by the DSSSD.

will set in front of the reaction target.

The measured angular distributions are reported in table and plotted in Figure 4.14.

Table 4.1 Elastic scattering angular distributions for different initial channel reactions.

	θ_{CM}(degrees)	σ_{CM}(mb/sr)	$\Delta\sigma_{CM}$(mb/sr)	σ_{CM}/σ_R	$\Delta\sigma_{CM}/\Delta\sigma_R$
^{16}C+p 50 MeV/u	19.2	184.39	26.61	6.71	0.97
	26.8	75.16	8.40	10.34	1.16
	34.4	55.81	15.48	20.59	5.71
	46.0	15.79	2.19	17.71	2.46
	61.6	8.87	1.46	29.26	4.81
	77.4	2.20	0.90	16.09	6.57
^{16}C+d 50 MeV/u	18.2	126.16	4.08	13.6	0.44
	25.0	60.00	2.03	9.74	1.3
	20.7	54.55	7.29	22.3	0.75
	28.8	50.69	5.04	33.1	3.3
	38.5	11.88	2.17	34.7	2.87
	33.3	30.36	2.51	23.9	4.36
^{13}B+d 52 MeV/u	16.3	88.06	3.45	9.16	0.36
	23.1	70.47	6.72	20.2	2.34
	21.1	69.59	8.09	28.8	2.74
	26.0	44.03	4.83	28.6	3.14
	32.7	24.89	2.09	40.1	3.36
	38.5	35.19	11.13	106.6	33.7
^{10}Be+p 56 MeV/u	19.1	94.95	7.70	94.95	7.70
	26.0	82.92	6.75	82.92	6.75
	33.2	57.43	3.91	57.43	3.91
	40.4	18.85	2.24	18.85	2.24
	48.1	6.76	0.67	6.76	0.67
	63.2	3.57	0.37	3.57	0.37

where θ_{CM} is the scattering angle in the centre of mass frame of the ^{16}C+p, ^{16}C+d, ^{13}B+d and ^{10}Be+p, σ_{CM} is the correspondent cross section given by the equation 4.2, $\Delta\sigma_{CM}$ is the error given by the Poisson statistic equal to $\sigma_{CM} / \sqrt{N_{scat}}$. The σ_R and $\Delta\sigma_R$ are the Rutherford cross section and its errors.

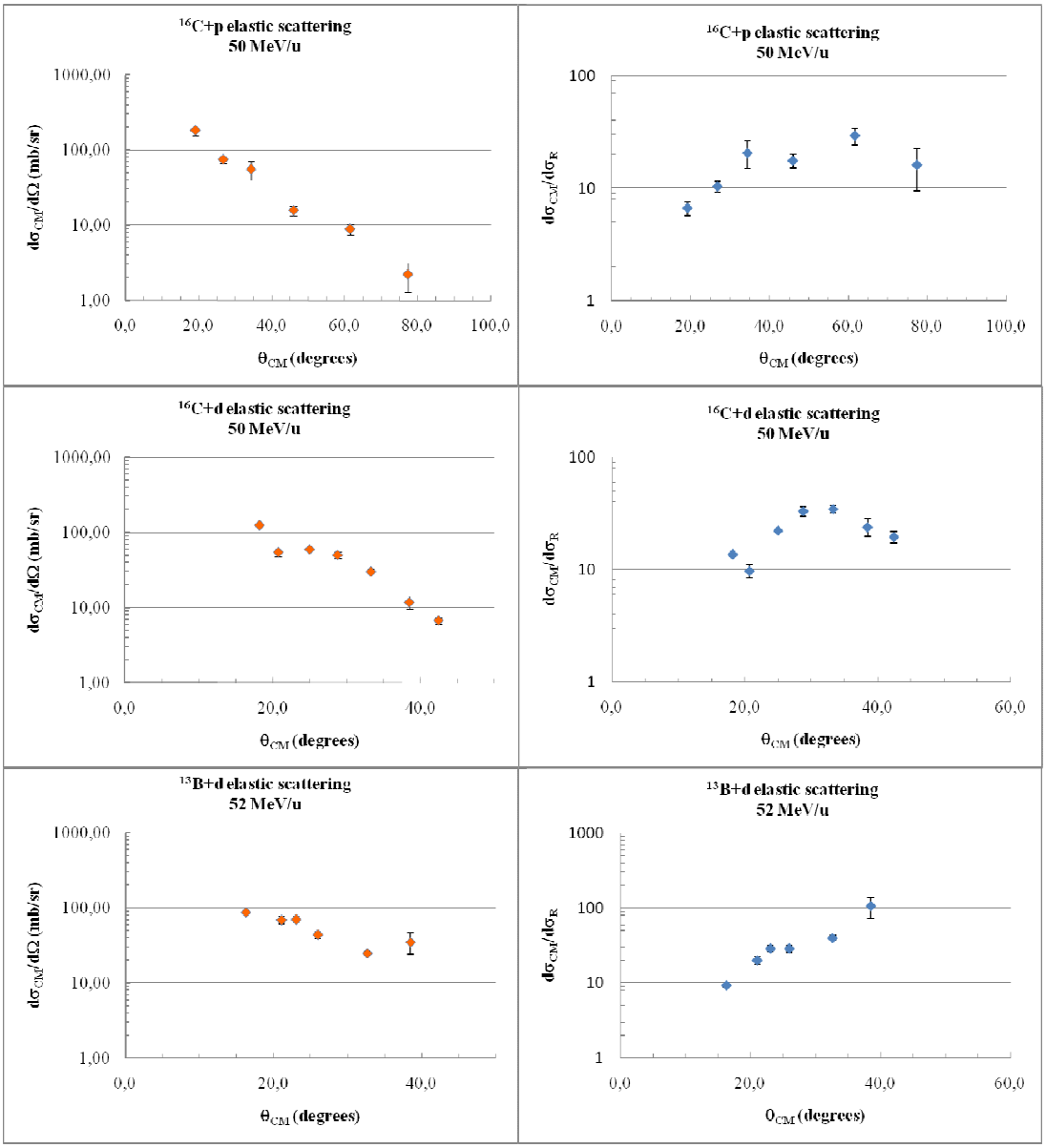

Figure 4.14 Elastic scattering angular distribution for colliding systems. On the left side the cross section measured. On the right side the ratio to the Rutherford cross section.

CHAPTER 5 – Elastic scattering measurements

5.1 The Optical Model

In this chapter the procedure and the potential shapes used to fit the elastic scattering angular distributions of the systems ^{16}C+p, ^{16}C+d, ^{13}B+d and ^{10}Be+p, are described. Elastic scattering is an ideal tool to study some nuclear properties (as nucleon-nucleon interactions, radial structure, etc.). In particular the proton and deuteron elastic scattering on light elements is conditioned by nuclear rather than electrostatic interaction. Indeed while elastic scattering cross section between heavy nuclei follows the $1/E^2$ energy dependence, light system particles, at intermediate range energies, are characterized by cross sections respect to the Rutherford ones, which rapidly increase with the scattering angles [GUR03]. The Coulomb effects are important only at small angles then the nuclear scattering dominates, this effect is related with the nuclear force short range. The common model used to describe the elastic scattering in literature is the optical model which describes the effect of the target nucleus on the incident particle in terms of a complex potential well. The optical analogy is a semi-transparent sphere scattering and absorbing light (cloudy crystal ball model) [WIL97]. The basic assumption is that the interaction between two colliding nuclei (structure-less), depends by the distance r between the centres of the two nuclei. The imaginary part of the potential takes into account all the effects different from the elastic scattering channels, involved in the reactions.

The elastic scattering angular distribution measured, shown in the chapter 4 (Table 4.1), has been analyzed using PTOLEMY code [RHO80], which provides an efficient program for fitting optical model potentials to elastic scattering data and calculate the cross sections. The potential shape used is:

$$V(r) = V_c(r) - Vf_1(r) - iW(r) f_2(r) + (V_{LS} + \tau \cdot V)\frac{4}{r}\mathbf{L}\cdot\mathbf{S}\frac{df_{LS}(r)}{dr} \qquad 5.1$$

where V_c is the Coulomb potential; V, W and V_{LS} are the potential depths of the real, imaginary and spin-orbit terms which depend by the energy involved in the elastic scattering; the functions $f_1(r)$, $f_2(r)$, $f_{LS}(r)$ are usually taken to have the familiar Saxon-Woods forms:

$$f(r) = \frac{1}{1 + e^{\frac{r-R}{a}}} \qquad 5.2$$

where $R = R_0 A_P^{1/3}$ is given by the projectile for elastic scattering system; *r* is the radial distant from the centre; *a* is the diffuseness, it describes the potential fall-off at the surface. In literature [PER76], usually the R_0 and *a* are about 1.20 fm, and 0.7 fm respectively. The spin-orbit potential part, referring to the spin of the projectile coupled to its orbital angular momentum, is included when the spin is different to zero [PTO78].

5.1.1. ^{16}C+p and ^{16}C+d elastic scattering at 50 MeV/u

The ^{16}C is a nucleus studied in some works [ELE04, ZHE02]. Its structure is not yet well understood from both theoretical and experimental point of view. It could be a candidate 2n-halo nucleus, but it is closer to the stability line than other 2n-halo nuclei. Even if ^{16}C can also be treated as a core+n+n three-body system, it is not a Borromean system because the subsystems n-^{15}C are bound. The ^{16}C one-neutron (S_n) separation energy is 4.250 MeV, and the two-neutron (S_{2n}) separation energy is 5.468 MeV. This suggests that pairing effect of the two neutrons added, in the system ^{14}C+2n, plays a very important role in ^{16}C. On the other hand, lifetime measurement for the first-excited state in ^{16}C [WIE08] and transfer reaction ^{15}C(d,p)^{16}C requires no exotic interpretation [WUO10]. Therefore complementary study of the elastic scattering could investigate its anomalous

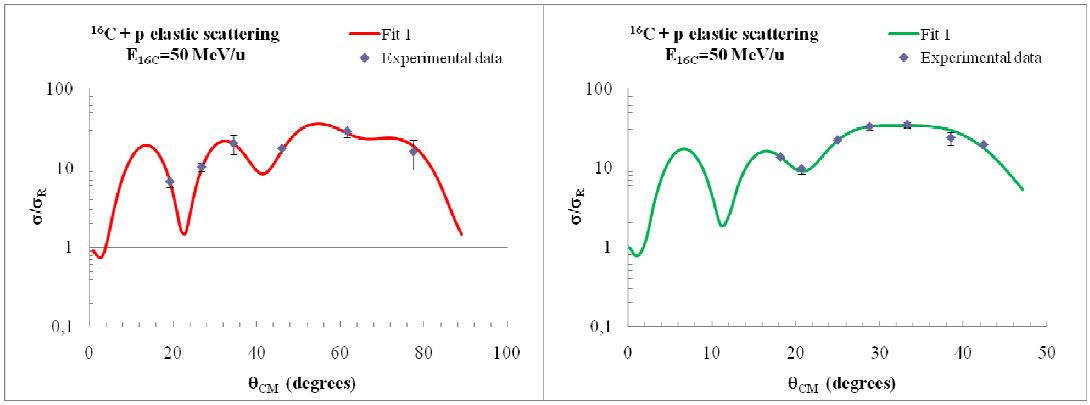

Figure 5.1 ^{16}C+p, ^{16}C+d elastic scattering. Fits to the experimental data by using optical potential model.

behaviour.

To avoid a fit with too many free parameters, that can produce "unphysical" results, initially the radius and diffuseness (real and imaginary parts) has been fixed and the potential depths are set as "free" fit parameters. ^{16}C has spin zero in the ground state, so the last term of the potential expression in 5.1 is equal to zero. The initial values to the fit are chosen looking for similar system in literature or in the Ref. [PER76]. As example, the radius real and imaginary of the interaction is set equal to 1.2 fm, and the diffuseness a and a_i, from the initial value of 0.7 fm, are scaled (one by one) at step of 0.02 fm. This task ends when the best chi-square per point (χ^2/point) is obtained. Results are reported in Table 5.1, and the angular cross sections to the Rutherford calculated by using the potential fit parameters, are plotted with experimental data in Figure 5.1.

Table 5.1 Optical model potential fit parameters

	V(MeV)	R_0(fm)	a(fm)	W(MeV)	R_{0i}(fm)	a_i(fm)	R_{c0}(fm)	χ^2/point
^{16}C+p 50 MeV/u	270	1.20	0.85	45.9	1.20	1.20	1.26	0.2
^{16}C+d 50 MeV/u	246	1.17	0.90	28.6	1.20	1.70	1.26	0.4

As expected, both the systems have behaviour close to the Rutherford at very small angles, then the nuclear force is more predominant than the Coulomb

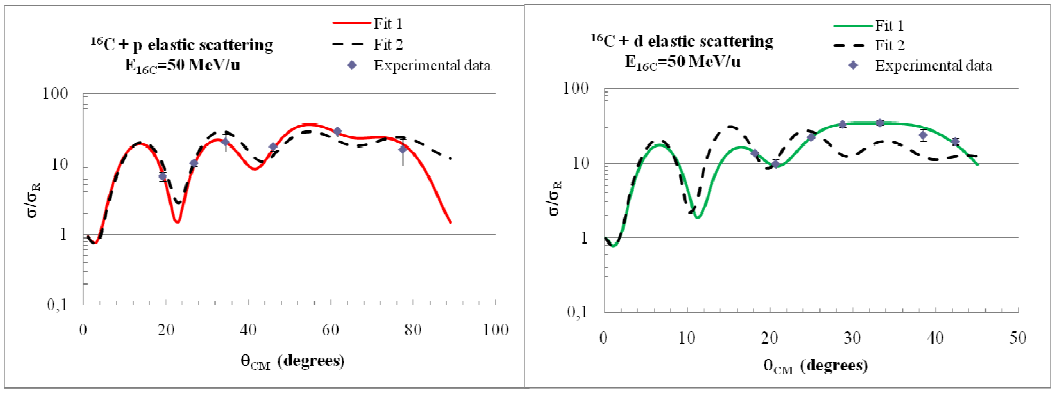

Figure 5.2 Elastic scattering angular distributions ^{16}C+p (left side) and ^{16}C+d (right side). The two lines (continue and dashed) are two fits to the data relative to the parameters reported in Table 5.2.

one and the ratio increases. The oscillations are typical to Fraunhofer nearside/farside interference pattern (diffraction effect).

The imaginary diffuseness parameters obtained from the fits have "anomalous" values, in particular for the elastic scattering of ^{16}C on deuteron target. Even if the usually halo nuclei are characterized by a potential surface [BON02], the big diffuseness of the imaginary part could suggest some strange behaviour. Different attempts have been done to fit the experimental data with a surface potential. Being few experimental data points, the addiction of more fit parameter produces unphysical results. In order to highlight the reliability the fit analysis, the comparison between two different data fits is plotted in Figure 5.2. The "anomalous" set parameters are named Fit 1, instead Fit 2 is the fit of the data by using "normal" diffuseness and radius parameters and the "free" potential depth. The two parameters sets are summarizes in Table 5.2. "Normal" diffuseness and radius fixed in the calculations produce a strong imaginary potential depth, and in the ^{16}C+d also an "enormous" real one. Elastic scattering reaction can't produce so high absorption, therefore the solution Fit 2 seems to be "unphysical". Moreover in Figure 5.2 the dashed black line (Fit 2) don't suite the data behaviours, especially in the elastic scattering ^{16}C+d, where the higher value of diffuseness is obtained. The pictures confirm the goodness of the parameters Fit

1 to reproduce the data behaviour.

Table 5.2 For each system, two sets potential parameters are reported.

		V(MeV)	R_0(fm)	a(fm)	W(MeV)	R_{0i}(fm)	a_i(fm)	R_{c0}(fm)
^{16}C+p 50 MeV/u	Fit 1	270	1.20	0.85	45.9	1.20	1.20	1.26
	Fit 2	286	1.20	0.85	88.7	1.20	0.90	1.26
^{16}C+d 50 MeV/u	Fit 1	246	1.17	0.90	28.6	1.20	1.70	1.26
	Fit 2	647	1.17	0.90	420	1.20	0.90	1.26

5.1.2. ^{13}B+d and ^{10}Be+p elastic scattering at 52 MeV/u

^{13}B and ^{10}Be isotopes have not "halo" structures, however the study of elastic scattering reactions for these nuclei is an important tool to future investigations of the ^{14}B and ^{11}Be "halo" nuclei. As it has been shown in the Chapter 1, one neutron halo is described using two-body model (nucleus core+neutron), therefore proton or deuteron elastic scattering calculations give important information to the core nucleus wave function to be used in the description of other direct reactions (transfer, break-up, etc.).

With the same method previously described, the ^{13}B+d and ^{10}Be+p elastic scattering angular distribution has been reproduced.

^{13}B has spin equal to $J^{\pi}=3/2^{-}$, so initially V, W, V_{LS} are taken as "free" parameters and the corresponding diffuseness and radius are fixed. This potential shape, using different combination of fixed initial parameters, doesn't give any

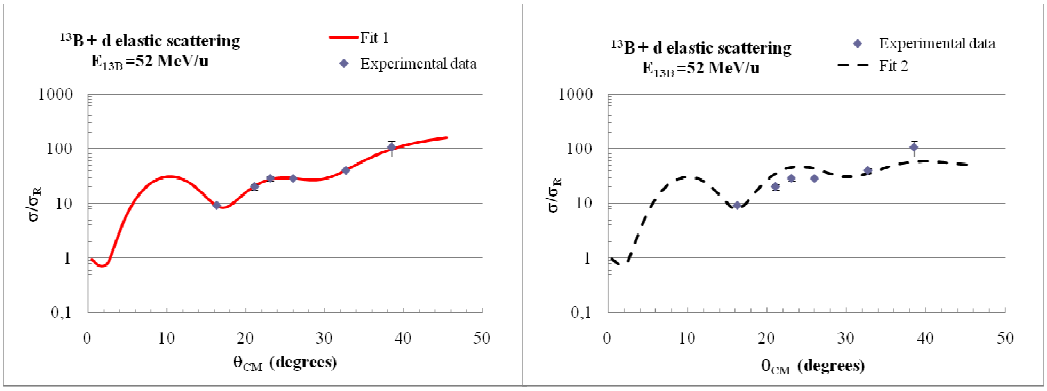

Figure 5.3 ^{13}B+ d elastic scattering, the pictures show two data fits by using parameters summarized in Table 5.3.

reasonable results. PTOLEMY code calculates no one possible result. Probably, due to the few data points, the introduction of further three parameters (connected with spin-orbit term) decreases the reliability to the data fits. To this reasons, assuming V_{SO} contribution smaller than the real and imaginary depth, spin-orbit term are neglected. The values of parameters obtained are reported in Table 5.3, named "Fit 1". The parameters of the imaginary potential are characterized by a little high diffuseness and radius. Different values (suggested by literatures for similar system [PER76]), produce an imaginary depth too high, compared with the real one (see Fit 2 in Table 5.3), and make worse the fit quality (χ^2=21.0 and see Figure 5.3).

Table 5.3 Two sets of fitted parameters to experimental data.

		V(MeV)	R_0(fm)	a(fm)	W(MeV)	R_{0i}(fm)	a_i(fm)	R_{c0}(fm)	χ^2/point
^{13}B+d 52 MeV/u	Fit 1	219	0.82	0.75	23.5	1.10	0.99	1.25	0.05
	Fit 2	143	1.13	0.70	65.4	1.13	0.70	1.25	21.0

Also for the ^{10}Be+p elastic scattering angular distribution, the data fitting procedure begins by the initial parameters of diffuseness and radius, for the real and imaginary part of the potential, suggested by [PER76]. This set of values lead to a real potential repulsive (Table 5.4 - Fit 2), which is "unphysical" solution for

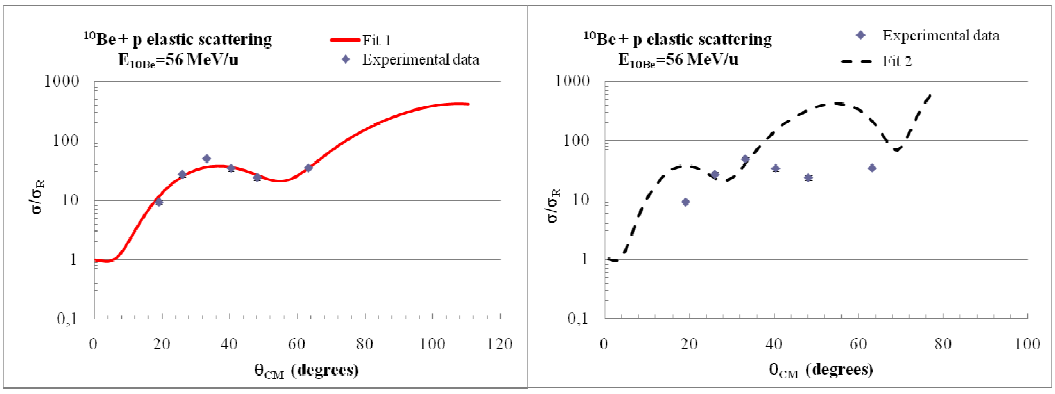

Figure 5.4 ^{10}Be+p elastic scattering. The pictures show two data fits by using parameters summarized in Table 5.3.

the nuclear attractive force. Scaling at steps radius and diffuseness real and imaginary parameters, the best reproduction to the data behaviour is suited by the parameters corresponding to the Fit 1 in Table 5.4. Beside, even if the radii and diffuseness are smaller than the parameters summarized in the Fit 2, the potential depths are more confident to those calculated for other elastic system at similar energies, above reported. The Figure 5.4 shows the two angular distributions fitted to the data (Fit 1 and Fit 2) and the better reproduction of the data behaviour by the red line than the black dashed one.

Table 5.4 Two sets of fitted parameters to experimental data.

		V(MeV)	R_0(fm)	*a*(fm)	W(MeV)	R_{0i}(fm)	a_i(fm)	R_{c0}(fm)	χ^2/point
^{10}Be+p 56 MeV/u	Fit 1	278	0.57	0.31	16.8	0.9	0.40	1.25	4.5
	Fit 2	-12.6	1.20	0.60	0.04	1.20	0.60	1.25	47

SUMMURY AND CONCLUSION

The present work reports first results about production of radioactive beams and the investigation of the CHIMERA multidetector capabilities using kinematical coincidences. At Laboratori Nazionali del Sud of the Istituto Nazionale di Fisica Nucleare (LNS-INFN) in Catania (Italy), radioactive ion beams (RIBs) are produced by In Flight Fragmentation (IFF) technique. Two experiments, with ^{18}O and ^{13}C primary beams at 55 MeV/u impinging on ^{9}Be production target, have produced light RIBs with enough rate (10^3 - 10^4 p/s) to study elastic scattering of ^{16}C+p and ^{16}C+d at 50 MeV/u, ^{10}Be+p at 56 MeV/u and ^{13}B+d at 52 MeV/u.

The experiment set-up has required some upgrading and accurate analyses. A tagging system, consisted of a Double Side Silicon Strip Detector (DSSSD) and a MicroChannel Plate (MCP), has been implemented on the CHIMERA multidetector. Measuring the energy loss (ΔE) in the DSSSD and the Time of Flight (TOF) between the two detectors, the energies measurement of the beams incoming and their isotopic identification have been performed the energies of the beams incoming and their isotopic identification have been performed. The system calibration has been obtained using the ΔE and TOF predicted by LISE++ simulation code. The program is designed to predict the intensity and purity of radioactive ion beams by in-flight separators. Setting the configuration of the Fragment Separator (FRS) at LNS-INFN and the experimental conditions (primary beams, detectors, etc.), the ΔE-TOF scatter plot is accurately predicted. Checks to the reliability of the calibration have highlighted some energy uncertainties due to the productions mechanisms and to the unknown magnetic fields in the dipoles. Future upgrading about monitor beam transport system and magnetic rigidity measurements in the FRS will lead to smaller uncertainties.

The elastic scattering angular distribution is measured by using kinematical coincidence technique. Taking into account that CHIMERA is a 4π multidetector, measurements of events in coincidence between telescopes coupled kinematically allowed to obtain high quality data. The energy spectra are cleaned by the background and the reaction mechanism involved is uniquely recognized. On the other hand some troubles arise when the beams incoming have not straights line and they are not focus on the target. The lack of a beam tracking has revealed some difficulty in the beam line reconstruction. Analysing events detected in the forward part of the CHIMERA array and punching through the DSSSD, strip by strip, some assumptions have allowed carrying on the data analysis. Next improvements about a MicroChannel Plate position sensitive, positioned in front to the target, together with a DSSSD will permit easier and more accurate beams lines reconstruction.

Selecting the initial reaction channel, measuring the number of particles incoming and the events in kinematical coincidences, with the appropriate solid angle, the elastic scattering angular distributions are obtained for the following systems: ^{16}C+p and ^{16}C+d at 50 MeV/u, ^{10}Be+p at 56 MeV/u and ^{13}B+d at 52 MeV/u. The experimental are fitted by using optical model. As expected, due to the short range of the nuclear force, the Coulombian forces are sensible only at very small angles. Increasing the angles the nuclear force becomes predominant leading at high values of the cross section to the Rutherford one.

In particular, the fits of the experimental data seem to reveal an anomalous structure of the ^{16}C isotope. Nowadays, its structure is not well understood, even if ^{16}C can also be treated as a core+n+n three-body system, it is not a Borromean system because the subsystems n-^{15}C are bound, the paring effect of the two neutron added at ^{14}C seems to play an important role [WUO10,WIE08, ELE04, ZHE02]. The elastic scattering distribution, fitted for the reaction channels ^{16}C+d and ^{16}C+p, leads at “anomalous” diffuseness of the imaginary potential. These

results could confirm the anomalous structure of the ^{16}C. Besides the upgrading of the FRS (available next year), about new larger quadrupoles and sextupoles mounting, will increase the beam intensity per 10 factor, carrying on further data analysis of direct reactions, as transfer and break up and more detail studies of elastic scattering. These studies will be complementary in the investigation of ^{16}C structure and other nuclei as ^{11}Be halo.

BIBLIOGRAFY

[AGO09] C. Agodi et al., LNS Activity Report, 24 (2009)

[AIE95] S. Aiello et al., Nucl. Phys. A 583, 461c (1995)

[ALA04] N. Alamanos, A. Gillibert, *Selected Topics in Reactions studies with exotic nuclei*, Lect. Notes Phys. 651, 295-337 (2004)

[ALD02] M. Alderighi et al., IEEE Trans. Nucl. Sci., 49, 334- 338 (2002)

[ALD04] M.Alderighi et al., Nucl. Phys. A 734, E88-E91 (2004)

[ALD05] M. Alderinghi et al., IEEE Trans Nucl. Sci. 52, 1624 (2006)

[AMO08] F. Amorini et. al., LNS Activity Report, 103 (2008)

[ARN92] E. Arnold et al., Phys. Lett. B281, 16 (1992)

[ATMC] Atomic Mass Data Center http://www-csnsm.in2p3.fr/AMDC

[BER83] A.M. Bernstein et al., Comm. Nucl. Phys. 11, 203

[BOL97] G. Bollen, Nucl. Phys. A 616, 457c (1997)

[BON85] A. Bonaccorso, G. Piccolo, D.M. Brink, Nucl. Phys. A 441, 555 (1985)

[BON88] A. Bonaccorso, D.M. Brink, Phys. Rev. C 38, 1776 (1988)

[BON91a] A. Bonaccorso, D.M. Brink, Phys. Rev. C 43, 299 (1991)

[BON91b] A. Bonaccorso, D.M. Brink, Phys. Rev. C 44, 1559 (1991)

[BON92] A. Bonaccorso, D.M. Brink, Phys. Rev. C 46, 700 (1992)

[BON98] A. Bonaccorso, D.M. Brink, Phys. Rev. C 58, 2864 (1998)

[BON02] A. Bonaccorso, F. Carstoiu, Nucl. Phys A 706 (2002) 322

[BON03] A. Bonaccorso Acta Physica Hungarica A) Heavy Ion Physics Vol.18, Number 2-4, 193, (2003)

[BOU02] C. Boutin, Climbing out of the nuclear valley, Cern Courier (2002)

[BOW73] J.D. Bowman, W.J. Swiatecki, and C.F. Tsang, Lawrence Berkeley Laboratory Report, LBL-2908, (1973), unpublished.

[BRA97] M.E. Brandan, G.R. Satchler, Phys. Rep. 285, 143 (1997)

[BRO81a] R.A. Broglia, A. Winther, Heavy Ion Reactions, Benjamin, Reading, MA, 1981.

[BRO81b] R.A. Broglia, G. Pollarolo, A. Winther, Nucl. Phys. A 361, 307 (1981)

[BRO89] H.L. Ravn and B.W. Allardyce, "On-Line Mass Separators". In Treatise on Heavy-Ion Science, Vol. 8 ed. by D. Allan Bromley (Plenum Publishing Corporation, 1989) p 363–439

[BRO96] B.A. Brown, in: M. de Saint-Simon, O. Sorlin (Eds.), Proc. Int. Conf. Exotic Nuclei and Atomic Masses (ENAM-95) Arles, France, 1995, Editions Frontières, Gif-sur-Yvette, 1996, p. 451.

[CAP01] F. Cappuzzello et al., Phys. Lett. B 516, 21 (2001)

[CAS00] R. F. Casten, B. M. Sherill: Prog. Part. Nucl. Phys. 45, S171 (2000)

[CLA03] J. Clark et al., Nucl. Instr. Meth. B 204, 487 (2003)

[COS09] L. Cosentino et. al, LNS Activity Report 160 (2009)

[CUN07] A.Cunsolo et al ; Eur. Phys. J. Special Topics 150, 343–346 (2007)

[DAR90] D. Darquennes t al., Phys. Rev. C 42, R804 (1190)

[DAV89] C.N. Davids, and J.D. Larson, Nucl. Instr. and Meth. B 40/B41, 1224 (1989)

[DEA03] D.J. Dean, M. Hjorth-Jensen, Red. Mod. Phys. 75, 607 (2003)

[DEF07] E. De Filippo et. al. Phys. LNS Activity Report, 113 (2007)

[DEF08] E. De Filippo et. al., Phys. Rev. Lett., 100, 233202 (2008)

[DEN97] P. Dendooven, Nucl. Instr. Meth. B 126, 182 (1997)

[DIP10] A. Di Pietro et. al., Phys. Rev. Lett. 105 (2010)

[DOB94] J. Dobaczewski et al., Phys. Rev. Lett. 72, 981 (1994)

[DUP06] P. Van Duppen, *Isotope Separation On Line and Post Acceleration*, Lect. Notes Phys. 700, 37–77 (2006)

[DUP92] P. Van Duppen et al., Nucl. Instr. Meth. B 70, 393 (1992)

[DUP97] P. Van Duppen, Nucl. Instr. Meth. B 126, 66 (1997)

[ELE04] Z. Elekes et al., Phys. Lett. B 586, 34 (2004)

[ENQ02] T. Enqvist et al., Nucl. Phys. A 703, 435 (2002)

[EURW] http://www.eurisol.org

[FAIW] http://www.gsi.de/fair/FAIR-Preparatory-Phase/summary_e.html

[FIG91] P.Figuera et al., Il nuovo Cimento A 104, 251 (1991)

[FRIBW] http://groups.nscl.msu.edu/frib/rates/fribrates.htm

[GAE03] M. Gaelens et al., Nucl. Instr. Meth. B 204, 48 (2003) and www.cyc.ucl.ac.be

[GEI03] H. Geissel et al., Nucl. Instr. and Meth. B 204, 71 (2003), and references therein.

[GLA59] R.J. Glauber, in Lectures in theoretical physics, ed. W.E. Brittin (interscience, N.Y., 1959) Vol. 1

[GOS77] J. Gosset et al., Phys. Rev. C 16, 629 (1977).

[GOU83] F.S . Goulding, D.A. Landis and N.W. Madden, IEEE Trans. Nucl. Sci. NS-30, 301 (1983)

[GRA04] H. Grawe, Shell Model from a Practitioner's Point of View, Lect. Notes Phys. 651, 33–75 (2004)

[GRA08] L. Grassi et al., LNS Activity Report, 106 (2008)

[GUR03] A.F. Gurbich, *Differential Cross Sections for Elastic Scattering of Protons and Helions from Light Nuclei*, Lectures given at the Workshop on Nuclear Data for Science and Technology: Materials Analysis, (2003)

[HAB00] D. Habs et al.: Hyp. Int. 129, 44 (2000)

[HER01] F. Herfurth et al., Nucl. Instr. Meth. A 469, 254 (2001)

[HEY04] K. Heyde, *Basic ideas and concepts in nuclear physics, third Edition*, Institute of Physics Publishing Bristol and Philadelphia

[HIEW] http://hie-isolde.web.cern.ch/hie-isolde/

[HUB91] L. Hubbeling et al. Nucl. Instr. and Meth. A310, 197 (1991)

[HUR88] G.S. Hurst and M.G. Payne, Principles and Applications of Resonance Ionization

[HUY06] M. Huyse, The Why and How of Radioactive-Beam Research, Lect. Notes Phys. 651, 1–32 (2006)

[IWA97] N. Iwasa, H. Geissel, G. Münzenberg, C. Scheidenberger, Th. Schwab, H. Wollnik, Nucl. Instr. and Meth. B 126, 284 (1997)

[IWA00a] H. Iwasaki et al., Phys. Lett. B491, 8 (2000)

[IWA00b] H. Iwasaki et al., Phys. Lett. B481, 7 (2000)

[JEU77] J.P. Jeukenne, A. Lejeune, C. Mahaux, Phys. Rev. C16, 80 (1977), and references therein.

[JON04] B. Jonson Physics Reports 389, 1-59 (2004)

[KEE09] Progress in Particle and Nuclear Physics 63, 396 (2009)

[KHA96] Al-Khalili et. al., Phys. Rev. Lett., 76, 3903 (1996)

[KHA97] J.S. Al-Khalili, J.A. Tostevin, J.M. Brooke, Phys. Rev. C 55, R1018 (1997)

[KHA01] J.S. Al-Khalili, J.A. Tostevin, Scattering ed P. Sabatier, E.R. Pike (London Academic) chapter 3.1.3 (2001).

[KHA04] Jim Al-Khalili, *An Introduction to Halo Nuclei*, Lect. Notes Phys. 651, 77–112 (2004)

[KIR92] R. Kirchner et al.: Nucl. Instr. Meth. B 70, 56 (1992)

[KNO00] Glenn F. Knoll, *Radiation Detection and Measurement*, third edition, 2000 Wiley

[KOB88] T. Kobayashi et al., Phys. Rev. Lett. 60, 2599 (1988)

[KUB03] T. Kubo et al., Nucl. Instr. and Meth. B 204, 97 (2003), and references therein.

[LAP08] V. Lapoux et al., Physics Letters B 658, 198 (2008)

[LEO94] William R. Leo, *Techniques for Nuclear and Particle Physics Experiments*, Springer-Verlag (1994)

[LET87] V.S. Letokhov, *Laser Photo Ionization Spectroscopy*, (Academic Press, Orlando) 1987

[LIS10] http://fribusers.org/4_GATHERINGS/2_SCHOOLS/2010/lectures.html, K. Lister

[LNSW] web site www.lns.infn.it

[MEN05] M. Menna et al. Proc. of the Particle Accelerator Conference 2005, Knoxville, 898.

[MON05] G.Montagnoli et al., Nucl. Instr. and Meth. A 547, 455 (2005)

[MOO92] R.B. Moore and G. Rouleau: J. Mod. Optics 39, 361 (1992)

[MOR04] D.J. Morrissey, B.M. Sherrill, In-Flight Separation of Projectile Fragments, Lect. Notes Phys. 651, 113–135 (2004)

[MOR78] D.J. Morrissey et al., Phys. Rev. C 18, 1267 (1978)

[MOR79] D.J. Morrissey et al., Phys. Rev. Lett. 43, 1139 (1979)

[MUS06] A. Musumarra et al., LNS Activity Report, 55 (2006)

[MUT00] M. Mutterer et al., IEEE Trans. NS 47, 756 (2000)

[NEY03] G. Neyens: Rep. Prog. Phys. 66, 633 (2003)

[NIE01] A. Nieminen et al.: Nucl. Instr. Meth. A 469, 244 (2001)

[NOL85] J.A. Nolen, and L. Harwood, *Instrumentation for Heavy Ion Nuclear Research*, D. Shapira, ed. (Harwood, New York, 1985) 171

[NOL03] J.A. Nolen et al., Nucl. Instr. and Meth. B 204, 293 (2003), ibid. pp. 298-302

[ORR92] N. Orr et al., Phys. Rev. Lett. 69, 2050 (1992)

[PAC00] J.C. Pacheco, N. Vinh Mau, Nucl. Phys. A 669, 135 (2000)

[PAG01] A. Pagano et al., Nucl. Phys. A 681, 331 (2001)

[PAG04] A. Pagano et al., Nucl. Phys. A 734, 504 (2004)

[PER76] C.M. Perey and F.G. Perey, Atomic data and nuclear data tables 17, 1-101 (1976)

[PFA96] R. Pfaff et al., Phys. Rev. C 53, 1753 (1996)

[PFU02] M. Pfützner et al.: Eur. Phys. J. A10, 279 (2002)

[PIR01] S. Pirrone et al, Phys. Rev. C 64, 024610 (2001)

[POL05] G. Politi et al., 2005 IEEE Nuclear Science Symposium Conference Record, N28-5 (2005)

[PTO78] PTOLEMY, M. Macfarlane and Steven C. Pieper, ANL-76-11 Rev.1 Mathematics and Computers (UC-32) (1978)

[RAP07] E. Rapisarda et al. Eur. Phys. J. Special Topics 150, 269–272 (2007) Mechanisms Varenna, 2003, p. 11

[RHO80] M. Rhoades-Brown et al., Phys. Rev. C 21, 2417 (1980).

[RIF08] D. Rifuggiato et a., LNS Activity Report, 147 (2008)

[SAK87] Y. Sakuragi, Phys. Rev. C35, 2161 (1987)

[SAV96] A. Savalle et al., In Proc. EPAC96 Fifth European Particle Accelerator Conf., (IoP Publishing, 1996) pp. 2403-2405, and A. Joubert et al., GANIL Report A-91-01, (1991) exunpublished

[SCH03] S. Schwarz et al.: Nucl. Instr. Meth. B 204, 507 (2003)

[SCH87] K.-H. Schmidt et al., Nucl. Instr. and Meth. A 260, 287 (1987)

[SOU02] G.A. Souliotis et al., Phys. Lett. B 543, 163 (2002)

[SPESW] http://www.lnl.infn.it/~spes/

[SPIW] http://pro.ganil-spiral2.eu/

[STA85] Fl. Stancu, D.M. Brink, Phys. Rev. C 32, 1937 (1985)

[TAN85] I. Tanihata et al., Phys. Lett. B206, 592 (1985)

[TAN03] I. Tanihata et. al., C. R. Physique 4, 437 (2003)

[TAR08] O.B. Tarasov and D. Bazin, Nucl. Instr. and Meth. B 266, 4657-4666 (2008), and reference therein, http://group.nscl.msu.edu/lise/lise.html

[TAS01] L. Tassan-Got, Nucl. Instr. and Meth. B 194, 503 (2002)

[TRIB89] 27. R.E. Tribble, R.H. Burch, and C.A. Gagliardi, Nucl. Instr. and Meth. A 285, 441 (1989)

[TYM99] N.K. Tymofeyuk and R. C. Johnson, Phys. Rev. C59, 1545 (1999)

[VIL03] A.C.C. Villari et al., Nucl. Instr. and Meth. B 204, 31 (2003)

[WER94] Werner, T. et al., Phys. Lett. B 335, 259 (1994)

[WIE08] M. Wiedeking et al., Phys. Rev. Lett. 100, 152501 (2008)

[WIL97] W.S.C. Williams, *Nuclear and Particle Physics*, Oxford Science pubblication

[WIN01] J.S. Winfield et al, Nuclear Physics A 683. 48 (2001)

[WUO10] A. H. Wuosmaa et al., Phys. Rev. Lett. 105, 132501 (2010)

[ZHE02] T. Zheng et al., Nuclear Physics A 709, 103 (2002)

[ZHU93] M.V. Zhukov et al., Phys. Rep. 231, 151 (1993).

ACKNOWLEDGEMENTS

I would like to thank Prof. Francesca Rizzo and Dr. Sara Pirrone for their scientific support. I would like to express my deep gratitude to Dr. Giuseppe Cardella, his expertise, knowledge and patience has contributed considerably to my training. I would like to thank Dr. Enrico De Filippo for his invaluable help in the analysis programs, his smooth personality has made very pleasant the work in collaboration. Finally, I would like to acknowledge Dr. Angelo Pagano and all the members of the EXOCHIM collaboration.

During these years I make sincerely friendships with different colleagues Italian and foreigner, and I thank them to listen me and for their not only scientific advices.